The spectra of gravitational atoms

Baumann, D.; Chia, H.S.; Stout, J.; Haar, L.T.

[Link to publication](#)

The Spectra of Gravitational Atoms

Daniel Baumann, Horng Sheng Chia, John Stout and Lotte ter Haar

Institute for Theoretical Physics, University of Amsterdam,
Science Park 904, Amsterdam, 1098 XH, The Netherlands

Abstract

We compute the quasi-bound state spectra of ultralight scalar and vector fields around rotating black holes. These spectra are determined by the gravitational fine structure constant α, which is the ratio of the size of the black hole to the Compton wavelength of the field. When α is small, the energy eigenvalues and instability rates can be computed analytically. Since the solutions vary rapidly near the black hole horizon, ordinary perturbative approximations fail and we must use matched asymptotic expansions to determine the spectra. Our analytical treatment relies on the separability of the equations of motion, and is therefore only applicable to the scalar field and the electric modes of the vector field. However, for slowly-rotating black holes, the equations for the magnetic modes can be written in a separable form, which we exploit to derive their energy eigenvalues and conjecture an analytic form for their instability rates. To check our conjecture, and to extend all results to large values of α, we solve for the spectra numerically. We explain how to accurately and efficiently compute these spectra, without relying on separability. This allows us to obtain reliable results for any $\alpha \gtrsim 0.001$ and black holes of arbitrary spin. Our results provide an essential input to the phenomenology of boson clouds around black holes, especially when these are part of binary systems.

Contents

1 Introduction

Light particles with very weak couplings to ordinary matter are hard to detect by traditional experimental means. For example, neutrinos—the lightest massive particles of the Standard Model and one of the most abundant particles in the universe—have only been detected directly through their rare interactions in enormous water tanks [1, 2]. New (ultra)light particles with couplings much weaker than those of neutrinos can therefore easily have escaped all of our current detection efforts. However, if these hypothetical particles are much lighter than neutrinos, and if they are bosons, then they can be produced around rotating black holes through a process called superradiance [3, 4]. This effect can extract enough mass and angular momentum from the black hole to form a large condensate of the bosonic field. The gravitational influence of these superradiantly-generated 'boson clouds' is potentially observable, making this an interesting laboratory of physics beyond the Standard Model [5, 6].

The black hole carrying the boson cloud is sometimes called a *gravitational atom* since the system closely resembles the proton-electron structure in a hydrogen atom (see Fig. 1). While superradiance with scalar fields has been studied extensively in the past [6–18], the exploration of vector fields is much more recent [19–28]. In this paper, we study the spectra of these gravitational atoms for both scalar and vector clouds. Our principal goal is to accurately compute the energy splittings between the eigenstates of the cloud—the analog of the fine and hyperfine structure of the hydrogen atom—for both types of fields. The differences in the spectra are potentially observable in future gravitational wave experiments. In particular, if the gravitational atom is part of a binary system [13] (see also [29–33]), the gravitational perturbation due to the companion can induce transitions among the different states of the cloud. These transitions can then affect the dynamics of the inspiral, leaving an imprint on observed gravitational waveforms. Detailed knowledge of the spectra will be required to interpret such experimental results and infer the microscopic nature of the cloud.

Both the efficiency of black hole superradiance and the spectrum of the cloud depend on the ratio of the gravitational radius of the black hole, $r_g \equiv GM/c^2$, to the (reduced) Compton wavelength of the field, $\lambda_c \equiv \hbar/(\mu c)$, where μ is the mass of the field. This defines the gravitational fine structure constant

$$\alpha \equiv \frac{r_g}{\lambda_c} = \frac{GM\mu}{\hbar c}, \qquad (1.1)$$

which becomes $\alpha = M\mu$ in natural units. A bosonic condensate only forms around the black hole if α is smaller than of order unity. In the limit $\alpha \ll 1$, the superradiance phenomenon can be treated perturbatively as an expansion in powers of α. Using such an expansion, the energy spectrum [13] and instability rates [7] were computed for a massive scalar field, up to the order in α at which the degeneracies between all modes in the spectrum are broken. The computation for a massive vector field, on the other hand, is much more involved [20–23], and has not yet been treated with complete rigor. Until recently, the main technical obstruction in the vector analysis has been the fact that the Proca equation could not be decomposed into separate angular and radial equations. However, in [34, 35], a separable ansatz was discovered
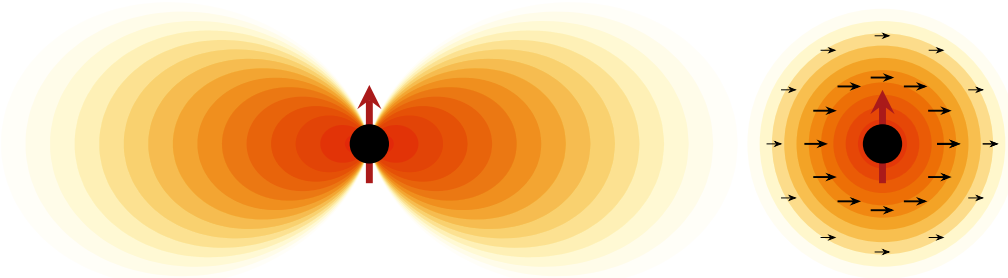
Figure 1: Illustration of the dominant growing modes of the scalar $(2p)$ and vector $(1s)$ gravitational atoms. The small arrows denote the intrinsic spin of the vector field, which allows for superradiant growth even for states without orbital angular momentum.

for the electric modes of a massive vector field on the Kerr background.[1] In this paper, we use this ansatz to compute the spectrum and instability rates for a Proca field perturbatively. A special feature of superradiantly-generated vector clouds is that the dominant growing mode is a $1s$ state, which has vanishing orbital angular momentum. In this case, the spin of the black hole is converted into the intrinsic spin of the field, and the cloud has non-negligible support near the black hole, see Fig. 1. These modes are then especially sensitive to the near-horizon geometry of the black hole, and this sensitivity necessitates going beyond ordinary perturbation theory to determine the spectrum.

While the magnetic modes of the Proca field are separable on the Schwarzschild background [36], a separable ansatz in the Kerr spacetime remains elusive, and thus rigorous analytic results are difficult to achieve for this part of the spectrum. Fortunately, all degeneracies between the states in the spectrum are broken at linear order in the spin of the black hole, and the Schwarzschild ansatz still separates the Proca equation at this order [20, 21]. Assuming that the fine and hyperfine structure of the magnetic modes are similar to their electric counterparts, we can use this small-spin expansion to derive the magnetic spectrum perturbatively in α. Furthermore, we 'derive' their leading-order instability rates using educated guesswork, and are thus able to attain perturbative results for the most phenomenologically relevant aspects of the spectrum, for all modes of the Proca field.

To test our analytic results, and to move beyond the limit of small α, we compute the spectra of scalar and vector clouds numerically (see also e.g. [8, 21, 27, 28]). Formulating this as a nonlinear eigenvalue problem allows us to attain highly accurate results for the spectrum with little computational cost. Our method also has the advantage that it does not rely upon a separable ansatz, which allows us to rigorously determine the magnetic spectrum and check our analytic guesswork for its instability rates. Our method is reliable even for very small values of α, where precise numeric results are typically difficult to achieve without separability [21, 27], and we apply it to both the dominant growing modes and other phenomenologically relevant states. We pay special attention to the numerical obstacles that can potentially destroy the accuracy

---

[1]In [28], it was shown that a special class of magnetic modes are contained within this ansatz (see Appendix B). However, it is not yet clear whether it contains every magnetic mode, nor is it clear how to recover them.

of a solution, and describe how to avoid them. This new formulation thus provides a robust and flexible method for finding the quasi-bound state spectra for arbitrary ultralight tensor fields about any stationary black hole, without relying on separability of the equations of motion.

Outline   The plan of the paper is as follows: in Section 2, we set up the basic equations describing massive scalar and vector fields around rotating black holes. We outline the computations performed in the rest of the paper and present a summary of key results. In Section 3, we compute the spectrum of energy eigenvalues and the associated instability rates, for both the scalar field and the electric modes of the vector field, using matched asymptotic expansions. We also compute the energy spectra of the magnetic modes at linear order in the black hole spin $\tilde{a}$ and motivate their conjectured instability rates. In Section 4, we describe our numerical methods. Our techniques, in principle, work for ultralight fields of arbitrary spin and do not assume separability of the equations of motion. In Section 5, we summarize our results and present an outlook on future applications. The appendices contain additional technical details: In Appendix A, we review essential facts on tensor spherical harmonics. In Appendix B, we present material supporting the analytical treatment in Section 3, while Appendix C spells out many of the details left out in the description of the numerics in Section 4. Finally, Appendix D collects the most important variables used in this paper.

Notation and conventions   We will use a metric with 'mostly plus' signature $(-,+,+,+)$ and, unless stated otherwise, work in natural units with $G = \hbar = c = 1$. Except when presenting explicit results, we will set $\mu \equiv 1$, so that times and distances are measured relative to the typical oscillation timescale and Compton wavelength of the fields. Greek letters will denote spacetime indices $(\mu, \nu, \ldots)$, while Latin letters will either stand for spatial indices $(i, j, \ldots)$, label indices $(i, k, \ldots)$, or for vierbein indices $(a, b, \ldots)$. To avoid confusion, we will sometimes wrap label indices in parentheses. We will adopt Boyer-Lindquist coordinates for the Kerr black hole with mass M and specific angular momentum a. The line element is then

$$\mathrm{d}s^2 = -\frac{\Delta}{\Sigma}\left(\mathrm{d}t - a\sin^2\theta\,\mathrm{d}\phi\right)^2 + \frac{\Sigma}{\Delta}\mathrm{d}r^2 + \Sigma\mathrm{d}\theta^2 + \frac{\sin^2\theta}{\Sigma}\left(a\,\mathrm{d}t - (r^2 + a^2)\,\mathrm{d}\phi\right)^2 , \qquad (1.2)$$

where $\Delta \equiv r^2 - 2Mr + a^2$ and $\Sigma \equiv r^2 + a^2\cos^2\theta$. The roots of Δ determine the inner and outer horizons, located at $r_\pm = M \pm \sqrt{M^2 - a^2}$, and the angular velocity of the black hole at the outer horizon is $\Omega_H \equiv a/2Mr_+$. Dimensionless quantities, defined with respect to the black hole mass M, are denoted by tildes; e.g. $\tilde{a} \equiv a/M$ and $\tilde{r}_\pm \equiv r_\pm/M$.

The scalar and vector eigenstates are denoted by $|n\ell m\rangle$ and $|n\ell jm\rangle$, with the integers $\{n, \ell, j, m\}$ labeling the principal, orbital angular momentum, total angular momentum, and azimuthal angular momentum numbers, respectively. Following the convention in atomic physics, we have $n \geq \ell + 1$. We refer to vector modes that acquire a factor of $(-1)^j$ under a parity transformation as 'electric modes,' and those that acquire a factor of $(-1)^{j+1}$ as 'magnetic modes.' These modes are to be distinguished from odd and even modes, which, by our convention, receive a factor of -1 and $+1$ under parity, respectively.

2 Scalars and Vectors around Kerr

Massive scalar and vector fields in a general spacetime with metric $g_{\alpha\beta}$ satisfy similar equations of motion,

$$\left(g^{\alpha\beta}\nabla_\alpha\nabla_\beta - \mu^2\right)\Phi \ = 0\,, \tag{2.1}$$

$$\left(g^{\alpha\beta}\nabla_\alpha\nabla_\beta - \mu^2\right)A_\mu = 0\,. \tag{2.2}$$

These are called the Klein-Gordon and Proca equations, respectively, and the latter must be supplemented by the Lorenz constraint $\nabla^\mu A_\mu = 0$. The goal of this paper is to determine the quasi-bound state solutions of these equations in the Kerr background. This section serves as an overview for the rest of the paper and we present a summary of both our analytic and numeric results in §2.4, relegating their detailed derivations to Sections 3 and 4.

2.1 Tensor Representations

We begin with a discussion of general tensor fields $T_{\mu\nu\ldots\rho}$ on the Kerr background. We are interested in quasi-bound states solutions, which are 'purely ingoing' at the outer horizon and vanish at infinity. As in atomic physics, these solutions will be characterized by a set of discrete 'quantum numbers' describing the energy, the orbital angular momentum and the intrinsic spin of the states. A precise definition of these quantum numbers is complicated by the fact that the spin of black hole breaks spherical symmetry. We will label our states by the quantum numbers they attain in the flat-space limit, where the spin of the black holes can be ignored.

In order to define the flat-space limit, it is convenient to rescale the temporal and radial coordinates, $t \mapsto t\mu^{-1}$ and $r \mapsto r\mu^{-1}$, so that the metric (1.2) becomes

$$\mu^2 \mathrm{d}s^2 = -\frac{\Delta}{\Sigma}\left(\mathrm{d}t - \alpha\tilde{a}\sin^2\theta\,\mathrm{d}\phi\right)^2 + \frac{\Sigma}{\Delta}\mathrm{d}r^2 + \Sigma\mathrm{d}\theta^2 + \frac{\sin^2\theta}{\Sigma}\left(\alpha\tilde{a}\,\mathrm{d}t - (r^2 + \alpha^2\tilde{a}^2)\,\mathrm{d}\phi\right)^2\,, \tag{2.3}$$

where $\tilde{a} \equiv a/M$ and

$$\begin{aligned}
\Delta &\equiv r^2 - 2\alpha r + \alpha^2\tilde{a}^2\,, \\
\Sigma &\equiv r^2 + \alpha^2\tilde{a}^2\cos^2\theta\,.
\end{aligned} \tag{2.4}$$

All physical quantities are now measured in units of the Compton wavelength of the field, μ^{-1}, which we henceforth set to $\mu^{-1} \equiv 1$. Notice that the spin parameter $\tilde{a}$ in (2.3) always appears in the combination $\alpha\tilde{a}$, so spherical symmetry is approximately restored when $\alpha \ll 1$. In fact, in the limit $\alpha \to 0$, the line element (2.3) reduces to that of Minkowski spacetime, while at linear order in α it becomes the Schwarzschild solution. Spin-dependent terms, such as those corresponding to the Lense-Thirring effect, only appear at quadratic order in α. As far as the dynamics of the field is concerned, we therefore expect the effects of spin to be subleading compared to the gravitational potential sourced by M.

The eigenstates of the field are labeled by a discrete set of quantum numbers that reflect the (approximate) isometries of the background metric. To identify these quantum numbers, we first

4

note that the Kerr geometry has two Killing vectors

$$k_t \equiv -i\frac{\partial}{\partial t}\,, \qquad k_z \equiv -i\frac{\partial}{\partial \phi}\,, \tag{2.5}$$

representing the fact that the metric (2.3) is both stationary and axisymmetric. The equations of motion for an arbitrary tensor field $T_{\mu\nu\cdots\rho}$ on the Kerr background will inherit the isometries (2.5). If these equations are linear, we may decompose their solutions in terms of states with definite frequency and azimuthal angular momentum,[2]

$$\begin{aligned}
\pounds_t\, T_{\mu\nu\cdots\rho} &= -\omega\, T_{\mu\nu\cdots\rho}\,, \\
\pounds_z\, T_{\mu\nu\cdots\rho} &= +m\, T_{\mu\nu\cdots\rho}\,,
\end{aligned} \tag{2.6}$$

where $\pounds_t \equiv \pounds_{k_t}$ and $\pounds_z \equiv \pounds_{k_z}$ are the Lie derivatives with respect to the isometries (2.5). In the Schwarzschild limit $\tilde{a} \to 0$, the geometry gains two more Killing vector fields k_x and k_y which, together with k_z, form an SO(3) algebra. We can then expand the field into its temporal and spatial components, which we further expand in representations of this algebra, i.e. eigentensors of the *total angular momentum* operator

$$\pounds^2\, T_{ik\cdots l} \equiv \left(\pounds_x^2 + \pounds_y^2 + \pounds_z^2\right) T_{ik\cdots l} = j(j+1)\, T_{ik\cdots l}\,, \tag{2.7}$$

where j denotes the total angular momentum. Furthermore, in the flat-space limit, $\alpha \to 0$, solutions also have definite orbital angular momentum ℓ (cf. Appendix A), so that they can be characterized by the quantum numbers ω, ℓ, j and m. We will label such states by $|n\ell jm\rangle$, where we have introduced an integer quantum number n that indexes the discrete quasi-bound state frequencies ω_n. Since total and orbital angular momenta are the same for the scalar field, we will label its states by $|n\ell m\rangle$. States still have definite total angular momentum in the Schwarzschild limit, but indefinite orbital angular momentum. At finite $\tilde{a}$, these states no longer have definite total angular momentum. Nevertheless, we will still label our states by $|n\ell jm\rangle$ with the understanding that these quantum numbers regain their physical meaning as $\alpha \to 0$.

Finally, the Kerr metric is invariant under the parity transformation

$$\mathcal{P}: \ (\theta, \phi) \mapsto (\pi - \theta, \phi + \pi)\,. \tag{2.8}$$

This helps us to further organize the spectrum into states with definite parity. Solutions to the Klein-Gordon and Proca equations with definite parity are invariant under (2.8) up to a sign, and, with our conventions, we have $\mathcal{P}|n\ell m\rangle = (-1)^\ell|n\ell m\rangle$ and $\mathcal{P}|n\ell jm\rangle = (-1)^{\ell+1}|n\ell jm\rangle$ for scalars and vectors, respectively. See Appendix A for a more detailed discussion.

---

[2]Our analysis will focus entirely on complex scalar and vector fields, as the complex representations of these isometries are much simpler than for real fields. Because the equations of motion are linear, a real solution can be generated by simply taking the real part of a complex solution, and so the spectra are identical.

2.2 Massive Scalar Fields

We now specialize to the case of a massive scalar field around a Kerr black hole. Since the Klein-Gordon equation is relatively simple, this will serve as a useful illustration of our approach without the technical distractions that arise in the vector analysis.

An important feature of the Klein-Gordon equation (2.1) is that it is separable in Boyer-Lindquist coordinates through the ansatz [37, 38]

$$\Phi(t, \mathbf{r}) = e^{-i\omega t + im\phi} R(r) S(\theta). \tag{2.9}$$

The spheroidal harmonics $S(\theta)$ obey the differential equation[3]

$$\left(-\frac{1}{\sin\theta}\frac{d}{d\theta}\left(\sin\theta\frac{d}{d\theta}\right) - c^2\cos^2\theta + \frac{m^2}{\sin^2\theta}\right)S = \Lambda S, \tag{2.10}$$

where Λ is the angular eigenvalue and the spheroidicity parameter is

$$c^2 \equiv -\alpha^2 \tilde{a}^2 (1 - \omega^2). \tag{2.11}$$

The radial equation is a confluent Heun equation,[4]

$$0 = \frac{1}{R\Delta}\frac{d}{dr}\left(\Delta\frac{dR}{dr}\right) - \frac{\Lambda}{\Delta} - (1 - \omega^2) + \frac{P_+^2}{(r - r_+)^2} + \frac{P_-^2}{(r - r_-)^2}$$
$$- \frac{A_+}{(r_+ - r_-)(r - r_+)} + \frac{A_-}{(r_+ - r_-)(r - r_-)}, \tag{2.12}$$

where we have defined the following coefficients

$$A_\pm \equiv P_+^2 + P_-^2 + \gamma^2 + \gamma_\pm^2 \quad \text{and} \quad P_\pm \equiv \frac{\alpha(\tilde{a}m - 2r_\pm\omega)}{r_+ - r_-}, \tag{2.13}$$

with

$$\gamma^2 \equiv \frac{1}{4}(r_+ - r_-)^2(1 - \omega^2),$$
$$\gamma_\pm^2 \equiv \left[\alpha^2(1 - 7\omega^2) \pm \alpha(r_+ - r_-)(1 - 2\omega^2)\right]. \tag{2.14}$$

We are interested in quasi-bound states, i.e. solutions to (2.12) that are purely ingoing at the horizon and vanish at infinity:

$$R(r) \propto \begin{cases} (r - r_+)^{iP_+} & \text{as } r \to r_+ \\ \exp(-\sqrt{1 - \omega^2}\, r) & \text{as } r \to \infty \end{cases}. \tag{2.15}$$

As is typical for eigenvalue problems, these two boundary conditions can only be simultaneously

---

[3]To avoid clutter, we suppress the dependence on the angular quantum numbers, i.e. $S \equiv S_{\ell m}$ and $\Lambda \equiv \Lambda_{\ell m}$.

[4]The Heun equation is a generalization of the hypergeometric equation with four, instead of three, regular singular points. By merging two of these singularities, we arrive at the confluent Heun equation, which is similarly a generalization of the confluent hypergeometric equation (2.17) that determines the wavefunctions of the hydrogen atom. The angular equation (2.10) is also a confluent Heun equation. For a detailed treatment, see [39].
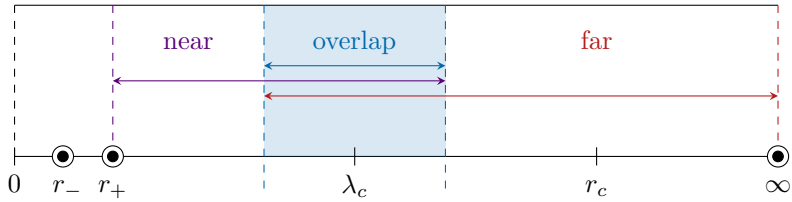
Figure 2: Illustration of the near and far regions used in our perturbative treatment for the massive scalar field, where $r_{\pm}$ are the inner and outer horizons of the black hole, $\lambda_c = \mu^{-1}$ is the Compton wavelength of the field, and $r_c = (\mu\alpha)^{-1}$ is the typical Bohr radius of the quasi-bound state. The two asymptotic solutions are matched in the overlap region.

satisfied for specific values of ω. Unfortunately, while solutions to both (2.10) and (2.12) are well known, closed-form expressions for their eigenvalues are not. However, in the limit $\alpha \ll 1$, we can construct a perturbative expansion of the spectrum. This perturbative approach is complicated by the presence of terms in (2.12) that diverge as $r \to r_+$. These terms represent *singular perturbations* in α, i.e. if we naively expand them in powers of α, an infinite number of terms become relevant as $r \to r_+$. Luckily, this is not a disaster. The role of these singular terms is simply to modify the characteristic scale on which $R(r)$ varies. As we will see explicitly in §3.1, the radial function satisfies

$$\frac{1}{R}\frac{dR}{dr} \sim \begin{cases} \alpha^{-1} & \text{as } r \to r_+ \\ \alpha & \text{as } r \to \infty \end{cases} . \tag{2.16}$$

This motivates splitting the interval $[r_+, \infty)$ into a 'near region' and a 'far region' (see Fig. 2). In the near region, the $(r - r_+)^{-2}$ pole in (2.12) dominates and an approximate solution to the differential equation for $R(r)$ can be obtained by dropping the subleading terms. In the far region, on the other hand, the non-derivative terms are dominated by the constant $(1 - \omega^2)$ term. By dropping the sub-leading contributions to (2.12) in each region, we can then construct approximate analytic solutions in the near and far regions, order-by-order in α. These solutions are then matched in the 'overlap region,' allowing a determination of the frequency eigenvalue ω, as an expansion in powers of α. The details of this *matched asymptotic expansion* will be presented in Section 3. For the angular problem, the perturbative solutions are valid over the entire angular domain and no matching is necessary.

To gain an intuitive understanding of the behavior of the solutions at leading order, it is instructive to first consider the equation of motion obeyed by the far-zone radial function, R_0^{far}. At leading order, this reads

$$\left[-\frac{1}{2r^2}\frac{d}{dr}\left(r^2\frac{d}{dr}\right) - \frac{\alpha}{r} + \frac{\ell(\ell+1)}{2r^2} + \frac{1 - \omega^2}{2} \right] R_0^{\text{far}} = 0 \,. \tag{2.17}$$

This is analogous to the time-independent Schrödinger equation for the hydrogen atom, where the radial-gradient term arises from the kinetic energy, the $1/r$ term corresponds to a Coulomb-like central potential with gravitational coupling constant α, the $1/r^2$ term is its centrifugal barrier with orbital angular momentum number ℓ, and the constant term captures the exponential
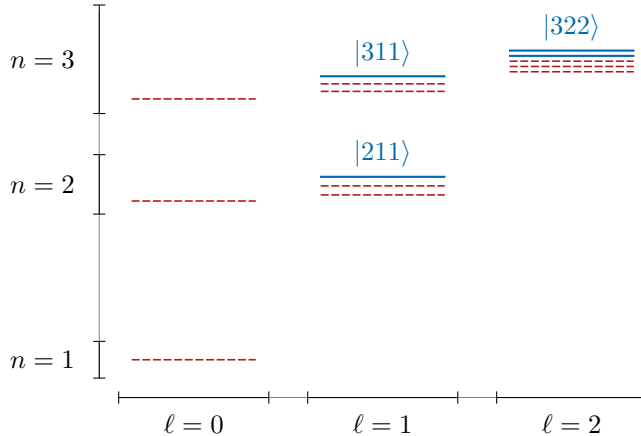
Figure 3: Schematic illustration of the energy spectrum for a massive scalar field. Each state is labeled by the quantum numbers $|n\ell m\rangle$. The solid blue lines are growing modes, while the dashed red lines are decaying modes.

behavior of the quasi-bound states at $r \to \infty$. We therefore expect the energy spectrum of all modes to be Bohr-like at leading order, with the radial function

$$R_0^{\text{far}}(r) \propto e^{-\sqrt{1-\omega^2}\,r}\,r^\ell L_{n-\ell-1}^{(2\ell+1)}\left(2\sqrt{1-\omega^2}\,r\right),\tag{2.18}$$

where $L_k^{(\rho)}$ is the associated Laguerre polynomial, and n is the principal quantum number, which satisfies $n \geq \ell + 1$. The exponential behavior in (2.18) implies that the solution has a typical Bohr radius

$$r_c \equiv (\mu\alpha)^{-1}\,.\tag{2.19}$$

Since (2.17) only captures the physics in the far region, it does not describe physical effects that depend on the boundary condition at the event horizon, such as the instability rates of the energy eigenstates. To study these effects, we match the near- and far-zone solutions. By pushing this procedure to higher orders in α, we determine the complete spectrum of the scalar field. A schematic illustration of this spectrum appears in Fig. 3.

2.3 Massive Vector Fields

The task of solving for the quasi-bound state solutions of vector fields is more involved because the matching involves three different regions, and the equation of motion is not obviously separable. The latter problem was addressed in [35] and [21] where separable ansätze were found for the electric modes and magnetic modes (in the limit of small black hole spin), respectively. In this paper, we use these results to derive the spectrum of vector quasi-bound states perturbatively.

Consider the following ansatz for a vector field on the Kerr background [34, 35]

$$A^\mu = B^{\mu\nu}\nabla_\nu Z\,, \quad \text{with} \quad Z(t,\mathbf{r}) = e^{-i\omega t + im\phi}R(r)S(\theta)\,,\tag{2.20}$$

8
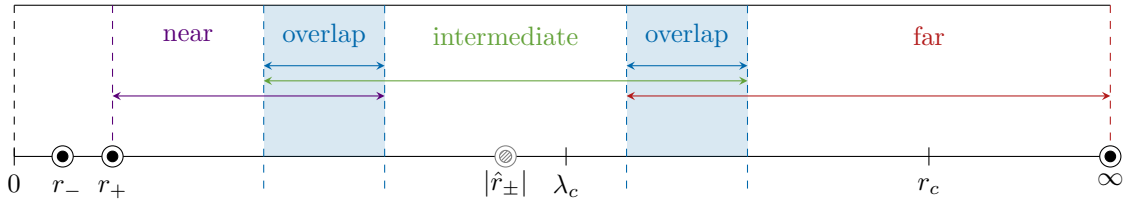
Figure 4: Illustration of the different regions used in our perturbative treatment for the massive vector field. The additional poles at $\hat{r}_{\pm}$ along the imaginary axis reduce the radii of convergence of the near- and far-zone solutions, so that there is no region where they overlap. Matching therefore requires the intermediate region.

where R and S are the radial and angular functions.[5] The polarization tensor $B^{\mu\nu}$ is defined by

$$B^{\mu\nu}\left(g_{\nu\sigma} + i\lambda^{-1}h_{\nu\sigma}\right) = \delta^{\mu}_{\sigma}, \tag{2.21}$$

where λ is generally a complex parameter, which we will refer to as the angular eigenvalue, and $h_{\mu\nu}$ is the principal tensor of the Kerr spacetime [40].[6] An explicit expression for $B^{\mu\nu}$ is given in Appendix B. The three independent degrees of freedom of the vector field can be organized in terms of $j = \ell \pm 1, \ell$. Since the $j = \ell \pm 1$ modes acquire a factor of $(-1)^j$ under a parity transformation, they are called *electric modes*, while the $j = \ell$ modes are the *magnetic modes* [41]. In §3.2, we will show that the ansatz (2.20) captures all of the electric modes of the vector field.[7]

Substituting (2.20) into the Proca equation, we obtain differential equations for $S(\theta)$ and $R(r)$. The angular equation reads [28]

$$\frac{1}{\sin\theta}\frac{\mathrm{d}}{\mathrm{d}\theta}\left(\sin\theta\frac{\mathrm{d}S}{\mathrm{d}\theta}\right) + \left(c^2\cos^2\theta - \frac{m^2}{\sin^2\theta} + \Lambda\right)S = \frac{2\alpha^2\tilde{a}^2\cos\theta}{\lambda^2 q_\theta}\left(\sin\theta\frac{\mathrm{d}}{\mathrm{d}\theta} + \lambda\sigma\cos\theta\right)S, \tag{2.22}$$

where the spheroidicity parameter c^2 was defined in (2.11), and

$$q_\theta \equiv 1 - \alpha^2\tilde{a}^2\lambda^{-2}\cos^2\theta,$$
$$\sigma \equiv \omega + \alpha\tilde{a}\lambda^{-2}(m - \alpha\tilde{a}\omega), \tag{2.23}$$
$$\Lambda \equiv \lambda(\lambda - \sigma) + 2\alpha\tilde{a}m\omega - \alpha^2\tilde{a}^2\omega^2.$$

---

[5]We emphasize that R and S are not the actual radial and angular profiles of the vector field, since the tensor $B^{\mu\nu}$ depends on both r and θ. However, we still retain the terminology 'radial' and 'angular function,' and denote them by R and S, to draw a direct parallel with the scalar. The precise relationships between R, S and the profile of the vector field A_μ in the far zone will be given in §3.2.1.

[6]To simplify many of the following equations, we take the angular eigenvalue λ to be the inverse of that in [34, 35].

[7]In [28], it was found that the ansatz (2.20) restores at least a subset of the magnetic modes in a special limit (see Appendix B for further details). It remains unclear, however, how to write all magnetic modes in separable form. In this paper, we will instead utilize a different ansatz, which, in the limit of small black hole spin, provides a separable equation for all of the magnetic modes.

9

The radial equation becomes

$$
0 = \frac{\mathrm{d}^2 R}{\mathrm{d}r^2} + \left(\frac{1}{r - r_+} + \frac{1}{r - r_-} - \frac{1}{r - \hat{r}_+} - \frac{1}{r - \hat{r}_-} \right) \frac{\mathrm{d}R}{\mathrm{d}r}
$$
$$
+ \left(-\frac{\Lambda}{\Delta} - (1 - \omega^2) + \frac{P_+^2}{(r - r_+)^2} + \frac{P_-^2}{(r - r_-)^2} - \frac{A_+}{(r_+ - r_-)(r - r_+)} \right. \tag{2.24}
$$
$$
\left. + \frac{A_-}{(r_+ - r_-)(r - r_-)} - \frac{\lambda \sigma r}{\Delta (r - \hat{r}_+)} - \frac{\lambda \sigma r}{\Delta (r - \hat{r}_-)} \right) R,
$$

where $\hat{r}_\pm \equiv \pm i\lambda$ depend on the angular eigenvalue and the parameters $P_\pm$ and $A_\pm$ were defined in (2.13). The presence of the additional poles at $r = \hat{r}_\pm$, makes this equation considerably more complicated than the corresponding equation (2.12) in the scalar case.

In principle, the task of determining the spectrum of electric modes of the vector quasi-bound states is the same as for the scalar. However, due to the additional poles at $r = \hat{r}_\pm$, the widths of the near and far regions are now much smaller and these regions no longer overlap. To match the asymptotic expansions in the near and far regions, we must introduce an *intermediate region*[8] that overlaps with both (see Fig. 4) and construct a solution that serves as a bridge. The matching is then performed in a two-step procedure, first between the far and intermediate regions, and then between the intermediate and near regions.

In the Schwarzschild limit, solutions have definite total angular momentum and parity. Because the vector spherical harmonic $Y^i_{j,jm}$ has opposite parity to $Y^i_{j\pm1,jm}$ and the scalar harmonic Y_{jm}, it completely decouples from all other angular modes. This magnetic mode,

$$
A^i(t, \mathbf{r}) = r^{-1} R(r) Y^i_{j,jm}(\theta, \phi) e^{-i\omega t}, \tag{2.25}
$$

is thus completely separable in the Schwarzschild limit [36], and [20, 21] showed that this persists to linear order in $\tilde{a}$. We can thus use this ansatz to determine the magnetic spectrum in the limit of small spin.

Substituting (2.25) into the Proca equation and expanding to first order in $\tilde{a}$, the radial function $R(r)$ satisfies [20, 21]

$$
0 = \frac{\mathrm{d}^2 R}{\mathrm{d}r^2} + \left(\frac{1}{r - \check{r}_+} - \frac{1}{r - \check{r}_-} \right) \frac{\mathrm{d}R}{\mathrm{d}r} + \left(-\frac{\check{\Lambda}}{\Delta} - (1 - \omega^2) \right.
$$
$$
\left. + \frac{\check{P}_+^2}{(r - \check{r}_+)^2} + \frac{\check{P}_-^2}{(r - \check{r}_-)^2} - \frac{\check{A}_+}{(\check{r}_+ - \check{r}_-)(r - \check{r}_+)} + \frac{\check{A}_-}{(\check{r}_+ - \check{r}_-)(r - \check{r}_-)} \right) R, \tag{2.26}
$$

where $\check{\Lambda} = j(j + 1)$ and $\check{P}_\pm, \check{A}_\pm, \check{r}_\pm$ represent $P_\pm$, $A_\pm$, $r_\pm$ expanded to linear order in $\tilde{a}$, respectively. Specifically, the position of the inner and outer horizons, $\check{r}_- = 0$ and $\check{r}_+ = 2\alpha$, have shifted in this approximation, and we expect that (2.26) does not accurately describe the near-

---

[8]Physically, the necessity of the intermediate region arises because the dynamics in the near and far regions depend on the angular momentum of the vector field in distinct ways. As we will see in Section 3, while the dynamics in the near region is sensitive to the total angular momenta of the field (including its intrinsic spin), the dynamics in the far region depends only on its orbital angular momentum. The intermediate region thus smoothly interpolates between these two behaviors.
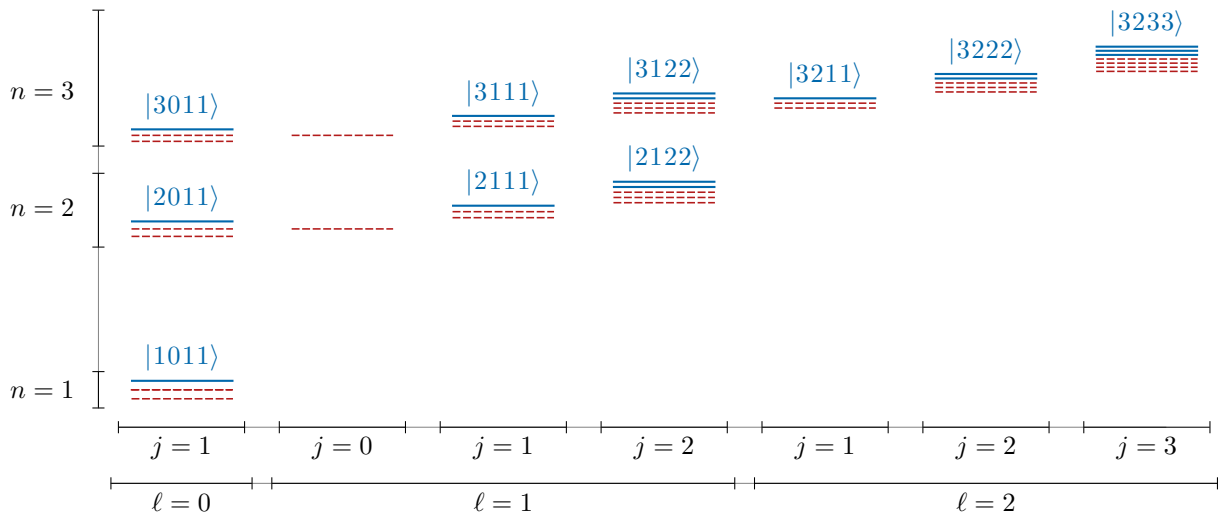
Figure 5: Schematic illustration of the energy spectrum for a massive vector field. Each state is labeled by the quantum numbers $|n\ell jm\rangle$.

horizon behavior of these magnetic modes. When expanded to linear order in $\tilde{a}$, the scalar radial equation (2.12) differs from (2.26) only in its $\mathrm{d}R/\mathrm{d}r$ coefficient. In Section 3, we will discuss the error this small-spin approximation introduces. To compute the magnetic spectra for arbitrary spin, we must still solve the Proca equation (2.2) numerically. For a schematic illustration of the vector field spectrum, see Fig. 5.

2.4   Summary of Results

In Sections 3 and 4, we will derive the spectra of scalar and vector quasi-bound states around Kerr black holes in detail. Here, we summarize our main results.

We write the frequency eigenvalues as

$$\omega \equiv E + i\Gamma \equiv \mu\sqrt{1 - \frac{\alpha^2}{\nu^2}}\,, \tag{2.27}$$

where the real part represents the energy E and the imaginary part determines the instability rates Γ. At leading order, we expect the energy spectrum to be Bohr-like, so that the real part of ν is an integer n. As we will see below, it is also convenient to work with ν because the fine and hyperfine structure can be read off directly from its α-expansion.

For the scalar field, the energy eigenvalues are (see also [13])

$$E_{n\ell m} = \mu\left(1 - \frac{\alpha^2}{2n^2} - \frac{\alpha^4}{8n^4} + \frac{f_{n\ell}}{n^3}\,\alpha^4 + \frac{h_\ell}{n^3}\,\tilde{a}m\alpha^5 + \cdots\right),$$

$$\mathrm{Re}\,(\nu_{n\ell m}) = n + f_{n\ell}\alpha^2 + h_\ell\tilde{a}m\alpha^3 + \cdots, \tag{2.28}$$

11
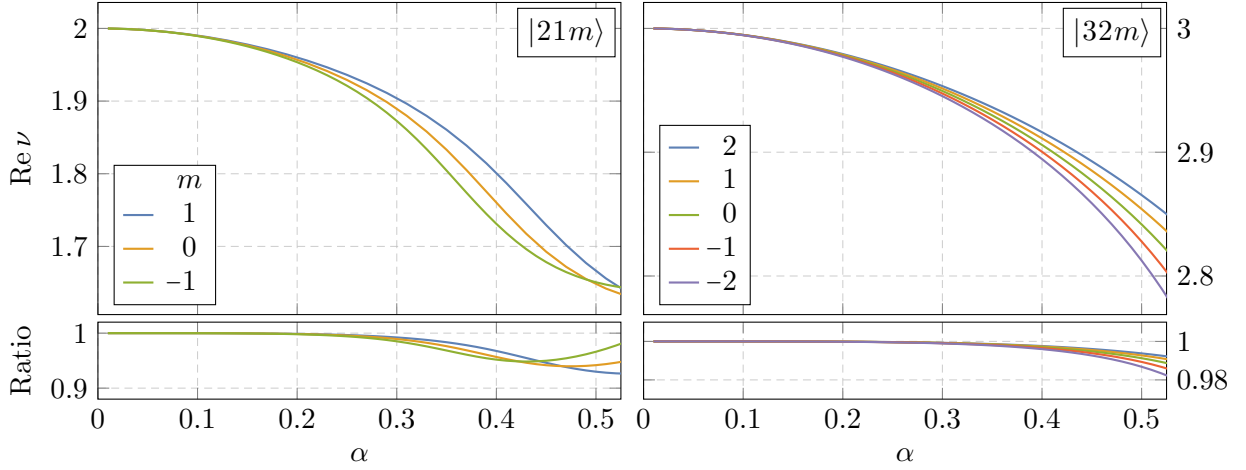
Figure 6: Numeric results of the energy eigenvalues for scalar field eigenstates $|n\ell m\rangle$, for $\tilde{a} = 0.5$. The lower panels show the ratio of the numeric results to the analytical predictions in (2.28). The fine and hyperfine structures are clearly seen in $\operatorname{Re}\nu$, and we find that (2.28) is an excellent approximation for $\alpha \lesssim 0.2$.

where the principal quantum number n are integers that satisfy $n \geq \ell + 1$, and

$$
\begin{aligned}
f_{n\ell} &\equiv -\frac{6}{2\ell + 1} + \frac{2}{n}, \\
h_{\ell} &\equiv \frac{16}{2\ell\,(2\ell + 1)\,(2\ell + 2)}.
\end{aligned}
\tag{2.29}
$$

The first three terms of $E_{n\ell m}$ describe the constant mass term, the hydrogen-like Bohr energy levels and the relativistic corrections to the kinetic energy. The terms proportional to $f_{n\ell}$ and h_{ℓ} are the fine-structure ($\Delta\ell \neq 0$) and hyperfine-structure ($\Delta m \neq 0$) splittings, respectively. As the second line in (2.28) suggests, these splittings can be more easily extracted from the real part of $\nu_{n\ell m}$. Numeric results for $\operatorname{Re}\nu$, and their comparison with the perturbative approximations (2.28), are shown in Fig. 6 for representative scalar modes; cf. Fig. 3 for a schematic illustration of the scalar spectrum.

For the vector field, we study the electric and magnetic modes separately using the ansätze (2.20) and (2.25). However, we find that the energy eigenvalues for *all* vector modes can be written as

$$
\begin{aligned}
E_{n\ell jm} &= \mu\left(1 - \frac{\alpha^2}{2n^2} - \frac{\alpha^4}{8n^4} + \frac{f_{n\ell j}}{n^3}\,\alpha^4 + \frac{h_{\ell j}}{n^3}\,\tilde{a}m\alpha^5 + \cdots\right), \\
\operatorname{Re}\left(\nu_{n\ell jm}\right) &= n + f_{n\ell j}\,\alpha^2 + h_{\ell j}\,\tilde{a}m\alpha^3 + \cdots,
\end{aligned}
\tag{2.30}
$$

with the coefficients

$$
\begin{aligned}
f_{n\ell j} &= -\frac{4\,(6\ell j + 3\ell + 3j + 2)}{(\ell + j)\,(\ell + j + 1)\,(\ell + j + 2)} + \frac{2}{n}, \\
h_{\ell j} &= \frac{16}{(\ell + j)\,(\ell + j + 1)\,(\ell + j + 2)},
\end{aligned}
\tag{2.31}
$$

12
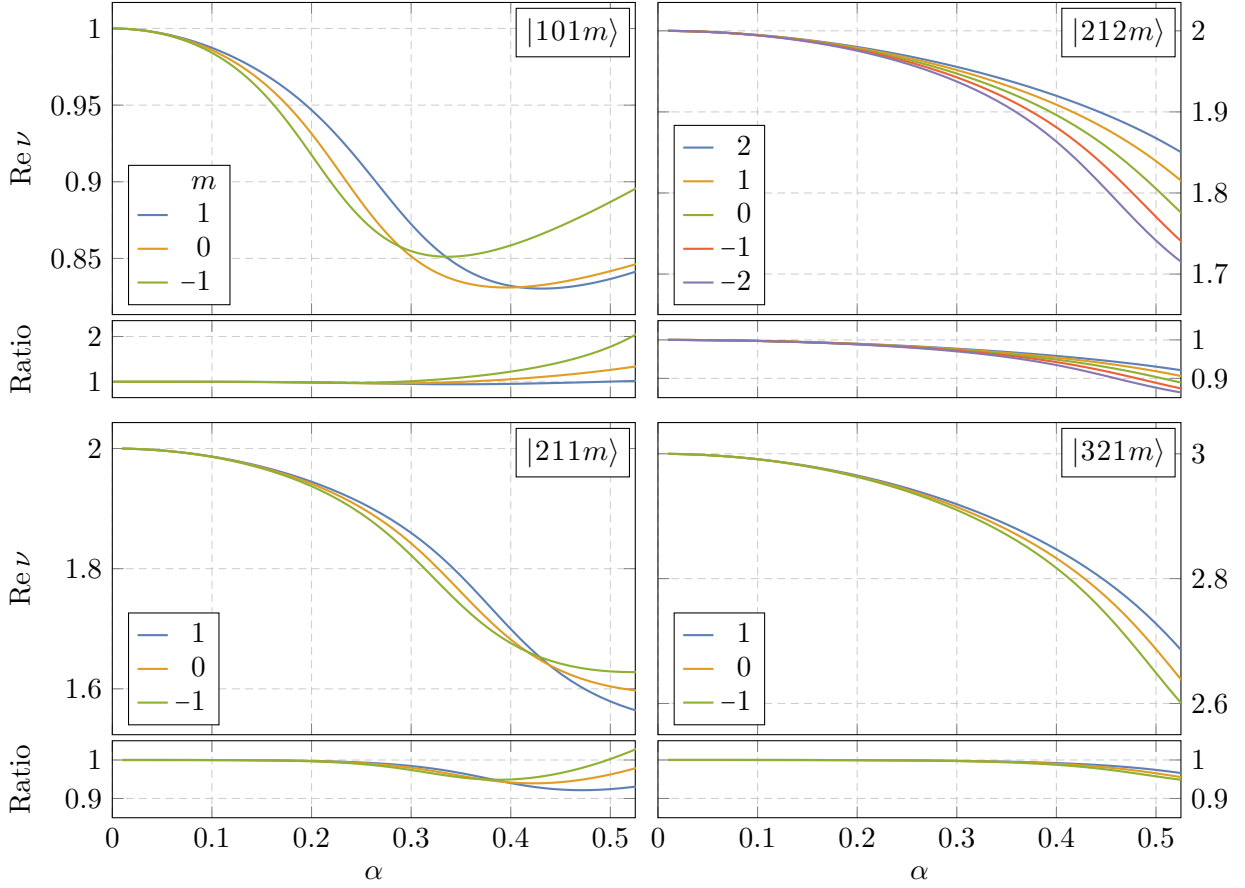
Figure 7: Numeric results of the energy eigenvalues for vector field eigenstates $|n\ell jm\rangle$, for $\tilde{a} = 0.5$. The lower panels show the ratio of the numeric results to our perturbative results in (2.30).

for $j = \ell \pm 1, \ell$. Notably, we find that the spectrum of the vector field is qualitatively similar to the scalar case (2.28); cf. Fig. 5 for a schematic illustration of the vector spectrum. Numeric results for $\mathrm{Re}\,\nu$ for representative electric and magnetic modes, and their comparison with (2.30), are shown in Fig. 7.

We also compute the instability rates for these scalar and vector quasi-bound states. For the scalar field, we find (see also [7])

$$\Gamma_{n\ell m} = 2\tilde{r}_+ C_{n\ell}\, g_{\ell m}(\tilde{a}, \alpha, \omega)\, (m\Omega_H - \omega_{n\ell m})\, \alpha^{4\ell+5}\,, \tag{2.32}$$

where we have defined

$$C_{n\ell} \equiv \frac{2^{4\ell+1}(n+\ell)!}{n^{2\ell+4}(n-\ell-1)!}\left[\frac{\ell!}{(2\ell)!(2\ell+1)!}\right]^2\,, \tag{2.33}$$

$$g_{\ell m}(\tilde{a}, \alpha, \omega) \equiv \prod_{k=1}^{\ell}\left(k^2\left(1-\tilde{a}^2\right) + \left(\tilde{a}m - 2r_+\omega\right)^2\right)\,. \tag{2.34}$$

13

Figure 8: Superradiant growth rates for the dominant vector mode $|1011\rangle$, for different values of the black hole spin $\tilde{a}$. The growth timescale is for a Proca field of mass $\mu = \hbar/10^{-9}\,\text{yr} \approx 2.1 \times 10^{-14}\,\text{eV}$. The points are numeric data, while the solid lines are the approximation (2.35). The lower panel shows the ratio of our numerics and analytics, and includes the decaying regime, $\Gamma < 0$, at larger values of α.

The dominant growing mode is $|n\ell m\rangle = |211\rangle$, and hence $\Gamma_{211} \propto \mu\,\alpha^8$ [7, 8], where we have used $\Omega_H \sim \mu\alpha^{-1}$. Numeric results for the growth rates Γ of the fastest growing scalar states are shown in Fig. 9, along with their comparison to the analytic approximations (2.32).

The instability rates for the vector modes take a very similar form. In particular, we find that they are
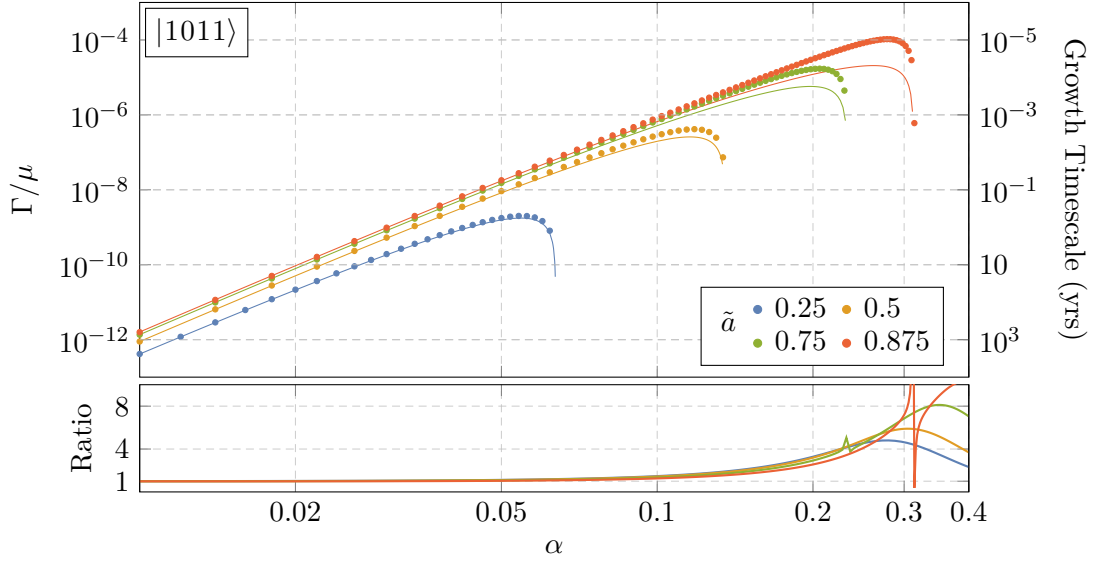
$$\Gamma_{n\ell jm} = 2\tilde{r}_+ C_{n\ell j}\, g_{jm}(\tilde{a}, \alpha, \omega)\,(m\Omega_H - \omega_{n\ell jm})\,\alpha^{2\ell+2j+5}\,, \qquad \text{for } j = \ell \pm 1, \ell\,, \tag{2.35}$$

where the coefficient,

$$C_{n\ell j} \equiv \frac{2^{2\ell+2j+1}(n+\ell)!}{n^{2\ell+4}(n-\ell-1)!}\left[\frac{(\ell)!}{(\ell+j)!(\ell+j+1)!}\right]^2\left[1 + \frac{2\,(1+\ell-j)\,(1-\ell+j)}{\ell+j}\right]^2\,, \tag{2.36}$$

is valid for all $j = \ell \pm 1, \ell$, and the function g_{jm} is obtained by replacing ℓ by j in (2.34). The α-scaling in (2.35) was also found in [20–23]. Notice that (2.35) is also valid for the scalar rate (2.32), if we set $j = \ell$ and multiply $C_{n\ell j}$ by a factor of $j^2/(j+1)^2$. The dominant vector growing mode is $|n\ell jm\rangle = |1011\rangle$ and has $\Gamma_{1011} \propto \mu\alpha^6$ [20–28]. This is faster than the dominant growing mode for the scalar field. In Fig. 8, we show our numeric results for the growth rate Γ_{1011} at different values of the black hole spin $\tilde{a}$, and compare it with (2.35). In Fig. 9, we compare our numeric results for the growth rates of other electric and magnetic vector modes to their perturbative approximations (2.35). For comparison, we also include the dominant scalar modes.

14
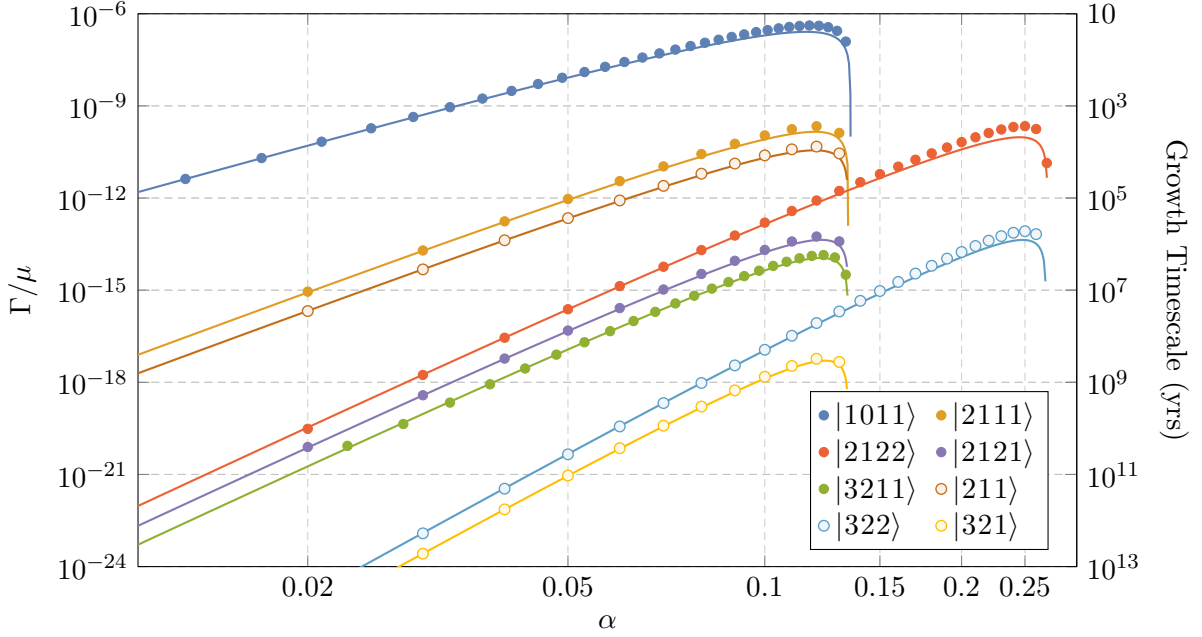
Figure 9: Superradiant growth rates for selected scalar and vector modes, for $\tilde{a} = 0.5$. The growth timescale is for $\mu = \hbar/10^{-9}\,\mathrm{yr} \approx 2.1 \times 10^{-14}\,\mathrm{eV}$. The points represent numeric data, while the solid lines are our perturbative predictions (2.32) and (2.35).

Unfortunately, the separable ansatz (2.25) for the magnetic mode does not describe the Proca field in the near-horizon geometry of the Kerr black hole, and thus cannot be used to rigorously derive a perturbative expression for the magnetic instability rates. The result (2.35) for $j = \ell$ was obtained through an educated guess and, in the absence of numerical evidence, should be taken as purely conjectural. Having said that, we find excellent agreement between this guess and our numeric results (c.f. Figures 9 and 10). and so we include it as a guide for phenomenology.

3 Analytical Computation of the Spectra

In this section, we compute in detail the energy spectra and instability rates of quasi-bound states of massive scalar and vector fields around rotating black holes, using the method of matched asymptotic expansions [42, 43]. The conceptual challenge of the computation can be illustrated using the scalar field, while avoiding the technical heft of the vector. We thus begin with the analysis of a scalar field [7, 44] in §3.1 before moving to the vector case in §3.2.

3.1 Massive Scalars around Kerr

In §2.2, we presented the Klein-Gordon equation of a massive scalar field in the Kerr spacetime. We will now solve for its spectrum of energy eigenstates. It is convenient to write the frequency eigenvalue as

$$\omega \equiv \sqrt{1 - \frac{\alpha^2}{\nu^2}}\,, \tag{3.1}$$

where the real part of ν is an integer for the leading-order Bohr spectrum. We will compute $\text{Im}\,\nu$ to leading order in α and $\text{Re}\,\nu$ to order α^3, as all degeneracies are broken at this order.

3.1.1 Matched Asymptotic Expansion

Since perturbative solutions of the scalar field radial equation (2.12) cannot capture the boundary conditions at $r = r_+$ and $r \to \infty$ simultaneously, a matched asymptotic expansion is necessary to compute the eigenvalues ν. Schematically, we approximate the radial function separately in both the near and far regions (cf. Fig. 2), and match these solutions in the region of overlap.

To define the *near region*, it is convenient to introduce the rescaled radial coordinate

$$z \equiv \frac{r - r_+}{r_+ - r_-} = \frac{r - \alpha \tilde{r}_+}{\alpha\,(\tilde{r}_+ - \tilde{r}_-)}\,, \tag{3.2}$$

where $\tilde{r}_\pm \equiv r_\pm/\alpha$, so that $\tilde{r}_\pm \sim \mathcal{O}(1)$. In this coordinate, the inner and outer horizons are mapped to $z = -1$ and $z = 0$, respectively. As discussed in §2.2, the radial function varies much more rapidly in the near region than in the far region, $\mathrm{d}R/\mathrm{d}r \sim \alpha^{-1}$, and the reason we change coordinates is to accommodate this rapid change in the α-expansion. The radial equation (2.12) then becomes

$$\frac{1}{R\,z(z+1)} \frac{\mathrm{d}}{\mathrm{d}z}\left(z(z+1)\frac{\mathrm{d}R}{\mathrm{d}z}\right) - \frac{\Lambda}{z(z+1)} - 4\gamma^2 + \frac{P_+^2}{z^2} + \frac{P_-^2}{(z+1)^2} - \frac{A_+}{z} + \frac{A_-}{z+1} = 0\,, \tag{3.3}$$

where the coefficients were defined in (2.13) and (2.14). We then expand (3.3) in powers of α, with z kept fixed. By comparing the dominant and subdominant terms at each order in α, we find that this region covers the range $0 \leq z \lesssim \alpha^{-2}$, cf. Fig. 2. Near the outer horizon at $z = 0$, the $1/z^2$ pole dominates and the radial solution scales as

$$R(z) \sim B_1\, z^{iP_+} + B_2\, z^{-iP_+}\,, \qquad z \to 0\,, \tag{3.4}$$

where B_1 and B_2 are integration constants. The purely ingoing boundary condition at the event horizon requires that $B_2 = 0$. Similarly, approaching the inner horizon at $z = -1$, we find

16

that $\lim_{z \to -1} R(z) \sim (z+1)^{\pm iP_-}$. However, unlike the outer horizon, the inner horizon is not physically accessible, and hence no boundary condition has to be imposed on it.

To identify the *far region*, it is useful to use the alternative coordinate

$$x \equiv 2\sqrt{1-\omega^2}\,(r-r_+) = 4\gamma z\,, \qquad (3.5)$$

where γ was defined in (2.14). In this coordinate, the near horizon region, $z \sim 1$, is mapped to $x \sim \alpha^2$, and the Bohr radius $r_c \sim \alpha^{-1}$ is at $x \sim 1$. In the far region, we expand the radial equation in powers of α, while keeping x fixed. As illustrated in Fig. 2, the far region spans $\alpha^2 \lesssim x < \infty$. The radial solution then behaves as

$$R(x) \sim B_3\,e^{-x/2}\,x^{-1+\nu-2\alpha^2/\nu} + B_4\,e^{+x/2}\,x^{-1-\nu+2\alpha^2/\nu}\,, \qquad x \to \infty\,, \qquad (3.6)$$

where ν was defined in (3.1). Since we are interested in quasi-bound states with $\omega < \mu$, the radial function should vanish at large distances. We therefore set $B_4 = 0$.

To perform matched asymptotic expansions at high orders in α, we expand the radial and angular functions[9]

$$X = \sum_k \alpha^k X_k\,, \qquad (3.7)$$

where $X = \{R^{\mathrm{near}}, R^{\mathrm{far}}, S\}$. Schematically, the equations of motion become

$$\Box X = \Big[\Box^{(0)} + \alpha\,\Box^{(1)} + \alpha^2\,\Box^{(2)} + \cdots\Big]\Big[X_0 + \alpha X_1 + \alpha^2 X_2 + \cdots\Big] = 0\,, \qquad (3.8)$$

where the α-expansion of the differential operators $\Box$ includes expansions of the angular and energy eigenvalues:

$$\Lambda = \sum_k \alpha^k \Lambda_k\,, \qquad \nu = \sum_k \alpha^k \nu_k\,. \qquad (3.9)$$

In order to lift the degeneracies between all modes of the spectrum, it is sufficient to go to order α^3 in Λ and $\mathrm{Re}\,\nu$. We will then solve these equations order by order in α, imposing the above boundary conditions at each order. Finally, we match the solutions in the overlap region to determine ν.

3.1.2   Leading-Order Solution

We begin with the leading-order expansion of the equations of motion, which we expect to yield the hydrogenic spectrum. However, unlike the hydrogen atom, these states will be quasi-stationary, and we must also compute their instability rates.

---

[9]It is essential that P_+ is held fixed, since an expansion of P_+ in powers of α would change the boundary condition (3.4) at the horizon. Indeed, the main reason this matched asymptotic expansion is needed at all is that, regardless of which order in α they appear, *all* terms multiplying the z^{-2} pole of (3.3) become arbitrarily important as we approach the outer horizon, $z \to 0$. It is thus crucial that we do not disturb this pole in our α-expansion, lest our approximation becomes arbitrarily bad, to a point where we must impose a different boundary condition.

At leading order, the angular equation (2.10) is

$$\left[\frac{1}{\sin\theta} \frac{\mathrm{d}}{\mathrm{d}\theta} \left(\sin\theta \frac{\mathrm{d}}{\mathrm{d}\theta} \right) - \frac{m^2}{\sin^2\theta} + \Lambda_0 \right] S_0 = 0 \,. \tag{3.10}$$

Setting $\Lambda_0 = \ell(\ell+1)$, and imposing regular boundary conditions at the antipodal points $\theta = 0$ and π, the solutions are given by the associated Legendre polynomials $S_0 = P_{\ell m}(\cos\theta)$. This is expected, since the spheroidal harmonics reduce to the ordinary spherical harmonics in the limit $\alpha \to 0$.

The leading-order near- and far-zone radial equations are

$$\left[\frac{\mathrm{d}^2}{\mathrm{d}z^2} + \left(\frac{1}{z} + \frac{1}{z+1} \right) \frac{\mathrm{d}}{\mathrm{d}z} - \frac{\ell(\ell+1)}{z(z+1)} + \frac{P_+^2}{z^2} + \frac{P_+^2}{(z+1)^2} - \frac{2P_+^2}{z} + \frac{2P_+^2}{z+1} \right] R_0^{\mathrm{near}} = 0 \,, \tag{3.11}$$

$$\left[\frac{\mathrm{d}^2}{\mathrm{d}x^2} + \frac{2}{x} \frac{\mathrm{d}}{\mathrm{d}x} + \frac{\nu_0}{x} - \frac{\ell(\ell+1)}{x^2} - \frac{1}{4} \right] R_0^{\mathrm{far}} = 0 \,. \tag{3.12}$$

Imposing the correct boundary conditions, we obtain

$$R_0^{\mathrm{near}}(z) = \mathcal{C}_0^{\mathrm{near}} \left(\frac{z}{z+1} \right)^{iP_+} {}_2F_1(-\ell, \ell+1, 1 - 2iP_+, 1+z) \,, \tag{3.13}$$

$$R_0^{\mathrm{far}}(x) = \mathcal{C}_0^{\mathrm{far}} \, e^{-x/2} x^\ell \, U(\ell+1-\nu_0, 2+2\ell, x) \,, \tag{3.14}$$

where $_2F_1$ is the hypergeometric function and U is the confluent hypergeometric function of the second kind. For integer values of $\nu_0 \geq \ell+1$, the functions U become Laguerre polynomials.

The widths of the near and far regions can be determined by comparing the terms in (3.3) that have been neglected when writing (3.11) and (3.12), to those that have been kept.[10] We find that the near and far regions are valid for $z \lesssim \alpha^{-2}$ and $x \gtrsim \alpha^2$, respectively. This means that the two regions have an overlapping region than spans the range $\alpha \lesssim r \lesssim \alpha^{-1}$ (see Fig. 2). Since (3.13) and (3.14) are approximations of the same function, they must agree over the entire overlap region. To match the solutions, it is convenient to introduce the following *matching coordinate*[11]

$$\xi \equiv \frac{x}{\alpha^\beta} = \frac{2(\tilde{r}_+ - \tilde{r}_-)}{\nu} \frac{z}{\alpha^{\beta-2}} \,, \qquad \text{with} \qquad 0 < \beta < 2 \,. \tag{3.15}$$

Requiring the α-expansions of the near and far-zone solutions to match, while keeping ξ fixed, will fix the free coefficients of the solutions and thus determine ν.

---

[10]The widths we quote for the near, far, and overlap regions are parametric statements, and so will be unaffected by higher-order corrections.

[11]The α-expansions of $R_0^{\mathrm{near}}(\xi)$ and $R_0^{\mathrm{far}}(\xi)$ are equivalent to taking the limits $z \to \infty$ and $x \to 0$, respectively. While the latter is more commonly adopted in the literature (see e.g. [7, 44]), matching in terms of ξ has the advantage that it is organized solely in powers of α. As we shall see in §3.1.3, this is a particularly useful way of organizing the matching at higher orders.

In terms of the coordinate ξ, the α-expansion of the near-zone solution is[12]

$$
\begin{aligned}
R_0^{\text{near}}(\xi) \sim \tilde{\mathcal{C}}_0^{\text{near}} \Big[& (\alpha^{\beta-2}\xi)^\ell \, (1 + \cdots) \\
& + (\alpha^{\beta-2}\xi)^{-\ell-1} \, \mathcal{I}_\ell \left(\frac{2(\tilde{r}_+ - \tilde{r}_-)}{\nu} \right)^{2\ell+1} (1 + \cdots) \Big], \quad \alpha \to 0,
\end{aligned}
\tag{3.16}
$$

where the ellipses denote expansions in powers of $(\alpha^{\beta-2}\xi)^{-1}$ with real coefficients. In the following, it will only be important that the omitted terms are purely real. We have absorbed an overall coefficient into the rescaling $\mathcal{C}_0^{\text{near}} \to \tilde{\mathcal{C}}_0^{\text{near}}$ and defined

$$
\mathcal{I}_\ell \equiv -iP_+ \frac{(\ell!)^2}{(2\ell)!(2\ell+1)!} \prod_{k=1}^\ell \left(k^2 + 4P_+^2 \right),
\tag{3.17}
$$

which is purely imaginary. Similarly, the α-expansion of the far-zone solution is

$$
\begin{aligned}
R_0^{\text{far}}(\xi) \sim \mathcal{C}_0^{\text{far}} \Big[& (\alpha^\beta \xi)^{-\ell-1} \frac{\Gamma(2\ell+1)}{\Gamma(\ell+1-\nu_0)} (1 + \cdots) + (\alpha^\beta \xi)^\ell \frac{\mathcal{K}_\ell(\nu_0)}{\Gamma(2\ell+2)\Gamma(-\ell-\nu_0)} (1 + \cdots) \\
& + (\alpha^\beta \xi)^\ell \log(\alpha^\beta \xi) \frac{1}{\Gamma(2\ell+2)\Gamma(-\ell-\nu_0)} (1 + \cdots) \Big], \quad \alpha \to 0,
\end{aligned}
\tag{3.18}
$$

where the ellipses denote expansions in powers of $\alpha^\beta \xi$, and we have defined the ν_0-dependent constant

$$
\mathcal{K}_\ell(\nu_0) \equiv \gamma_E - \psi(2\ell+2) + \psi(\ell+1-\nu_0) + \sum_{k=1}^{2\ell+1} \frac{(-1)^{k+1}\Gamma(2\ell+2)\Gamma(-\ell+\nu_0)}{2^k \, k \, \Gamma(\nu_0-\ell+k)\Gamma(2\ell+2-k)},
\tag{3.19}
$$

where $\psi(z) = \Gamma'(z)/\Gamma(z)$ is the digamma function and γ_E the Euler-Mascheroni constant. Since logarithmic terms are absent in (3.16), they do not play a role in the matching at leading order. However, these terms will appear at higher orders in the near-zone expansion and will ultimately match the logarithmic term in (3.18).

Matching the common terms in (3.16) and (3.18) allows us to solve for the frequency eigenvalue ν_0. Although there are $2\ell+1$ such terms, only the ξ^ℓ and $\xi^{-\ell-1}$ terms need to be matched at leading order. This is because they contain the dominant behaviors of R_0^{near} and R_0^{far} in the limit $\alpha \to 0$. The remaining terms are suppressed by powers of α and, like the logarithmic term above, can only be matched consistently when higher-order corrections to R_0^{near} and R_0^{far} are taken into account. Matching the coefficients of ξ^ℓ and $\xi^{-\ell-1}$, and taking their ratio, we obtain the following matching condition

$$
\frac{\Gamma(-\ell-\nu_0)\nu_0^{2\ell+1}}{\Gamma(\ell+1-\nu_0)\mathcal{K}_\ell(\nu_0)} = \alpha^{4\ell+2} \left(\frac{[2(\tilde{r}_+ - \tilde{r}_-)]^{2\ell+1}}{(2\ell!)(2\ell+1)!} \mathcal{I}_\ell + \cdots \right),
\tag{3.20}
$$

where the ellipses denote terms that are purely real. We emphasize that, although we have so far

---

only expanded the equations of motion at leading-order, higher powers of α arise in (3.20) due to the hierarchy of the coordinates $x/z \sim \alpha^2$. This is why the leading-order result for $\mathrm{Im}\,\nu$ can be $\mathcal{O}(\alpha^{4\ell+2})$.

Solving (3.20) for ν_0, we get

$$\nu_0 = n + iP_+ \left[2\alpha^2(\tilde{r}_+ - \tilde{r}_-)\right]^{2\ell+1} \frac{(n+\ell)!}{n^{2\ell+1}(n-\ell-1)!} \left[\frac{\ell!}{(2\ell)!(2\ell+1)!}\right]^2 \prod_{k=1}^{\ell}\left(k^2 + 4P_+^2\right), \quad (3.21)$$

where n is an integer, with $n \geq \ell + 1$. Substituting (3.21) into (3.1), and restoring a factor of μ, the energy spectrum reads[13]

$$\omega_{n\ell m} = \mu\left(1 - \frac{\alpha^2}{2n^2}\right) + i\Gamma_{n\ell m}, \quad (3.22)$$

where the instability rate is given by (2.32). The real part of (3.22) shows that the system has the expected hydrogen-like spectrum. However, due to the nontrivial boundary condition at the horizon, the imaginary part of (3.21) is non-vanishing and the energy eigenstates are only quasi-stationary. For $m\Omega_H > \omega$, the instability rate is positive and superradiant growth occurs.

3.1.3 Higher-Order Corrections

Next, we compute higher-order corrections to ν. We focus only on the corrections to the real part of the spectrum, since all degeneracies in the imaginary part have already been broken at leading order.

It is convenient to rearrange the α-expansion of the equations of motion (3.8) into the following form

$$\square^{(0)}X_i = -\sum_{k=0}^{i-1}\square^{(i-k)}X_k \equiv J_i^X, \quad (3.23)$$

so that the solutions of order $k < i$ are sources for the solution at order i. Expanding the angular equation (2.10) in powers of α, we obtain $J_i^\theta = 0$ and $\Lambda_i = 0$, for $i = 1, 2, 3$, which means that the angular eigenvalue and eigenstate are uncorrected up to third order:

$$\Lambda = \ell(\ell+1) + \mathcal{O}(\alpha^4), \qquad S(\theta) = P_{\ell m}(\cos\theta) + \mathcal{O}(\alpha^4). \quad (3.24)$$

This is to be expected, since any deviation between $P_{\ell m}$ and the spheroidal harmonics, which are the exact solutions of (2.10), is parametrized by the spheroidicity parameter $c^2 \sim \alpha^4$. To the order in α that we are working in, we can therefore use the leading-order angular solutions.

The asymptotic expansions of the radial functions need to be treated more carefully. We will distinguish between modes with $\ell = 0$ and $\ell \neq 0$. For the former, the radial function peaks near the horizon and the solution is especially sensitive to the near-horizon geometry.

---

[13]From the point of view of the matching procedure, the real and imaginary parts of the eigenvalue arise from the matching of the coefficients of ξ^ℓ and $\xi^{-\ell-1}$, respectively. This can be seen directly from (3.16), since the coefficient of ξ^ℓ is purely real while that of $\xi^{-\ell-1}$ has an imaginary part.

ℓ = 0 modes While the matching procedure is conceptually the same as before, the system of equations (3.23) is more challenging to solve, because the source terms J_i^X do not vanish. We solve these inhomogeneous equations via the method of *variation of parameters*, where the general solutions contain integrals over J_i^X, with the integration limits appropriately chosen such that the boundary conditions in the respective regions are satisfied. We relegate all technical details to Appendix B, and provide a more qualitative description here.

We perform the matching at higher orders by converting the radial coordinates x and z to the matching coordinate (3.15), and expanding the resulting functions in the limit $\alpha \to 0$, just as we did at leading order. However, since x and z also appear in the integration limits of the integrals mentioned above, their asymptotic expansions must be systematically organized such that no spurious divergences appear as $\alpha \to 0$; see Appendix B. At finite order in α, we expect only a finite number of the terms in $R^{\text{near}}(\xi)$ and $R^{\text{far}}(\xi)$ to match as $\alpha \to 0$. For example, for the $\ell = 0$ mode, only the terms ξ, ξ^0, $\log \xi$ and ξ^{-1} are shared between the near- and far-zone solutions at order α^2. We solve for the energy eigenvalues by matching the coefficients of these terms. Although there are generally more terms to match than unknowns, the matching is only consistent if all of these common terms match. For the $\ell = 0$ mode, this procedure yields

$$E_{n00} = \mu \left(1 - \frac{\alpha^2}{2n^2} - \frac{\alpha^4}{8n^4} + \frac{(2 - 6n)\,\alpha^4}{n^4} \right). \tag{3.25}$$

Since $\ell = 0$ implies $m = 0$, there is no hyperfine splitting $\propto m\tilde{a}\,\alpha^5$.

ℓ ≠ 0 modes Although the method of matched asymptotic expansion described so far is robust and correctly captures all boundary conditions of the radial equation, the procedure quickly becomes cumbersome for modes with arbitrary quantum numbers $\{n, \ell, m\}$. Fortunately, since the typical Bohr radii of the $\ell \neq 0$ modes are peaked in the far region, most of their support is far from the horizon. The spectra of the $\ell \neq 0$ modes can therefore be obtained by naively extending the radial solution in the far region (2.18) towards $x \to 0$ and assuming that it is regular at the origin. While this approximation does not capture the instability rates, it is sufficient for determining the real parts of the energy eigenvalues ν_i, at least up to the order of interest.[14] As shown explicitly in Appendix B, this leads to the expression (2.28) for the scalar field energy eigenvalue. This result also agrees with (3.25) obtained for $\ell = 0$ through the matched asymptotic expansion.[15] These higher-order contributions have been computed in [13] in the non-relativistic limit. Our results here, which make no such assumption, agrees with the previous result.

3.2   Massive Vectors around Kerr

Having illustrated our approach for the case of a scalar field, we are now ready to attack the more technically challenging vector field. We will treat the electric and magnetic modes of the field separately.

---

[14]We have also performed a matched asymptotic expansion for the $\ell = 1$ mode, and we found agreement with the stated approximation up to order α^5. Since the approximation gets better for larger values of ℓ, we expect the results obtained through this simplification also hold for all other $\ell \neq 0$ modes.

[15]In (2.28), the hyperfine structure naively diverges for the $\ell = 0$ mode. However, since this mode necessarily has $m = 0$, it does not actually receive a contribution from the hyperfine splitting.

3.2.1 Electric Modes

Our electric analysis relies on the separable ansatz (2.20) introduced in [34, 35]. Just like for the scalar field, we can transform the radial equation (2.24) into near and far regions through the variables z and x, defined in (3.2) and (3.5), respectively. The asymptotic behavior of the radial function as $z \to 0$ and $x \to \infty$ is

$$R(z) \sim B_1 \, z^{iP_+} + B_2 \, z^{-iP_+} \,, \qquad\qquad z \to 0 \,, \qquad (3.26)$$

$$R(x) \sim B_3 \, e^{-x/2} \, x^{+\nu - 2\alpha^2/\nu} + B_4 \, e^{+x/2} \, x^{-\nu + 2\alpha^2/\nu} \,, \qquad x \to \infty \,. \qquad (3.27)$$

The near horizon behavior is similar to that of the scalar in (3.4), since the residues of the $1/z^2$ poles are identical. The asymptotic behavior in the far region, on the other hand, differs from that of the scalar, c.f. (3.6), because the coefficients of the dR/dr term in the radial equations differ as $r \to \infty$. The purely ingoing boundary condition at the horizon requires that $B_2 = 0$, and for a quasi-bound state solution we must set $B_4 = 0$.

A crucial difference between the analysis for scalar and vector fields is the presence of additional poles at $r = \hat{r}_\pm$ in the radial equation (2.24). Since these poles are located at an $\mathcal{O}(1)$ distance from the origin of the complex-r plane, the widths of the near and far regions are now much smaller. Indeed, we find that the near and far regions cover $z \lesssim \alpha^{-1}$ and $x \gtrsim \alpha$, and therefore do not overlap. This means that the matching between these regions must be performed indirectly through an intermediate region (see Fig. 4). To describe this intermediate region, it is convenient to introduce the following coordinate

$$y \equiv r - r_+ \,. \qquad (3.28)$$

We find that the intermediate region spans the range $\alpha \lesssim y \lesssim \alpha^{-1}$, which overlaps with both the near and far regions and therefore allows the two-step matching procedure. Since no boundary conditions need to be imposed in the intermediate region, the coefficients are determined by matching the near- and far-zone solutions.

To solve the coupled differential equations (2.22) and (2.24) order-by-order in α, we now expand all relevant quantities in powers of α. The system of equations are schematically organized as in (3.8), where X now includes the intermediate radial function R^{int}. The parameters appearing in the differential operators, λ and ν, are also expanded in powers of α.

Leading-order solutions

The leading-order angular equation for the electric modes is

$$\left[\frac{1}{\sin\theta} \frac{d}{d\theta} \left(\sin\theta \frac{d}{d\theta} \right) - \frac{m^2}{\sin^2\theta} + \lambda_0(\lambda_0 - 1) \right] S_0 = 0 \,. \qquad (3.29)$$

Since the vector field has intrinsic spin, the quantum number m now describes the *total angular momentum* projected along the spin of the black hole (see Appendix A). The solutions are the associated Legendre polynomials P_{jm}, provided that the separation constant obeys $\lambda_0(\lambda_0 - 1) = j(j+1)$. In the far region, we may identify j as the total angular momentum of solution. This

22

yields the following two solutions

$$\lambda_0^+ = -j \quad \text{and} \quad \lambda_0^- = j + 1 \,. \tag{3.30}$$

To understand the physical interpretation of these solutions, it is instructive to consider the leading-order form of the ansatz $A^\mu \equiv B^{\mu\nu}\nabla_\nu Z$. Using the results of Appendix B, we find

$$A^\mu_{(0)} = \frac{\lambda_0}{\lambda_0^2 + r^2}\begin{pmatrix} -\lambda_0 & ir & 0 & 0 \\ -ir & \lambda_0 & 0 & 0 \\ 0 & 0 & 0 & 0 \\ 0 & 0 & 0 & 0 \end{pmatrix}\begin{pmatrix} \partial_t \\ \partial_r \\ \partial_\theta \\ \partial_\phi \end{pmatrix}Z_0 + \frac{1}{r^2}\begin{pmatrix} 0 & 0 & 0 & 0 \\ 0 & 0 & 0 & 0 \\ 0 & 0 & 1 & 0 \\ 0 & 0 & 0 & \csc^2\theta \end{pmatrix}\begin{pmatrix} \partial_t \\ \partial_r \\ \partial_\theta \\ \partial_\phi \end{pmatrix}Z_0 \,, \tag{3.31}$$

which is diagonal in angular gradients. At large distances $r \gg \lambda_0$, the spatial components of the vector field simplify to

$$A^i_{(0)} \propto r^{-1}R_0^{\text{far}}(r)\left(r\partial^i Y_{jm} - \lambda_0\, Y_{jm}\hat{r}^i\right)e^{-i\omega t}, \tag{3.32}$$

where Y_{jm} are the scalar spherical harmonics, and we have normalized the basis vectors with the appropriate scale factors $\{1, r, r\sin\theta\}$ in spherical coordinates. Using the relationships between the 'pure-orbital' and 'pure-spin' vector spherical harmonics in flat space [41],[16]

$$\begin{aligned} Y^i_{j-1,jm} &= \frac{1}{\sqrt{j(2j+1)}}\left[r\partial^i Y_{jm} + jY_{jm}\hat{r}^i\right], \\ Y^i_{j+1,jm} &= \frac{1}{\sqrt{(j+1)(2j+1)}}\left[r\partial^i Y_{jm} - (j+1)Y_{jm}\hat{r}^i\right], \end{aligned} \tag{3.33}$$

we see that the solutions (3.32) with eigenvalues $\lambda_0^\pm$ correspond to the $j = \ell \pm 1$ electric modes of the vector field. Furthermore, (3.32) relates R_0^{far} to the actual radial profile of the vector field at large distances, with the additional power of r^{-1} accounting for the different asymptotic behaviors of (3.6) and (3.27). This means that the usual hydrogen-like intuition still applies for all spatial components of the vector field [22, 23].[17]

The near, intermediate and far-zone radial equations are

$$\left[\frac{\mathrm{d}^2}{\mathrm{d}z^2} + \left(\frac{1}{z} + \frac{1}{z+1}\right)\frac{\mathrm{d}}{\mathrm{d}z} - \frac{\lambda_0(\lambda_0-1)}{z(z+1)} + \frac{P_+^2}{z^2} + \frac{P_+^2}{(z+1)^2} - \frac{2P_+^2}{z} + \frac{2P_+^2}{z+1}\right]R_0^{\text{near}} = 0\,, \tag{3.34}$$

$$\left[\frac{\mathrm{d}^2}{\mathrm{d}y^2} + \left(\frac{2}{y} - \frac{2y}{\lambda_0^2+y^2}\right)\frac{\mathrm{d}}{\mathrm{d}y} - \frac{\lambda_0(\lambda_0-1)}{y^2} - \frac{2\lambda_0}{\lambda_0^2+y^2}\right]R_0^{\text{int}} = 0\,, \tag{3.35}$$

$$\left[\frac{\mathrm{d}^2}{\mathrm{d}x^2} + \frac{\nu_0}{x} - \frac{\lambda_0(\lambda_0+1)}{x^2} - \frac{1}{4}\right]R_0^{\text{far}} = 0\,. \tag{3.36}$$

We see that the combination of λ_0 that appears in (3.34) is the same as that in (3.29). This

---

[16]See Appendix A for a discussion of vector spherical harmonics in spherically symmetric spacetimes.

[17]This is perhaps most obvious if we rewrite the Proca equation as the system of coupled scalar equations (4.30). In the far-field limit, the mixings vanish, and the Proca equation reduces to a set of uncoupled scalar equations (2.12).

means that the near-horizon behavior is sensitive to the total angular momentum of the vector field, instead of just its orbital angular momentum. This is to be expected since the near-horizon limit resembles a 'massless' limit of the vector field, and Teukolsky's equation for a massless gauge field in this same limit manifestly depends on the spin of the field [45]. Furthermore, we find that the dependence on λ_0 in (3.34) differs from that in (3.36). Since the $\alpha \to 0$ limit in the far region is equivalent to taking the flat-space limit, the far region is therefore only sensitive to the orbital angular momentum of the field. Indeed, solving $\lambda_0 (\lambda_0 + 1) = \ell(\ell + 1)$, we obtain

$$\lambda_0^+ = -(\ell + 1) \quad \text{and} \quad \lambda_0^- = \ell. \tag{3.37}$$

Comparing (3.30) and (3.37), we find that the eigenvalues $\lambda_0^\pm$ correspond to the $j = \ell \pm 1$ modes, which agrees with our analysis above.

Imposing the correct boundary conditions, we find

$$R_0^{\text{near}}(z) = \mathcal{C}_0^{\text{near}} \left(\frac{z}{z+1} \right)^{iP_+} {}_2F_1(-j, j+1, 1 - 2iP_+, 1 + z), \tag{3.38}$$

$$R_0^{\text{int}}(y) = \mathcal{C}_0^{\text{int}} y^{-\lambda_0} + \mathcal{D}_0^{\text{int}} y^{-1+\lambda_0} \left[\lambda_0^2 (2\lambda_0 + 1) + (2\lambda_0 - 1) y^2 \right], \tag{3.39}$$

$$R_0^{\text{far}}(x) = \mathcal{C}_0^{\text{far}} e^{-x/2} x^{\ell+1} U(\ell + 1 - \nu_0, 2 + 2\ell, x). \tag{3.40}$$

Since the intermediate region depends on both j and ℓ, the powers of the polynomials in (3.39) are determined by the angular eigenvalues (3.30). As we shall see, the fact that the term proportional to $\mathcal{D}_0^{\text{int}}$ contains two distinct y-dependences is crucial for the matching with the asymptotic expansions of the near and far-zone solutions. In the following, we will replace ℓ by j via the substitution $j = \ell \pm 1$. This is because the azimuthal number m is interpreted as m_j, so the eigenstates of the vector field are characterized by j instead of ℓ.

Since the solutions (3.38), (3.39) and (3.40) are different approximations of the same function, they must agree in the regions of overlap. Although the near and far regions do not overlap with each other, they each overlap with the intermediate region. It is therefore convenient to introduce the following matching coordinates

$$\begin{aligned} \xi_1 &\equiv \frac{x}{\alpha^\beta} = \frac{2}{\nu} \frac{y}{\alpha^{\beta-1}}, & 0 < \beta < 1, \\ \xi_2 &\equiv \frac{2(\tilde{r}_+ - \tilde{r}_-)}{\nu} \frac{z}{\alpha^{\beta-2}} = \frac{2}{\nu} \frac{y}{\alpha^{\beta-1}}, & 1 < \beta < 2. \end{aligned} \tag{3.41}$$

We match these solutions by demanding that the intermediate-zone solution has the same ξ_1 dependence as the far-zone solution, and the same ξ_2 dependence as the near-zone solution. This forces the intermediate solution to agree with the solutions in the near and far regions in the regions of overlap. This matching procedure thus fixes the coefficients and determines the frequency eigenvalues.

24

In terms of ξ_2, the α-expansion of the near-zone solution is

$$
R_0^{\text{near}} \sim \tilde{\mathcal{C}}_0^{\text{near}} \Bigg[(\alpha^{\beta-2}\xi_2)^j \left[1 + \cdots\right]
$$
$$
+ (\alpha^{\beta-2}\xi_2)^{-j-1} \mathcal{I}_j \left(\frac{2(\tilde{r}_+ - \tilde{r}_-)}{\nu} \right)^{2j+1} [1 + \cdots] \Bigg], \quad \alpha \to 0, \tag{3.42}
$$

where $\mathcal{I}_j$ was defined in (3.17), with ℓ replaced by j. For the far and intermediate-zone solutions, we have to treat the $j = \ell \pm 1$ modes separately.

Substituting $\ell = j - 1$ into (3.40) and expanding in powers of α, the far-zone solution becomes

$$
R_0^{\text{far}} \sim \mathcal{C}_0^{\text{far}} \Bigg[(\alpha^\beta \xi_1)^{-j+1} \frac{\Gamma(2j-1)}{\Gamma(j-\nu_0)} [1 + \cdots] + (\alpha^\beta \xi_1)^j \frac{\mathcal{K}_{j-1}(\nu_0)}{\Gamma(2j)\Gamma(1-j-\nu_0)} [1 + \cdots]
$$
$$
+ (\alpha^\beta \xi_1)^j \log(\alpha^\beta \xi_1) \frac{1}{\Gamma(2j)\Gamma(1-j-\nu_0)} [1 + \cdots] \Bigg], \quad \alpha \to 0, \tag{3.43}
$$

where $\mathcal{K}_{j-1}$ was defined in (3.19), with the indices appropriately replaced. Although logarithmic terms are absent in (3.42), they will appear at higher orders in the near-zone expansion, such that they can be matched with the logarithmic term in (3.43). Substituting $\lambda_0 = \lambda_0^+$ into (3.39), the intermediate-zone solution reads

$$
R_0^{\text{int}} = \tilde{\mathcal{C}}_0^{\text{int}} (\alpha^{\beta-1}\xi)^j + \tilde{\mathcal{D}}_0^{\text{int}} \left[4j^2(2j-1)(\alpha^{\beta-1}\xi)^{-j-1} + (2j+1)\nu^2 (\alpha^{\beta-1}\xi)^{-j+1} \right], \tag{3.44}
$$

where we have rescaled the coefficients $\mathcal{C}_0^{\text{int}} \to \tilde{\mathcal{C}}_0^{\text{int}}$ and $\mathcal{D}_0^{\text{int}} \to \tilde{\mathcal{D}}_0^{\text{int}}$ for future convenience. For the matchings with the far and near zones, we will use $\xi = \xi_1$ and $\xi = \xi_2$, respectively.

To determine the correct matching, we consider the behavior of the two asymptotic expansions (3.42) and (3.43) as $\alpha \to 0$. From the perspective of the near-zone solution (3.42), this limit 'zooms' in on the overlap of the near and intermediate regions, as seen 'from' the near region. The ξ_2^j term then dominates (3.42), and it must match the corresponding ξ^j term in (3.44). Similarly, if we take $\xi = \xi_1$ in the intermediate region (3.44), then the $\alpha \to 0$ limit zooms in on the overlap between the intermediate and far regions, as seen from the intermediate region. In this case, ξ_1^j also dominates, and so it must match the same term in (3.43). Thus, as we move from the near to intermediate to far regions, the dominant behavior is always ξ^j, and its coefficients in the three different regions must match.

We may also work in reverse. In the far region, the $\alpha \to 0$ limit zooms into its overlap with the intermediate region, but this time as seen from the far region. The dominant behavior now is ξ_1^{-j+1}, and this must match with the corresponding term in (3.44). Similarly, taking $\xi = \xi_2$ in (3.44), the $\alpha \to 0$ limit zooms into its overlap with the near region, though this time as seen from the intermediate region. We find that the ξ_2^{-j-1} dominates the intermediate solution and so is matched with its partner in (3.42). As we move from the far region, through the intermediate, and into the near region, the dominant behavior changes and thus the resulting matching condition is more nontrivial.

Taking the ratio of these two matching relations, we obtain

$$\frac{\Gamma(1-j-\nu_0)\,\nu_0^{2j-1}}{\Gamma(j-\nu_0)\mathcal{K}_{j-1}(\nu_0)} = \alpha^{4j}\left(\frac{(2j+1)\,[2(\tilde{r}_+ - \tilde{r}_-)]^{2j+1}}{[2j(2j-1)!]^2}\mathcal{I}_j + \cdots\right). \tag{3.45}$$

We again emphasize that, although we have expanded the equations of motion only to leading order, higher powers of α appear in (3.45) from $x/y \sim y/z \sim \alpha$. Solving for the leading-order real and imaginary parts of ν_0, and restoring factors of μ, we find

$$\omega_{n\ell jm} = \mu\left(1 - \frac{\alpha^2}{2n^2}\right) + i\Gamma_{n\ell jm}, \tag{3.46}$$

where the instability rate is given by (2.35). The dominant $j = \ell + 1$ growing mode, $|1011\rangle$, has a growth rate $\Gamma_{1011} \propto \mu\,\alpha^6$ that is much larger than the dominant growing mode in the scalar case. The $j = \ell - 1$ electric mode has the same energy spectrum (3.46), but a different instability rate $\Gamma_{n\ell jm}$; cf. (2.35). Its dominant growing mode $|3211\rangle$ has a significantly suppressed growth rate, $\Gamma_{3211} \propto \mu\,\alpha^{10}$, compared to the the dominant $j = \ell + 1$ mode.

Higher-order corrections

Finally, we compute the higher-order corrections to the real part of the frequency eigenvalues. The following is a sketch of the computation, with details relegated to Appendix B.

Due to the presence of additional θ-dependent terms on the right-hand side of (2.22), the higher-order angular equations are now harder to solve than in the scalar case. In particular, these terms induce new cross couplings in the angular eigenstates

$$S(\theta) = P_{jm}(\cos\theta) + \Delta S(\theta) + \mathcal{O}(\alpha^4),$$

$$\Delta S(\theta) = \left(\alpha^2\tilde{a}^2 b_{j-2} + \alpha^3\tilde{a}^3 c_{j-2}\right)P_{j-2,m}(\cos\theta) + \left(\alpha^2\tilde{a}^2 b_{j+2} + \alpha^3\tilde{a}^3 c_{j+2}\right)P_{j+2,m}(\cos\theta), \tag{3.47}$$

where the coefficients $b_{j\pm2}$ and $c_{j\pm2}$ are given in Appendix B. Strictly speaking, j is no longer a good quantum number at order α^2. However, as we discussed in §2.1, an approximate notion of total angular momentum still exists—especially in the $\alpha \to 0$ limit—and we continue to label our states with j, even though it has no precise physical meaning. The angular eigenvalues λ for $j = \ell \pm 1$, expanded up to order α^3, are also given in Appendix B. Substituting these results for λ into the radial equations allows us solve for the energy eigenvalues at high orders.

It is also instructive to compute the higher-order corrections to the actual vector field configuration (3.32) in the far zone

$$A_{(1)}^i \propto r^{-1}R_0^{\text{far}}\, i\tilde{a}\alpha\left(\cos\theta\,\epsilon^{ikl}r^k\partial^l\,Y_{jm} - \lambda_0\sin\theta\,Y_{jm}\,\hat{\phi}^i\right)e^{-i\omega t}. \tag{3.48}$$

Despite the presence of a magnetic vector spherical harmonic in (3.48), the vector field configuration is still of the electric type, since the $\cos\theta$ factor acquires a factor of (-1) under a parity transformation. The presence of the $\hat{\phi}^i$-term in (3.48) is a manifestation of the fact that spherical symmetry is already broken at this order in α.

$\ell = 0$ modes   We first consider the dominant growing mode, with $j = 1$ and $\ell = 0$. Since the radial wavefunctions are peaked near the horizon, they are most sensitive to strong gravity effects. This sensitivity manifests itself through the failure of ordinary perturbation theory, which diverges for this mode. It is not clear how to regulate these divergences, and thus this technology of matched asymptotic expansions is necessary to derive this mode's fine and hyperfine structure. The matching procedure at higher orders is the same as that illustrated in §3.1.3, except that the matching between the near and far-zone solutions must be performed through the intermediate zone. We find that these higher-order intermediate-zone solutions take the form of simple linear combinations of powers and logarithms of y, which can be matched with the corresponding terms found in the asymptotic expansions of the near and far-zone solutions. Performing the matched asymptotic expansion up to third order, we find

$$E_{n01m} = \mu \left(1 - \frac{\alpha^2}{2n^2} - \frac{\alpha^4}{8n^4} + \frac{(6 - 10n)\,\alpha^4}{3n^4} + \frac{8\tilde{a}m\alpha^5}{3n^3} \right). \tag{3.49}$$

Since the vector field has intrinsic spin, the $\ell = 0$ modes now have hyperfine splittings $\propto \tilde{a}m\alpha^5$.

$\ell \neq 0$ modes   Since the $\ell \neq 0$ modes peak in the far zone, the calculation of the higher-order corrections of their spectra can be simplified by naively extrapolating the far-zone solution (3.40) towards the horizon $x \to 0$ and imposing regular boundary conditions there. The far-zone radial function and the eigenvalues are then solved as an expansion in powers of α. This leads to the result (2.30) for the energy eigenvalues. Remarkably, we find that (2.30), obtained through this simplified treatment, agrees with (3.49), which was derived more rigorously through matching (see Appendix B for a more detailed discussion).

3.2.2   Magnetic Modes

In principle, the task of solving for the magnetic mode spectrum involves a straightforward application of the machinery developed in previous sections to the relevant separated radial and angular equations. Unfortunately, these equations are not yet known, except at linear order in $\tilde{a}$ [20, 21]. In this section, we discuss the extent to which the approximate radial equation (2.26) can be used to derive the energy spectrum and instability rates. Our discussion will be brief and mostly qualitative, since our solutions are similar to those found in previous sections.

Leading-order solution

In the far region, the electric (3.36) and magnetic (2.26) radial equations are of the same form at leading order, with $\lambda_0(\lambda_0 + 1)$ replaced with $j(j + 1)$ [21, 36]. The magnetic quasi-bound states therefore take the same form as their electric counterparts in the far region (3.32), and

$$A_{(0)}^i \propto r^{-1} R_0^{\text{far}}(r)\, Y_{j,jm}^i(\theta, \phi)\, e^{-i\omega t}\,. \tag{3.50}$$

As expected, these magnetic modes are therefore also hydrogenic [22, 23] and the spectrum is Bohr-like to leading order in α.

In the previous sections, we derived the leading-order instability rates by finding the near- and far-zone solutions, and matched them in the overlap region. One might hope to do the same
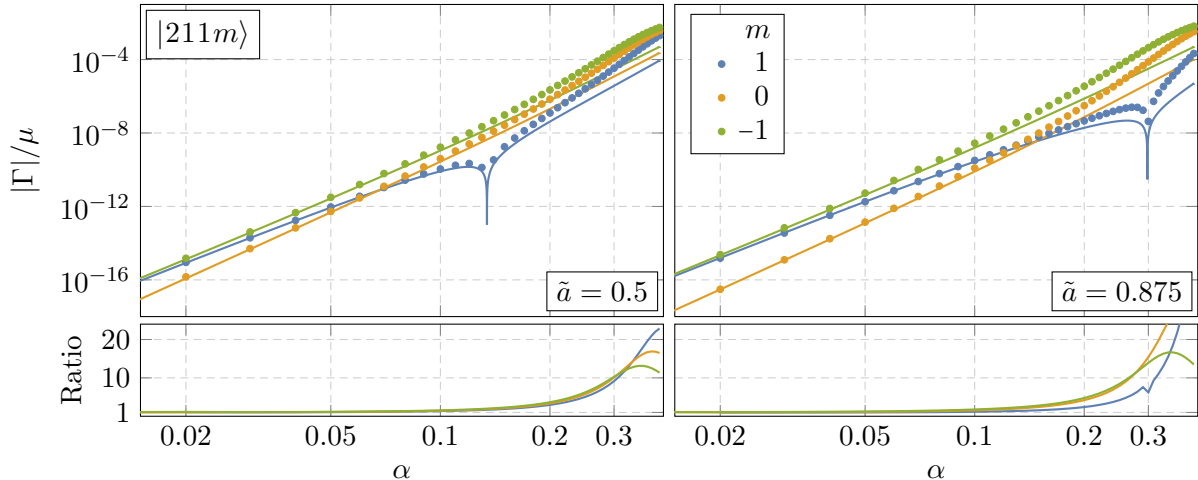
Figure 10: Instability rates for the magnetic mode $|211m\rangle$, for $\tilde{a} = 0.5$ (left) and $\tilde{a} = 0.875$ (right). We compare our numeric results (denoted by points) with the conjectured form of the instability rate (solid lines), and plot the ratio of numerics to analytics in the lower panels.

with (2.26) to derive the magnetic instability rates to linear order in $\tilde{a}$. However, since the radial equation was derived in the far region, extending it into the near region is not as innocuous as it naively seems. This is because the near region—and especially the boundary condition at the outer horizon—is sensitive to the full nonlinear spin-dependence of the metric. As we discussed in Footnote 9, getting these important terms wrong in our perturbative expansion can cause our approximation to deviate strongly from the actual solution, and it is not clear how to infer the correct behavior from a far-zone solution at linear order in $\tilde{a}$.[18]

We will instead guess the form of the magnetic instability rate and check this guess against our numerics. It is natural to assume that the magnetic instability rates take the same functional form as the rates for the scalar field (2.32) and the electric modes of the vector field (2.35). The overall normalization and the dominant α-scaling can be fixed by demanding that this ansatz matches the Schwarzschild limit [36], and thus we arrive at the conjectural instability rate (2.35) with (2.36). As we show in Fig. 10, we find our guess to be in excellent agreement with our numeric results for small α, even at high values of $\tilde{a}$. However, we emphasize that this formula represents our best educated guess for the magnetic instability rate at arbitrary spin and is *not* rigorously derived. A conclusive analytic result can only be found by solving a separable equation valid for all $\tilde{a}$.

---

[18]The authors of [20, 21] were able to derive an accurate expression for the magnetic instability rate to linear order in $\tilde{a}$, by matching the solution in the far region to a near-zone solution that is obtained by extrapolating (2.26) toward the outer horizon $r_+ = 2\alpha$. However, they needed to discard terms like $\check{P}_+^2$, which contains both constant and linear-in-$\tilde{a}$ pieces, to obtain a finite result. In effect, discarding these divergent terms imposes the correct near-horizon behavior.
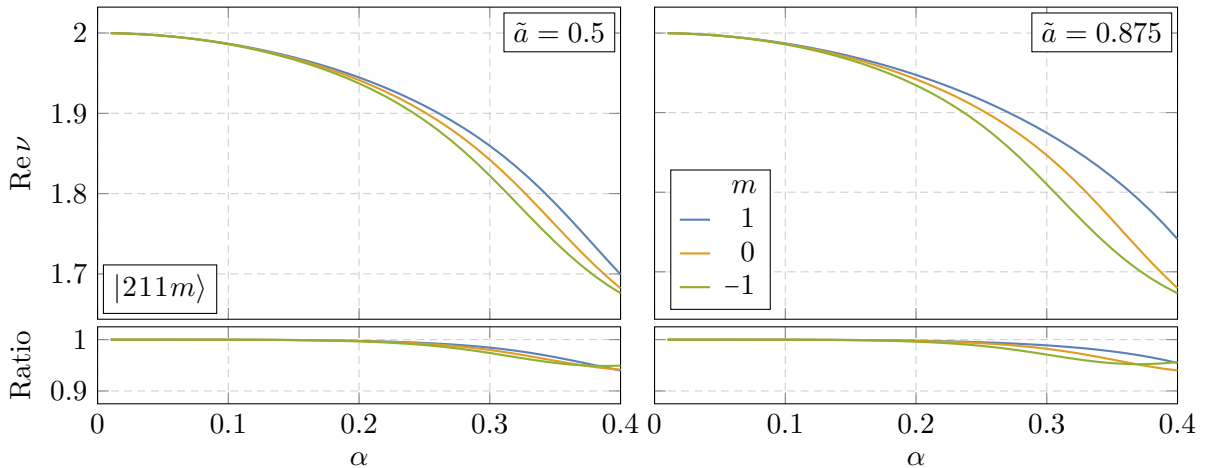
Figure 11: Numeric results for the spectra of the magnetic mode $|211m\rangle$, for $\tilde{a} = 0.5$ (left) and $\tilde{a} = 0.875$ (right). The ratios of the numeric results to their perturbative predictions (2.30) are shown in the panels below.

Higher-order corrections

Since the linear-spin approximation does not fully capture the leading-order behavior of the near region, we cannot use (2.26) to perform a matched asymptotic expansion at high orders in α. Fortunately, the magnetic modes have non-vanishing orbital angular momentum and are thus peaked far away from the horizon. As we have illustrated for both the scalar and the electric modes of the vector, we may derive the energy spectrum of these modes to $\mathcal{O}(\alpha^3)$ by extending the far-zone radial solutions (3.40) toward the horizon, imposing regular boundary conditions, and solving for ν perturbatively in powers of α. This then yields the fine and hyperfine structure of the magnetic modes to linear order in $\tilde{a}$. However, following the pattern suggested by the electric modes in the spectrum, we expect the fine structure to be independent of $\tilde{a}$, and the hyperfine structure to be proportional to $m\tilde{a}$, so that our results for the magnetic energy spectrum should be valid for arbitrary spin. In Figure 11, we compare the approximation (2.30) to our numeric results and find that it is very accurate even at large $\tilde{a}$, suggesting that our extrapolation of the fine and hyperfine structure to arbitrary $\tilde{a}$ is correct.

4 Numerical Computation of the Spectra

The analysis of the previous section required α to be small, and we derived rigorous results only for the scalar field and the electric modes of the vector field. In this section, we numerically solve for the quasi-bound state spectrum, providing results for arbitrary values of α and $\tilde{a}$, including the magnetic modes of the vector field. We will thus be able to use these results to determine when the perturbative approximations summarized in §2.4 break down. In §4.1, we first illustrate our approach using the scalar field. We discuss why precise results for $\alpha \ll 1$ are difficult to achieve numerically and how to surmount these difficulties. In §4.2, we then solve the analogous problem for the vector field.

4.1 Massive Scalars around Kerr

The quasi-bound state spectrum of Klein-Gordon fields in the Kerr background has been studied in many previous works; see e.g. [8, 46]. To make contact with the literature, we will begin by reviewing the continued fraction method for determining the scalar spectrum (§4.1.1). We will discuss the main limitations of the method and show how they can be overcome by reformulating the problem as a nonlinear eigenvalue problem (§4.1.2). We then use this to solve for the scalar spectrum (§4.1.3).

4.1.1 Continued Fraction Method

In §2.2, we expanded the field Φ in spheroidal harmonics and obtained the radial differential equation (2.12). For the numerical analysis, it will be convenient to write the radial function as

$$R(r) = \frac{(r - r_+)^{iP_+}}{(r - r_-)^{iP_-}} B(x) , \tag{4.1}$$

where $x = 2\sqrt{1 - \omega^2}(r - r_+)$, as in §3.1 and (3.5). For quasi-bound state solutions, $B(x)$ approaches a constant at the horizon, $x \to 0$, and decays exponentially $B(x) \sim e^{-x/2}$ at spatial infinity, $x \to \infty$. Any function with these properties can be represented by a linear combination of associated Laguerre polynomials $L_k^{(\rho)}(x)$ multiplied by $e^{-x/2}$,

$$B(x) = \sum_{k=0}^{\infty} b_k \, e^{-x/2} L_k^{(\rho)}(x) . \tag{4.2}$$

In general, the expansion in (4.2) transforms the scalar radial equation (2.12) into a five-term recursion relation for the coefficients b_k. However, by choosing $\rho = 2iP_+$, one obtains the three-term recursion relation

$$\alpha_k b_{k+1} + \beta_k b_k + \gamma_k b_{k-1} = 0 , \tag{4.3}$$

where, in the notation of §2.2, we have defined

$$\begin{aligned}
\alpha_k &\equiv (k + 1)(k - c_1 + c_2 + 2 + 2iP_+ - 4\gamma) , \\
\beta_k &\equiv -2k^2 + (c_1 - 2(1 + c_2 + 2iP_+)) \, k - c_2(1 + 2iP_+) - c_3 , \\
\gamma_k &\equiv (k + 2iP_+)(k + c_2 - 1) ,
\end{aligned} \tag{4.4}$$

with

$$c_1 \equiv 2\left(1 + i(P_+ - P_-) - 2\gamma\right),$$

$$c_2 \equiv 1 + i(P_+ - P_-) + \frac{1}{4\gamma}(\gamma_+^2 - \gamma_-^2),$$ (4.5)

$$c_3 \equiv (P_+ - P_-)^2 - i(P_+ - P_-) + 2\gamma(1 + 2iP_+) + \gamma^2 + \gamma_+^2 + \Lambda.$$

For any initial data b_0 and b_1,[19] we can iteratively solve (4.3) for b_k and thereby find a solution to the radial equation (2.12).[20] However, for generic values of ω, solutions to (4.3) diverge as $k \to \infty$, so that $B(x)$ will grow—rather than decay—exponentially at spatial infinity. This is the discrete analog of the fact that the boundary conditions (2.15) can only be satisfied simultaneously at special values of ω and that, for generic ω, the solutions that satisfy the ingoing boundary condition at $r = r_+$ diverge as $r \to \infty$.

It is only for special values of ω—the quasi-bound state frequencies—that the recurrence relation (4.3) admits a *minimal solution*, which is finite both as $k \to 0$ and $k \to \infty$ [47]. Denoting the two linearly-independent solutions of (4.3) as f_k and g_k, the solution f_k is minimal if

$$\lim_{k\to\infty} \frac{f_k}{g_k} = 0.$$ (4.6)

A theorem by Pincherle [47] states that the recurrence relation (4.3) admits a minimal solution if and only if ω solves the continued fraction equation

$$\frac{\beta_0}{\alpha_0} = \cfrac{\gamma_1}{\beta_1 - \cfrac{\alpha_1\gamma_2}{\beta_2 - \cfrac{\alpha_2\gamma_3}{\beta_3 - \cdots}}}.$$ (4.7)

Determining the quasi-bound state spectrum is therefore reduced to the much simpler problem of finding the roots of a transcendental equation. This method has been used to find the quasi-normal modes of massless perturbations about Kerr black holes [48] and the quasi-normal modes and quasi-bound state spectra of massive fields [8, 21, 36, 49].

As will become apparent, sensitivity to numerical errors is a common challenge in finding the spectrum for a massive field about Kerr, and it is important to use methods that tamp down numerical errors as much as possible. For instance, the fact that the coefficients b_k diverge exponentially quickly when ω is not exactly a quasi-bound state frequency means that, unless properly accounted for, numerical errors will grow at the same rate. Solving for ω typically involves starting with an initial seed and stepping towards the solution through a sequence of intermediate frequencies, and large errors introduced during these intermediate steps can impact the accuracy of the 'solution.' As seen in Fig. 12, one needs to include several hundred of the coefficients b_k to accurately compute the decay rates $\Gamma_{n\ell m}$, so this exponential growth in error—which scales with the number of coefficients—can be an enormous problem. The major advantage

---

[19] By convention, we define $b_{-1} \equiv 0$.

[20] An alternative recursion relation was derived in [8] by performing a different mode expansion. Although the detailed forms of these coefficient functions change if we use this expansion, our discussion does not.
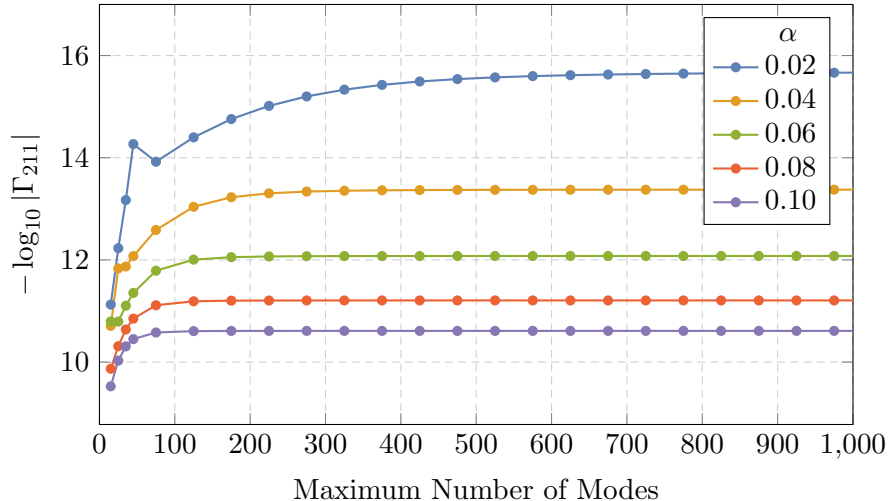
Figure 12: The imaginary part of ω slowly converges for small α, requiring about 1000 modes (terms in the continued fraction) to achieve accurate results for $\alpha \sim 0.02$. The results shown in the figure are for the $\ell = 1$, $m = 1$ mode, with $\tilde{a} = 0.5$, but similar conclusions apply to other states. Identical results apply to the recursion relation used in [8].

of phrasing this as the continued fraction (4.7) is that there exist numerically robust methods—for instance, the modified Lentz method [50]—for efficiently and accurately evaluating the continued fraction to a specified precision, which can then be passed to standard root-finding methods (i.e. Newton-Raphson) to find the eigenfrequencies.

The main issue with the continued fraction method is its rigidity—one must first separate the partial differential equation and then find a basis of functions, like $e^{-x/2}L_k^{(2iP_+)}$, that reduces the scalar radial equation (2.12) to a three-term recurrence relation.[21] This is problematic for two reasons. The first reason is simply that it is not always possible to find such a basis—for instance, it is not clear that there exists a separable ansatz for the magnetic modes of a vector field, or that there exists a basis of functions that reduces (2.24) to a relation like (4.3). The second reason is more subtle. We have seen, in Fig. 12, that several hundred modes are needed to achieve accurate results for the growth rate of the main superradiant mode $|211\rangle$. But the radial profile of this mode does not oscillate wildly and is instead quite smooth. So, why are all of these modes needed? The problem is that, as we discussed in §2.2, the solution in the near region varies on extremely short scales, $\Delta x \sim \alpha^2$, while the basis functions $e^{-x/2}L_k^{(2iP_+)}(x)$ naturally vary on much larger scales, $\Delta x \sim 1$. A large number of modes are therefore needed to approximate this (relatively) rapid behavior in the near region, and the number of required modes increases the smaller this region gets. As we will discuss shortly, the numerical error often scales with the size of a problem, and thus it can be computationally difficult to access reliable results at small α with these methods.

---

[21]One can sometimes convert a five-term recurrence relation into a three-term relation using Gaussian elimination [51]. However, it will be more convenient to bypass (4.7) entirely.

4.1.2 Nonlinear Eigenvalue Problem

The rigidity of the continued fraction method presents a serious obstacle to efficiently and accurately computing the quasi-bound state spectrum of scalar and vector fields. However, we can make progress by recognizing that the recurrence relation (4.3) is analogous to the infinite-dimensional matrix equation

$$\mathcal{M}(\omega)\,\mathbf{b} = \begin{pmatrix} \beta_0 & \alpha_0 & 0 & 0 & 0 & \dots \\ \gamma_1 & \beta_1 & \alpha_1 & 0 & 0 & \dots \\ 0 & \gamma_2 & \beta_2 & \alpha_2 & 0 & \dots \\ 0 & 0 & \gamma_3 & \beta_3 & \alpha_3 & \dots \\ \vdots & \vdots & \vdots & \vdots & \vdots & \ddots \end{pmatrix} \begin{pmatrix} b_0 \\ b_1 \\ b_2 \\ b_3 \\ \vdots \end{pmatrix} = 0\,, \tag{4.8}$$

whose elements are nonlinear functions of ω. When we decompose $B(x)$ onto a basis of functions that individually satisfy the boundary conditions (2.15) and then truncate to a finite set of size $N+1$, this becomes a *nonlinear eigenvalue problem*, i.e. we must find pairs ω and $\mathbf{b}$ such that (4.8) is satisfied [46]. For a recent review of the numerical techniques developed to attack these problems, see [52].

There are two sources of error in using (4.8) to solve for ω. The first is truncation error—in order to actually solve this matrix equation on a computer, we must truncate the representation of $B(x)$ to a finite number of coefficients. We similarly needed to truncate the number of 'levels' in the continued fraction (4.7) to actually evaluate it. This truncation introduces an error, as $B(x)$ is now *approximated* by a smaller collection of functions. As we increase the size of this collection, we are able to more faithfully represent $B(x)$ and, as seen in Fig. 12, this truncation error will decrease. We can then estimate the accuracy of our solution by how sensitive it is to changes in N. The second source of error is numerical error. Floating point arithmetic is inherently noisy, as there are round off errors incurred after every operation (e.g. addition and multiplication), and this noise can be amplified by careless numerics. Unfortunately, this error grows with the number of operations performed, and thus with the number of coefficients we include in (4.8). This is potentially disastrous, since, if we try suppress truncation error by increasing N, we could be overrun by this numerical error. We will specifically choose a representation of (4.8) to help sooth these numeric problems. In the following, we will motivate and explain these choices, and discuss them in more detail in §C.4.

Regardless of representation, numerical errors can also creep in when we try to numerically solve (4.8), and it is important to use methods that avoid such instabilities. For instance, perhaps the simplest way to determine the quasi-bound state spectrum is to find the roots of the equation $\det \mathcal{M}(\omega) = 0$. Unfortunately, this is not feasible for large N. In order for the determinant to vanish, there must be sensitive cancellations between a large number of operations, and accumulated roundoff errors can totally destroy the accuracy of our solution. This is a common problem for any nearly-singular matrix—a rule of thumb is that relative errors are amplified by the so-called condition number, the ratio of the matrix's largest and smallest eigenvalues, and this condition number diverges for exactly the frequencies we are solving for. For small α and large matrices, this numerical error easily dominates the instability rates and energy splittings.

We will instead use nonlinear inverse iteration [46, 52], a form of Newton's method applied directly to $\mathcal{M}(\omega)\mathbf{b} = 0$ that iteratively solves for both ω and $\mathbf{b}$. This method circumvents the numerical instability caused by these nearly-singular matrices because this error is amplified much more along the singular direction—i.e. the one we are interested in—than any other. That is, these errors only change the length of the solution $\mathbf{b}$ and not its direction, and so their effect is nullified. In practice, this method converges both quickly and accurately as long as one has a good initial guess for the pair $(\omega, \mathbf{b})$.

4.1.3 Chebyshev Interpolation

We will now apply the algorithm sketched in the previous subsection to the case of the scalar field in the Kerr background. As shown in §2.9, the scalar modes are separable into radial and angular functions. It is convenient to write the radial function as

$$R(r) = \left(\frac{r - r_+}{r - r_-}\right)^{iP_+} (r - r_-)^{-1+\nu-2\alpha^2/\nu} e^{-\alpha(r-r_+)/\nu} B(\zeta)\,, \tag{4.9}$$

where the asymptotic behavior shown in (3.4) and (3.6) has been extracted explicitly. The remaining function $B(\zeta)$ is defined on the finite interval $\zeta \in [-1,1]$ via a map $\zeta(r)$. Different choices of $\zeta(r)$ will be discussed below. We will work with ν, defined in (3.1), instead of ω. The function $B(\zeta)$ satisfies a linear differential equation of the form

$$\mathcal{D}_\nu[B(\zeta)] \equiv \left(\frac{\partial^2}{\partial \zeta^2} + \mathcal{C}_1(\nu, \zeta)\frac{\partial}{\partial \zeta} + \mathcal{C}_2(\nu, \zeta)\right) B(\zeta) = 0\,, \tag{4.10}$$

where the precise form of the functions[22] $\mathcal{C}_i(\nu, \zeta)$ depend on our choice of $\zeta(r)$. The function $B(\zeta)$ will satisfy the correct boundary conditions if it approaches a constant at both the outer horizon ($\zeta = -1$) and spatial infinity ($\zeta = 1$). Because (2.12) has no singularities between the outer horizon and spatial infinity, $B(\zeta)$ is necessarily a smooth function for all $\zeta \in [-1,1]$, and we may represent it in a variety of ways. For computational simplicity, we will use Chebyshev polynomials of the first kind—defined by $T_n(\cos t) = \cos nt$ and described at length in §C.4—but our conclusions will largely be independent of this choice.

Above, we derived the recurrence relation (4.3) by projecting both $B(x)$ and the radial equation (2.12) onto Laguerre functions. We could now mimic this procedure by first constructing a *polynomial projection* of $B(\zeta)$ in terms of the Chebyshev polynomials,

$$B_N(\zeta) = \sum_{k=0}^{N} b_k T_k(\zeta)\,, \tag{4.11}$$

which is a degree-N polynomial that is guaranteed to converge $\lim_{N\to\infty} B_N(\zeta) = B(\zeta)$, since B is smooth on $\zeta \in [-1,1]$ and the Chebyshev polynomials form a complete set. Projecting the radial equation (4.10) onto the Chebyshev polynomials, we would obtain the matrix equation

---

[22]These functions also depend on α, $\tilde{a}$, and the orbital and azimuthal quantum numbers ℓ and m, respectively. We will suppress this dependence, as it does not play a crucial role in our story.

$\sum_k \mathcal{M}_{nk}(\nu)b_k = 0$, where[23]

$$\mathcal{M}_{nk}(\nu) \equiv \frac{2}{\pi} \int_{-1}^{1} d\zeta \, \frac{T_n(\zeta) \, \mathcal{D}_\nu[T_k(\zeta)]}{\sqrt{1-\zeta^2}} \,. \tag{4.12}$$

The matrix given by (4.12) is similar to that in (4.8), though it has many more non-zero elements. We could again pass this to a solver to determine the quasi-bound state spectrum, but unfortunately this formulation of the problem proves (cf. §C.4) to be numerically unstable, it is difficult to reduce truncation errors without numerical errors biting back.

To circumvent this problem, we will represent $B(\zeta)$ not by its Chebyshev coefficients, but by its values at the *Chebyshev nodes*

$$\zeta_n = \cos\left(\frac{\pi(2n+1)}{2N+2}\right), \quad \text{where} \quad n = 0, 1, \ldots, N \,. \tag{4.13}$$

Introducing the associated *cardinal polynomials* $p_k(\zeta)$—degree-N polynomials that are defined by $p_k(\zeta_n) = \delta_{nk}$ (cf. §C.4)—we may rewrite (4.11) as

$$B_N(\zeta) = \sum_{k=0}^{N} B(\zeta_k) \, p_k(\zeta) \,. \tag{4.14}$$

Note that this is nothing more than a reorganization of (4.11) in a different basis of degree N polynomials such that the values of $B(\zeta)$ appear explicitly. Furthermore, because the operator $\mathcal{D}_\nu[B(\zeta)]$ appearing in (4.10) also defines a smooth function on $\zeta \in [-1,1]$, we can also represent it by its values at these specified points. This means that we can approximate (4.10) by the matrix equation

$$\sum_{k=0}^{N} \mathcal{M}_{nk}(\nu)B(\zeta_k) = 0 \,, \tag{4.15}$$

where

$$\mathcal{M}_{nk}(\nu) \equiv p_k''(\zeta_n) + \mathcal{C}_1(\nu, \zeta_n) \, p_k'(\zeta_n) + \mathcal{C}_2(\nu, \zeta_n) \, \delta_{nk} \,. \tag{4.16}$$

In practice, this formulation proves to be both simpler and more numerically robust than (4.12), as long as $p_k''(\zeta_n)$ and $p_k'(\zeta_n)$ are computed using (C.49) and (C.50), respectively. See §C.4 for more details.

The specific form of the mapping $\zeta(r)$ can dramatically affect the truncation error. Just like the convergence of a Laurent series about a point is set by the largest *circular* domain of analyticity, the convergence of the interpolation (4.14) is set by the largest *ellipsoidal* domain of analyticity about the interval $\zeta \in [-1,1]$. Specifically, it can be shown (cf. Appendix C.4) that the largest disagreement between the function and its Chebyshev interpolation anywhere on the interval scales as

$$\|B - B_N\| \sim \mathcal{O}(\rho^{-N}) \,. \tag{4.17}$$

---

[23]This formula must be multiplied by a factor of $1/2$ when $n = 0$.

The parameter ρ measures the size[24] of the largest ellipse with foci at $\zeta = \pm 1$ inside which $B(\zeta)$ is analytic. The interpolation thus converges more slowly the closer a singularity of $B(\zeta)$ is to the interval $\zeta \in [-1, 1]$, as measured by these ellipses.

The radial equation (2.12) has an additional singularity at $r = r_-$, which maps to a singularity in $B(\zeta)$ at $\zeta_- = \zeta(r_-)$. This is why our choice of $\zeta(r)$ can affect the truncation error. If this mapping does not place ζ_- far from the interval $\zeta \in [-1, 1]$, this singularity can drastically increase the number of modes N needed to accurately approximate the solution. This is also why we avoided introducing factors of r in the ansatz (4.9), as they could introduce inessential singularities into $B(\zeta)$ and potentially affect convergence.

Our choice of mapping $\zeta(r)$ will also determine how the interpolation points (4.13) sample the radial domain $[r_+, \infty)$. As we have argued in §4.1.1, one of the reasons the Laguerre basis performed so poorly was that it naturally varies on scales much larger than the width of the near region and so it has trouble approximating the behavior there. This is easier to see if we note that this Laguerre basis samples the function $B(x)$ at the zeros of $L_{N+1}^{(2iP_+)}(x)$ [53], whose smallest root scales as $\mathcal{O}(N^{-1})$. We would thus need to include $\mathcal{O}(\alpha^{-2})$ modes to accurately sample the boundary layer $x \sim \mathcal{O}(\alpha^2)$, in good agreement with the numerical experiments shown in Fig. 12. One of the benefits of the Chebyshev basis is that the interpolation points (4.13) have a much higher density $\Delta\zeta \sim \mathcal{O}(N^{-2})$ near the boundary than in the interior $\Delta\zeta \sim \mathcal{O}(N^{-1})$, which makes it easier for the basis to resolve phenomena in the near region. Still, we must be careful that the mapping we choose does not obstruct this useful behavior.

The simplest choice that maps the triplet $r = (r_-, r_+, \infty)$ to $\zeta = (-\infty, -1, 1)$ is

$$\zeta_1(r) = \frac{r - 2r_+ + r_-}{r - r_-} \,. \tag{4.18}$$

A drawback of this mapping is that the Bohr peak at $r_c \sim \nu/\alpha$ is mapped to $\zeta_1(r_c) \sim 1 - \mathcal{O}(\alpha^2)$, while the middle of the interval $\zeta = 0$ corresponds to $(2r_+ - r_-) = \mathcal{O}(\alpha)$. This creates the opposite problem as with the expansion into Laguerre polynomials—we are now sampling the near-horizon region very well, but at the expense of the far region. To ensure the far region is also well-sampled, we again require a relatively large number of modes $N \sim \alpha^{-1}$, although the properties of the Chebyshev nodes help alleviate this problem somewhat compared to the expansion (4.2). In practice, this map works fairly well for the $n = \ell + 1$ quasi-bound states, as they have very little structure in the far region.

An alternative mapping that avoids this problem is

$$\zeta_2(r) = \frac{r - \sqrt{4r_+(r - r_-) + r_-^2}}{r - r_-} \,. \tag{4.19}$$

This maps the Bohr radius to $\zeta_2(r_c) \sim 1 - \mathcal{O}(\alpha)$, which means that we only need $N \sim \mathcal{O}(\alpha^{-1/2})$ modes to resolve the far region. While the singularity at r_- is only mapped to the finite point

---

[24]Concretely, ρ is the sum of the semi-major and semi-minor axes of the ellipse with foci at $\zeta = \pm 1$. The parametric form of this ellipse is given by (C.39) and it is depicted in Fig. 16.
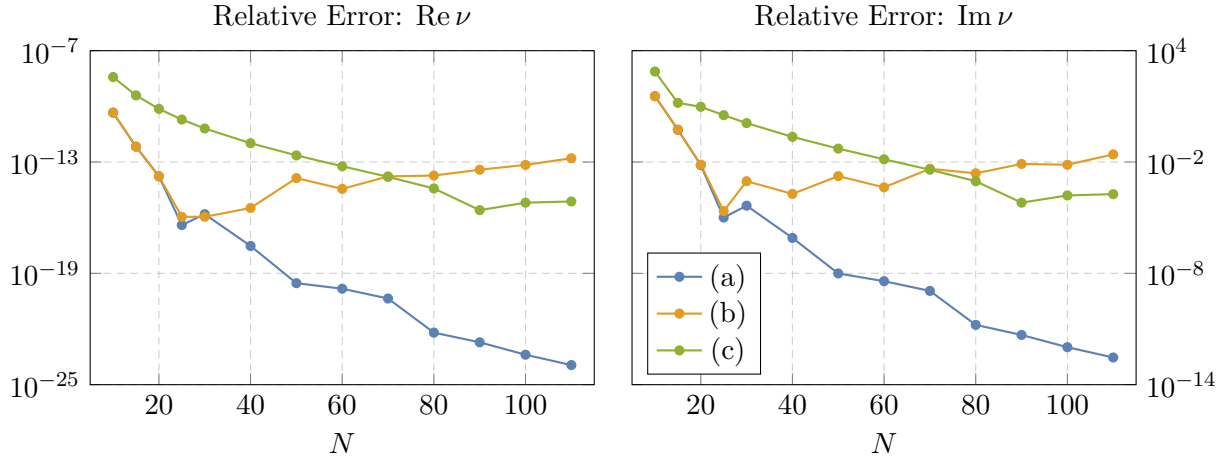
Figure 13: Comparison between the two mappings $\zeta_1(r)$ and $\zeta_2(r)$ defined in (4.18) and (4.19), as a function of the number of modes N. The displayed lines are: (a) [blue] ζ_2 with 60 digits of precision, (b) [orange] ζ_2 with machine precision, (c) [green] ζ_1 with either 60 digits of precision or with machine precision. The data shown in the figures is for $\alpha = 0.01$, $\tilde{a} = 0.5$, and $|n\ell m\rangle = |211\rangle$. All relative errors are measured with respect to the high precision ζ_2 result with $N = 120$.

$\zeta_- = -(2r_+ - r_-)/r_-$, it is still displaced far enough from the interval that it does not dramatically affect convergence. For instance, $\rho > 2$ in (4.17) as long as $\tilde{a} \lesssim 0.96$ and so ζ_2 is an effective map except in the extremal limit. In principle, there are better maps that send r_- infinitely far from the interval and more equally distribute the interpolation points (4.13) across the near, intermediate, and far regions. However, the map ζ_2 works well enough in practice that we will not pursue others.

A comparison between the two maps ζ_1 and ζ_2 is shown in Fig. 13. We see that we can achieve very accurate results for the parameter ν using only $N \sim 30$ modes. For comparison, reaching a similar level of accuracy using the continued fraction method requires $N \sim 10^4$ modes. Clearly, the map ζ_2 converges much more quickly than ζ_1, and becomes limited by the resolution $\epsilon \sim 10^{-16}$ of machine precision numbers (the 'machine epsilon') very quickly.

This method was used to determine the spectra of the $|21m\rangle$ and $|32m\rangle$ modes in Figures 6 and 9. In particular, the extremely small decay rates $\Gamma/\mu \sim 10^{-24}$ of the $|32m\rangle$ modes are accurately computed using only $N = 60$. In contrast, the continued fraction method requires $N \sim 2 \times 10^4$ modes to achieve comparable precision! With the scalar now solved, we can turn our attention to the vector.

4.2 Massive Vectors around Kerr

The quasi-bound state spectrum of Proca fields in the Kerr background has been studied only relatively recently; see e.g. [20–28, 35]. Progress has been impeded by the fact that a separable ansatz is only known [35] for the electric modes of the vector field. We used this ansatz, in §3.2, to find perturbative results for both the energy splittings and growth rates for these electric modes.
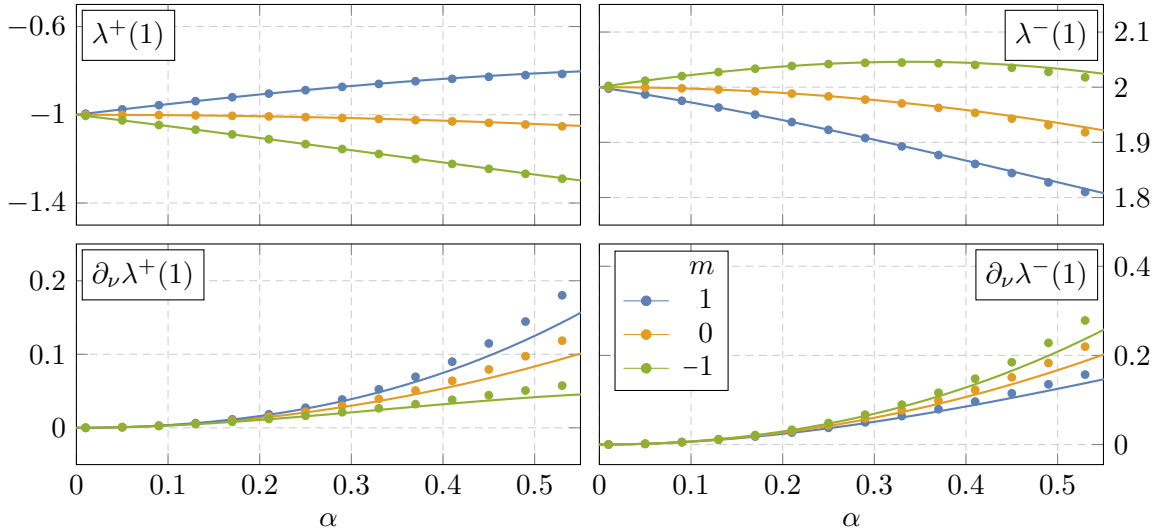
Figure 14: Comparison between the numeric (dots) and perturbative (solid) results for the angular eigenvalues $\lambda^{\pm}$ (top row) and their derivatives with respect to ν (bottom row) for $\tilde{a} = 0.5$, $j = 1$, and $\nu = 1$. The perturbative expressions (B.15) only compute the derivatives $\partial_\nu \lambda^{\pm}$ to next-to-leading order and thus deviate from the numeric results significantly at large α.

In §4.2.1, we will show how to modify the techniques developed above for the separated equations (2.22) and (2.24). This yields an efficient, accurate, and robust method for computing the spectra at arbitrary α and $\tilde{a}$. To attack the magnetic spectrum, we cannot rely on a separable ansatz. Fortunately, the techniques of the previous section are flexible enough not to rely on one. In §4.2.2, we describe how to formulate the non-separated equations of motion for both the scalar and vector fields as nonlinear eigenvalue problems. This allows us to accurately and robustly determine the entire quasi-bound state spectrum for a Proca field around a Kerr black hole.

4.2.1 Using Separability

Clearly, the methods used in §4.1.3 also apply to the separated vector equation (2.24), albeit with one small wrinkle. Our discussion there relied on our ability to accurately compute the eigenvalues of the scalar angular equation (2.10), and we skipped past this complication because various software packages already natively compute these quantities.[25] This is not the case for the Proca angular equation (2.22).

Fortunately, (2.22) is also a nonlinear eigenvalue problem which we can solve using the techniques of the previous section. Defining $\zeta = \cos\theta$ and expanding the angular function in the Chebyshev cardinal polynomials,

$$S(\zeta) = \sum_{k=0}^{N} S(\zeta_k)\, p_k(\zeta)\,, \tag{4.20}$$

---

[25]For instance, the eigenvalues of the spheroidal harmonics and their derivatives can be computed to arbitrary precision using Mathematica's `SpheroidalEigenvalue`.

we convert the angular equation (2.22) into another finite-dimensional matrix equation

$$\sum_{k=0}^{N} \mathcal{A}_{nk}(\lambda,\nu)S(\zeta_k) \equiv \mathcal{A}(\lambda,\nu)\,\mathbf{S} = 0\,. \tag{4.21}$$

For a given ν, we can then pass the matrix $\mathcal{A}_{nk}(\lambda,\nu)$ to a solver to find λ as a function of ν. Furthermore, since nonlinear inverse iteration will require the derivative $\partial_\nu \mathcal{M}_{nk}(\nu)$ of the radial matrix, we must also find the derivative of the angular eigenvalues $\lambda'(\nu)$. By differentiating $\det \mathcal{A}_{nk}(\lambda(\nu),\nu) = 0$ with respect to ν, we can rewrite this derivative in terms of derivatives of the matrix $\mathcal{A}$,

$$\lambda'(\nu) = -\frac{\mathrm{tr}\left(\mathcal{A}^{-1}\partial_\nu\mathcal{A}\right)}{\mathrm{tr}\left(\mathcal{A}^{-1}\partial_\lambda\mathcal{A}\right)} = -\frac{\mathbf{S}_{\mathrm{L}}^{\top}(\partial_\nu\mathcal{A})\mathbf{S}_{\mathrm{R}}}{\mathbf{S}_{\mathrm{L}}^{\top}(\partial_\lambda\mathcal{A})\mathbf{S}_{\mathrm{R}}}\,, \tag{4.22}$$

where the second equality follows since the trace is dominated by the zero left and right eigenvectors, $\mathbf{S}_{\mathrm{L}}$ and $\mathbf{S}_{\mathrm{R}}$, when evaluated at the eigenvalue $\lambda(\nu)$. We can thus calculate $\lambda'(\nu)$ for very little additional computational cost. In Fig. 14, we compare our numeric results with their perturbative approximations (B.15).

With the angular eigenvalue in hand, the techniques discussed in §4.1.3 apply almost unchanged. We introduce a map $\zeta(r)$ from $r \in [r_+, \infty)$ to the finite interval $\zeta \in [-1,1]$ and rewrite the radial function as

$$R(r) = \left(\frac{r-r_+}{r-r_-}\right)^{iP_+}(r-r_-)^{\nu-2\alpha^2/\nu}\,e^{-\alpha(r-r_+)/\nu}B(\zeta)\,, \tag{4.23}$$

so that $B(\zeta)$ approaches a constant at the endpoints of the interval $\zeta = \pm 1$. We need not worry about the poles at $r = \hat{r}_\pm$ in (2.24), which will not affect convergence because $R(r) \sim C_\pm + D_\pm(r-\hat{r}_\pm)^2$ is analytic for $r \to \hat{r}_\pm$. Expanding in the Chebyshev cardinal polynomials $p_k(\zeta)$ and sampling the radial equation (2.24) at the Chebyshev nodes, we find a finite-dimensional matrix $\mathcal{M}_{nk}(\nu)$ that can then be passed to a solver to determine the quasi-bound state spectrum.

4.2.2   Without Separability

Having rephrased the problem as a nonlinear eigenvalue problem affords us the flexibility to use a nonseparable ansatz. While this is mainly relevant for the Proca equation, for which a separable ansatz is not known in general, we will first illustrate the technique using the scalar field. It can then be applied to the vector case with minimal complication.

Scalar

In the Schwarzschild limit, $\tilde{a} \to 0$, spherical symmetry is restored in the Kerr geometry. Moreover, since $\tilde{a}$ always appear dressed by factors of α, spherical symmetry is only weakly broken when $\alpha \ll 1$. This mean that, for $\alpha \ll 1$, we can use the weakly broken symmetry to organize our ansatz for the scalar field Φ and decompose Φ into scalar spherical harmonics. The general idea is to first decompose the Klein-Gordon equation into operators that act naturally on the scalar spherical harmonics, and then to use the methods of the previous section to convert it into a finite-dimensional matrix equation.

Our first step is to rewrite the Klein-Gordon equation using the isometries (2.5) and the total angular momentum operator $\mathcal{L}^2$, described in detail in Appendix A. One can show that the operator

$$\left[\Sigma\nabla^2 + \mathcal{L}^2 - \left(\Sigma + \frac{2\alpha r(r^2 + \alpha^2\tilde{a}^2)}{\Delta}\right)\mathcal{L}_t^2 - \frac{\alpha^2\tilde{a}^2}{\Delta}\mathcal{L}_z^2 - \frac{4\alpha^2\tilde{a}r}{\Delta}\mathcal{L}_t\mathcal{L}_z\right]\Phi = \partial_r\left(\Delta\partial_r\Phi\right) \quad (4.24)$$

is purely radial when acting on a scalar field Φ. By assuming that Φ has definite frequency, $\mathcal{L}_t\Phi = -\omega\Phi$, and azimuthal angular momentum, $\mathcal{L}_z\Phi = m\Phi$, the Klein-Gordon equation reduces to

$$\begin{aligned} 0 = {} & \frac{1}{\Delta}\partial_r\left(\Delta\partial_r\Phi\right) - \frac{1}{\Delta}\left(\mathcal{L}^2 + \alpha^2\tilde{a}^2(1-\omega^2)\cos^2\theta\right)\Phi \\ & + \left(-(1-\omega^2) + \frac{P_+^2}{(r-r_+)^2} + \frac{P_-^2}{(r-r_-)^2} + \frac{A_-}{(r_+-r_-)(r-r_-)} - \frac{A_+}{(r_+-r_-)(r-r_+)}\right)\Phi \end{aligned} \qquad (4.25)$$

with minimal effort. We recognize the spheroidal harmonic equation (2.10)

$$\left(\mathcal{L}^2 + \alpha^2\tilde{a}^2(1-\omega^2)\cos^2\theta\right)S = \Lambda S\,, \qquad (4.26)$$

and so (4.25) is of the same form as (2.12), yet without needing the separable ansatz (2.9). Mimicking (4.9), we then strip Φ of its asymptotic behavior and decompose it into scalar spherical harmonics,

$$\Phi = e^{-i\omega t}\left(\frac{r-r_+}{r-r_-}\right)^{iP_+}(r-r_-)^{-1+\nu-2\alpha^2/\nu}e^{-\alpha(r-r_+)/\nu}\sum_\ell B_\ell(\zeta)\,Y_{\ell m}(\theta,\phi)\,, \qquad (4.27)$$

where the sum ranges over even or odd values of ℓ for parity even or odd modes, respectively.

With this ansatz, we can project the Klein-Gordon equation (4.25) onto the scalar spherical harmonics to find

$$\left(\frac{\partial^2}{\partial\zeta^2} + \mathcal{C}_1(\nu,\zeta)\frac{\partial}{\partial\zeta} + \mathcal{C}_2(\nu,\zeta)\right)B_\ell(\zeta) + \mathcal{C}_{\ell,\ell+2}(\nu,\zeta)\,B_{\ell+2}(\zeta) + \mathcal{C}_{\ell,\ell-2}(\nu,\zeta)B_{\ell-2}(\zeta) = 0\,, \quad (4.28)$$

where the functions $\mathcal{C}_i$ again depend on our choice of $\zeta(r)$, but now have explicit ℓ dependence. Importantly, the $\cos^2\theta$ term in (4.25) breaks spherical symmetry and thus couples different spherical harmonics to one another, through the function $\mathcal{C}_{\ell,\ell'}$. By expanding the radial functions $B_\ell(\zeta)$ in cardinal polynomials, as in (4.14), and sampling at the interpolation points (4.13), this system of equations can be rewritten as the matrix,

$$\begin{aligned} \mathcal{M}_{n\ell;k\ell'}(\nu) = {} & \left(p_k''(\zeta_n) + \mathcal{C}_1(\nu,\zeta_n)p_k'(\zeta_n) + \mathcal{C}_2(\nu,\zeta_n)\delta_{nk}\right)\delta_{\ell\ell'} \\ & + \mathcal{C}_{\ell,\ell+2}(\nu,\zeta_n)\delta_{nk} + \mathcal{C}_{\ell,\ell-2}(\nu,\zeta_n)\delta_{nk}\,, \end{aligned} \qquad (4.29)$$

which can then be passed to a solver to find the bound state spectrum.

To fit (4.29) on a computer, it is necessary both to sample a finite number of radial points and to include only a finite number of angular modes. This angular truncation is an additional

source of error that must be controlled. Fortunately, both the Klein-Gordon and Proca equations enjoy an approximate spherical symmetry that is restored in the Schwarzschild limit—this is why we expanded (4.27) in terms of scalar spherical harmonics, as opposed to another complete set of functions. In this basis, the $\mathcal{C}_{\ell,\ell\pm2}$ mixings in (4.29) are proportional to $\alpha^2\tilde{a}^2$. For the main superradiant state $|211\rangle$, the angular truncation error roughly scales as $(\alpha\tilde{a})^{2L}$ if we include only $\ell = 1, 3, \ldots, 2L + 1$ in the expansion (4.27). However, we must emphasize that this estimate of the truncation error is only accurate at small α or $\tilde{a}$. Of course, the scalar (or vector) spherical harmonics are a complete set and so may represent an arbitrary scalar (or vector) field configuration. As long as we include 'enough' of these angular modes, we are guaranteed to faithfully represent any field configuration. In fact, one can show from their recurrence relation [54] that the coefficients of the spherical harmonic decomposition of the spheroidal harmonics decay faster than exponentially, independent of $\alpha\tilde{a}$. This reflects the intuition that low-energy solutions to the Klein-Gordon equation are relatively smooth, and the same will be true for the Proca field. In practice, this method is as fast[26] as that using the separable ansatz in §4.1.3 and can be made just as accurate. Applying this algorithm reproduces the results presented in §2.4.

Vector

A similar strategy works for the Proca equation, although we will encounter additional technical challenges. As for the case of the scalar, we will first rewrite the equations of motion using operators that act simply on either the radial or angular directions. We will then decompose the temporal and spatial components of the vector field into scalar and vector spherical harmonics, and use this decomposition to convert the equations of motion into a matrix equation. In the following, we provide a mostly qualitative overview of our techniques, keeping the many technical details confined to Appendix C.

One complication, compared with the scalar case, is that the Proca equation (2.2) needs to be supplemented by the Lorenz condition, $\nabla^\mu A_\mu = 0$. We can do this either by first solving $\nabla^\mu A_\mu = 0$ for the temporal component A_t and then substituting it into the Proca equation to find an equation purely in terms of the spatial components A_i, or by including the Lorenz constraint as an additional 'block' of the matrix equation. We will choose the latter, since it is more flexible and generally easier to implement.

With this in mind, our first step is to rewrite both the Proca equation and Lorenz constraint using operators that act simply in either the radial or angular directions. The operator (4.24) we used in the previous section is, unfortunately, only radial when acting on a scalar. It will thus be extremely convenient to expand the vector field along a carefully chosen tetrad[27] $A_\mu = A_a f^a{}_\mu$, so that we may instead work with the four scalar fields A_a instead of the four-vector A_μ. As detailed in Appendix C, we require that this tetrad is stationary, $\mathcal{L}_t f^a{}_\mu = 0$. We will take $f^0{}_\mu \mathrm{d}x^\mu \propto \mathrm{d}t$ to be purely temporal with no angular dependence and the $f^i{}_\mu$ to have definite total and azimuthal angular momentum—their explicit form is given in (C.3).

---

[26]Though the matrix (4.29) passed to the nonlinear eigenvalue solver is generally much larger than (4.16), this is generally balanced by no longer needing to compute the spheroidal harmonic eigenvalue and (more importantly) its derivative with respect to ν.

[27]We will use tetrad indices $a, b, \ldots$ to run from 0 to 3, and indices $i, j, \ldots$ to run from 1 to 3. By convention, repeated indices are summed over.

We may then use this decomposition with (4.24) to rewrite the Proca equation as

$$
0 = \left(\frac{1}{\Delta} \partial_r (\Delta \partial_r) - \frac{1}{\Delta} \left(\pounds^2 + \alpha^2 \tilde{a}^2 \left(1 - \omega^2 \right) \cos^2 \theta \right) \right) A_b \tag{4.30}
$$

$$
+ \left(-(1 - \omega^2) + \frac{P_+^2}{(r - r_+)^2} + \frac{P_-^2}{(r - r_-)^2} - \frac{A_+}{(r - r_+)(r_+ - r_-)} + \frac{A_-}{(r - r_-)(r_+ - r_-)} \right) A_b
$$

$$
+ \mathcal{S}_b{}^a A_a + \mathcal{Q}_b{}^a \pounds_z A_a + \mathcal{R}_b{}^a \partial_r A_a + \mathcal{P}_b{}^a \mathcal{D}_+ A_a + \mathcal{Z}_b{}^a \mathcal{D}_0 A_a + \mathcal{M}_b{}^a \mathcal{D}_- A_a \,,
$$

where we have assumed that the vector field has definite frequency $\pounds_t A_\mu = -\omega A_\mu$ and azimuthal angular momentum $\pounds_z A_\mu = m A_\mu$. We recognize that (4.30) is simply four copies of the scalar equation (4.25), coupled together through the mixing matrices $\mathcal{S}$, $\mathcal{Q}$, $\mathcal{R}$, $\mathcal{P}$, $\mathcal{Z}$ and $\mathcal{M}$, whose precise form can be found in (C.9) and depend on our choice of tetrad. These mixing matrices encode the 'vector-ness' of the scalars A_a, while $\mathcal{D}_\pm$ and $\mathcal{D}_0$—cf. (A.21) and (A.22)—are purely angular operators that act simply on the scalar spherical harmonics. The Lorenz constraint can be similarly decomposed,

$$
0 = \mathcal{T}^0 A_0 + \mathcal{S}^i A_i + \mathcal{R}^i \, \partial_r A_i + \mathcal{P}^i \, \mathcal{D}_+ A_i + \mathcal{Z}^i \, \mathcal{D}_0 A_i + \mathcal{M}^i \, \mathcal{D}_- A_i \,, \tag{4.31}
$$

in terms of the mixing vectors defined in (C.11).

As we explain in §C.2, we also choose the $f^a{}_\mu$ so that the scalars A_a have the same asymptotic behavior, (3.4) and (3.6), as the scalar field Φ. Then, by mimicking the scalar decomposition (4.27), we strip the A_a of their asymptotic behavior and decompose the temporal component A_0 into scalar spherical harmonics and the spatial components A_i into one-form harmonics

$$
A_0 = e^{-i\omega t} \left(\frac{r - r_+}{r - r_-} \right)^{iP_+} (r - r_-)^{-1+\nu-2\alpha^2/\nu} e^{-\alpha(r-r_+)/\nu} \sum_j B_{0,j}(\zeta) \, Y_{jm}(\theta, \phi) \,, \tag{4.32}
$$

$$
A_i = e^{-i\omega t} \left(\frac{r - r_+}{r - r_-} \right)^{iP_+} (r - r_-)^{-1+\nu-2\alpha^2/\nu} e^{-\alpha(r-r_+)/\nu} \sum_{\ell,j} B_{\ell j}(\zeta) \, Y_i^{\ell,jm}(\theta, \phi) \,. \tag{4.33}
$$

In the scalar case, we found that only components with even (odd) parity could couple to one another. This is a reflection of the fact that the Kerr metric is invariant under parity transformations, and so only scalar harmonics with the same parity couple to one another. This also applies to the Proca field. As discussed in Appendix A, the parity of the scalar and vector spherical harmonics in (4.32) and (4.33) are $(-1)^j$ and $(-1)^{\ell+1}$, respectively. When we solve for the spectrum of a parity even or odd mode, we can restrict the expansions (4.32) and (4.33), halving the number of angular terms we must include to faithfully represent the Proca field.

$$
\begin{pmatrix}
\boxed{\mathcal{D}^{\text{ss}}_{01\,|\,01}} & \mathcal{D}^{\text{ss}}_{01\,|\,21} & \mathcal{D}^{\text{ss}}_{01\,|\,22} & \cdots & \mathcal{D}^{\text{st}}_{01\,|\,0} & \mathcal{D}^{\text{st}}_{01\,|\,2} & \cdots \\
\mathcal{D}^{\text{ss}}_{21\,|\,01} & \mathcal{D}^{\text{ss}}_{21\,|\,21} & \mathcal{D}^{\text{ss}}_{21\,|\,22} & \cdots & \mathcal{D}^{\text{st}}_{21\,|\,0} & \mathcal{D}^{\text{st}}_{21\,|\,2} & \cdots \\
\mathcal{D}^{\text{ss}}_{22\,|\,01} & \mathcal{D}^{\text{ss}}_{22\,|\,21} & \mathcal{D}^{\text{ss}}_{22\,|\,22} & \cdots & \mathcal{D}^{\text{st}}_{22\,|\,0} & \mathcal{D}^{\text{st}}_{22\,|\,2} & \cdots \\
\vdots & \vdots & \vdots & \ddots & \vdots & \vdots & \cdots \\
\mathcal{D}^{\text{ts}}_{0\,|\,01} & \mathcal{D}^{\text{ts}}_{0\,|\,21} & \mathcal{D}^{\text{ts}}_{0\,|\,22} & \cdots & \mathcal{D}^{\text{tt}}_{0\,|\,0} & \mathcal{D}^{\text{tt}}_{0\,|\,2} & \cdots \\
\mathcal{D}^{\text{ts}}_{2\,|\,01} & \mathcal{D}^{\text{ts}}_{2\,|\,21} & \mathcal{D}^{\text{ts}}_{2\,|\,22} & \cdots & \mathcal{D}^{\text{tt}}_{2\,|\,0} & \mathcal{D}^{\text{tt}}_{2\,|\,2} & \cdots \\
\vdots & \vdots & \vdots & \ddots & \vdots & \vdots & \cdots
\end{pmatrix}
\begin{pmatrix}
B_{0,1m} \\
\boxed{B_{2,1m}} \\
B_{2,2m} \\
\vdots \\
B_{0m} \\
B_{2m} \\
\vdots
\end{pmatrix}
= 0
$$

where the boxed block $\mathcal{D}^{\text{ss}}_{01\,|\,01}$ expands to

$$
\begin{pmatrix}
\mathcal{D}^{\text{ss}}_{01\,|\,01}[p_0(\zeta_0)] & \cdots & \mathcal{D}^{\text{ss}}_{01\,|\,01}[p_N(\zeta_0)] \\
\mathcal{D}^{\text{ss}}_{01\,|\,01}[p_0(\zeta_1)] & \cdots & \mathcal{D}^{\text{ss}}_{01\,|\,01}[p_N(\zeta_1)] \\
\vdots & \ddots & \vdots \\
\mathcal{D}^{\text{ss}}_{01\,|\,01}[p_0(\zeta_N)] & \cdots & \mathcal{D}^{\text{ss}}_{01\,|\,01}[p_N(\zeta_N)]
\end{pmatrix}
$$

and the boxed vector entry $B_{2,1m}$ expands to

$$
\begin{pmatrix}
B_{2,1m}(\zeta_0) \\
B_{2,1m}(\zeta_1) \\
B_{2,1m}(\zeta_2) \\
\vdots \\
B_{2,1m}(\zeta_N)
\end{pmatrix}
$$

Figure 15: Structure of the matrix equation for the parity even modes. Each angular block forms a separate radial sector, which is sampled at $N+1$ points $\{\zeta_k\}$.

Following the scalar case, we project both (4.30) and (4.31) onto the different scalar and vector harmonics to find the following system of equations,

$$
\sum_{\ell',j'} \mathcal{D}^{\text{ss}}_{\ell j\,|\,\ell'j'}[B_{\ell',j'm}(\zeta)] + \sum_{j'} \mathcal{D}^{\text{st}}_{\ell j\,|\,j'}[B_{j'm}(\zeta)] = 0 \,, \tag{4.34}
$$

$$
\sum_{\ell',j'} \mathcal{D}^{\text{ts}}_{j\,|\,\ell'j'}[B_{\ell',j'm}(\zeta)] + \sum_{j'} \mathcal{D}^{\text{tt}}_{j\,|\,j'}[B_{j'm}(\zeta)] = 0 \,, \tag{4.35}
$$

which can be written as the matrix equation schematically depicted in Fig. 15, where we have introduced a collection of operators defined in (C.32). This system of equations is the vector analog of (4.28), though it appears more complicated because we have explicitly separated the spatial and temporal components. As before, this matrix may then be passed to a nonlinear eigenvalue solver to determine the quasi-bound state spectrum. This method reproduces the quasi-bound state frequencies of the electric modes computed using the separable ansatz in §4.2.1. More importantly, it accurately computes the energy spectrum of the magnetic modes $|211m\rangle$, shown in Figures 7 and 11, and provides a crucial check of the magnetic instability rate (2.35), displayed in Figures 9 and 10.

5 Summary and Outlook

In this work, we have computed the quasi-bound state spectra of massive scalar and vector fields around rotating black holes, both analytically and numerically. The main challenge has been the fact that the fields vary rapidly in the near-horizon region of the black hole, which causes ordinary perturbative approximations to fail and many numerical methods to become unreliable. To address this issue in our analytical treatment, we constructed independent solutions in different asymptotic regions of the black hole spacetime and determined the spectrum by demanding that these solutions match in their regions of shared validity. For the scalar field, the asymptotic expansions in the near and far regions were matched directly, while, for the vector field, these expansions could only be matched indirectly, via a solution in an additional intermediate region. This reflected the fact that the vector field in the near and far regions depend on different types of angular momentum, which a matched solution must smoothly interpolate between. We presented results for the energies and instabilities as perturbative expansions in powers of the gravitational fine structure constant α.

Our perturbative analysis relied on the separability of the equations of motion, and thus did not apply to all magnetic modes of the vector field. However, by working at linear order in the black hole spin $\tilde{a}$, we derived perturbative results for the energy spectrum of the magnetic modes, which we argued plausibly extend to arbitrary $\tilde{a}$. Furthermore, we provided an educated guess for the magnetic instability rate by demanding that it takes the same functional form as the electric instability rates, and fixing its undetermined overall coefficient and dominant α-scaling using its known Schwarzschild limit.

As a check of our conjectural magnetic results, and to study all modes at large values of α, we computed the spectra numerically. The rapid variation of the fields in the near-horizon region presents serious numerical obstacles which can potentially destroy the accuracy of a solution. We described how to avoid these pitfalls and presented a formulation of the problem that accurately computes the quasi-bound state frequencies without relying on a separable ansatz. In principle, this formulation can be extended to ultralight fields of arbitrary spin about any stationary spacetime, although it works best if spherical symmetry is approximately restored at large distances. These numeric results provided a valuable check of our analytic approximations, which we found to accurately predict the energy eigenvalues and instability rates for both electric and magnetic modes as long as $\alpha \lesssim 0.2$, even at large $\tilde{a}$.

As shown in Figures 3 and 5, the scalar and vector gravitational atoms have qualitatively distinct spectra. In particular, the vector field's intrinsic spin allows for many more nearly degenerate states than the scalar. This suggests that we could differentiate between the scalar and vector atoms by studying induced transitions between these different energy levels. In fact, such transitions naturally occur when the gravitational atom is part of a binary system, in which case the gravitational interaction with the binary companion leads to mixings of the energy levels [13]. The results of this paper therefore provide an essential input for the phenomenology of such systems and, in a forthcoming work [29], we study how these spectral differences manifest themselves in gravitational wave signals.

Acknowledgements

A Tensor Spherical Harmonics

In this appendix, we describe the spherical harmonic decomposition of tensor fields in black hole backgrounds, focusing in particular on the construction of vector spherical harmonics.

A.1 Tensor Representations of SO(3)

Besides the time-like Killing vector $k_t = -i\partial_t$, the spherically symmetric Schwarzschild black hole enjoys three additional Killing vectors, which in Boyer-Lindquist coordinates take the form

$$
\begin{aligned}
k_x &= -i\left(y\frac{\partial}{\partial z} - z\frac{\partial}{\partial y}\right) = i\left(\sin\phi\,\frac{\partial}{\partial\theta} + \cot\theta\cos\phi\,\frac{\partial}{\partial\phi}\right), \\
k_y &= -i\left(z\frac{\partial}{\partial x} - x\frac{\partial}{\partial z}\right) = i\left(-\cos\phi\,\frac{\partial}{\partial\theta} + \cot\theta\sin\phi\,\frac{\partial}{\partial\phi}\right), \\
k_z &= -i\left(x\frac{\partial}{\partial y} - y\frac{\partial}{\partial x}\right) = -i\frac{\partial}{\partial\phi}\,.
\end{aligned}
\tag{A.1}
$$

These Killing vectors are the generators of the group SO(3) and therefore satisfy the commutation relations

$$
[k_i, k_j] = \mathcal{L}_i k_j = i\epsilon_{ijk}k_k\,,
\tag{A.2}
$$

where we use $i, j, k = 1, 2, 3$ to represent x, y, z, respectively, and have employed the shorthand $\mathcal{L}_i = \mathcal{L}_{k_i}$ for the Lie derivative along k_i. This algebra has a quadratic Casimir,

$$
\mathcal{L}^2 = \mathcal{L}_x^2 + \mathcal{L}_y^2 + \mathcal{L}_z^2\,,
\tag{A.3}
$$

that commutes with the generators k_i. Irreducible representations of this group can then be labeled by their eigenvalues under $\mathcal{L}^2$ and one of the generators $\mathcal{L}_i$. It is conventional to define the representation $|j, m\rangle$ by

$$
\begin{aligned}
\mathcal{L}^2|j, m\rangle &= j(j+1)|j, m\rangle\,, \\
\mathcal{L}_z|j, m\rangle &= m|j, m\rangle\,.
\end{aligned}
\tag{A.4}
$$

For now, $|j, m\rangle$ denotes an arbitrary (tensor) representation of this algebra with total angular momentum j and total azimuthal angular momentum m.

We may also define the vector fields

$$
k_\pm = k_x \pm ik_y = e^{\pm i\phi}\left(\pm\frac{\partial}{\partial\theta} + i\cot\theta\frac{\partial}{\partial\phi}\right),
\tag{A.5}
$$

and the corresponding operators $\mathcal{L}_\pm = \mathcal{L}_{k_\pm}$. These operators raise/lower the azimuthal angular momentum

$$
\begin{aligned}
\mathcal{L}_\pm k_\mp &= [k_\pm, k_\mp] = \pm 2k_z\,, \\
\mathcal{L}_z k_\pm &= [k_z, k_\pm] = \pm k_\pm\,.
\end{aligned}
\tag{A.6}
$$

A physical, finite-dimensional representation requires that

$$
\mathcal{L}_\pm|j, \pm j\rangle = 0\,,
\tag{A.7}
$$

since we could otherwise violate the requirement that $\mathcal{L}^2 - \mathcal{L}_z^2 \geq 0$. With the normalization condition $\langle j, \pm j | j, \pm j \rangle = 1$, (A.7) defines the states $|j, \pm j\rangle$. The other states are then defined in the *Condon-Shortley phase convention*[28] by

$$\begin{aligned}
\mathcal{L}_+|j, m\rangle &= \sqrt{(j-m)(j+m+1)}\,|j, m+1\rangle\,, \\
\mathcal{L}_-|j, m\rangle &= \sqrt{(j+m)(j-m+1)}\,|j, m-1\rangle\,.
\end{aligned} \tag{A.8}$$

Two representations of SO(3) can be combined into a single representation with definite total and azimuthal angular momentum using the Clebsch-Gordan coefficients,

$$|j, m; \ell, s\rangle = \sum_{m_\ell=-\ell}^{\ell} \sum_{m_s=-s}^{s} |(s\,m_s)\,(\ell\,m_\ell)\rangle\langle(s\,m_s)\,(\ell\,m_\ell)|j, m; \ell, s\rangle\,. \tag{A.9}$$

This yields a well-defined prescription for generating tensor spherical harmonics of any rank. That is, given a tensor with an arbitrary number of spatial indices, we can define the basis of tensors $|s, m_s\rangle$ by first solving

$$\begin{aligned}
\mathcal{L}_+ \chi_{ijk\ldots}^{s,s} &= 0\,, \\
\mathcal{L}_z \chi_{ijk\ldots}^{s,s} &= s\,\chi_{ijk\ldots}^{s,s}\,,
\end{aligned} \tag{A.10}$$

and then using $\mathcal{L}_-$, with the normalization convention above, to define the other $|s, m_s\rangle$. Note that these conditions immediately imply that $\mathcal{L}^2 \chi_{ijk\ldots}^{s,s} = s(s+1)\chi_{ijk\ldots}^{s,s}$. We may then combine $|s, m_s\rangle$ with a *scalar* representation of $|\ell, m_\ell\rangle$, i.e. the scalar spherical harmonics $Y_{\ell m_\ell}(\theta, \phi)$, to generate the tensor spherical harmonics

$$T_{ijk\ldots}^{j,m;\ell,s}(\theta, \phi) = \sum_{m_\ell=-\ell}^{\ell} \sum_{m_s=-s}^{s} \langle(s\,m_s)\,(\ell\,m_\ell)|j, m; \ell, s\rangle\,Y_{\ell m_\ell}(\theta, \phi)\,\chi_{ijk\ldots}^{s,m_s}\,. \tag{A.11}$$

This procedure yields a tensor representation of SO(3). Because our ultimate goal is to expand vector fields in $\mathbb{R}^3$, the $T_{ijk\ldots}^{j,m;\ell,s}$ must actually form a representation of O(3), i.e. the group SO(3) together with inversions. Since the scalar spherical harmonics have definite parity $Y_{\ell m_\ell}(\pi - \theta, \phi + \pi) = (-1)^\ell Y_{\ell m_\ell}(\theta, \phi)$, we can choose $\chi_{ijk\ldots}^{s,m_s}$ to also have definite parity, so that (A.11) defines a tensor representation of O(3). Below, we will explicitly construct a family of vector spherical harmonics. In that case, the choice of parity determines whether (A.11) yields *vector* or *pseudo-vector* spherical harmonics.

A.2 Vector Spherical Harmonics

To form a basis of vector spherical harmonics, we first construct the basis of vectors χ_{1,m_s}^i by the defining relations

$$\begin{aligned}
\mathcal{L}_+\chi_{1,1}^i &= 0\,, \\
\mathcal{L}_z\chi_{1,1}^i &= \chi_{1,1}^i\,.
\end{aligned} \tag{A.12}$$

---

[28]Which convention should be used depends on the convention for the Clebsch-Gordan coefficients. We use this convention since it is the one used by Mathematica.

These equations have the general solution

$$\chi^i_{1,1}\,\partial_i = \frac{e^{i\phi}}{\sqrt{2}}\left[F_r(r)\sin\theta\,\partial_r + F_\phi(r)(\partial_\theta + i\cot\theta\,\partial_\phi) + F_\theta(r)(\cos\theta\,\partial_\theta + i\csc\theta\,\partial_\phi)\right],\qquad\text{(A.13)}$$

where the F_i are, in general, undetermined functions of r. Imposing that $\chi^i_{1,1}$ transforms like a *vector* under inversions, leads to $F_\phi = 0$. Taking, instead, $F_r = F_\theta = 0$ would yield a basis of *pseudo-vector* spherical harmonics. We may then define $\sqrt{2}\chi^i_{1,0} = \mathcal{L}_-\chi^i_{1,1}$ and $\sqrt{2}\chi^i_{1,-1} = \mathcal{L}_-\chi^i_{1,0}$, to find the complete basis

$$\chi^i_{1,1}\,\partial_i = \frac{e^{i\phi}}{\sqrt{2}}\left[F_r(r)\sin\theta\,\partial_r + F_\theta(r)(\cos\theta\,\partial_\theta + i\csc\theta\,\partial_\phi)\right],$$
$$\chi^i_{1,0}\,\partial_i = -F_r(r)\cos\theta\,\partial_r + F_\theta(r)\sin\theta\,\partial_\theta\,,\qquad\text{(A.14)}$$
$$\chi^i_{1,-1}\,\partial_i = \frac{e^{-i\phi}}{\sqrt{2}}\left[-F_r(r)\sin\theta\,\partial_r + F_\theta(r)(-\cos\theta\,\partial_\theta + i\csc\theta\,\partial_\phi)\right].$$

In flat space, we can take $F_r = -1$ and $F_\theta = -1/r$, so that these basis vectors are covariantly constant, $\nabla_\mu\chi^\nu_{1,m_s} = 0$.[29] These harmonics then reduce to those commonly used in the literature; see e.g. [41]. This is impossible in the Kerr geometry. It will instead be more convenient to choose F_r and F_θ to simplify the boundary conditions of the vector field at the horizon and at spatial infinity, as discussed in §C.2. For each choice of $F_r(r)$ and $F_\theta(r)$, we then have a set of *vector spherical harmonics*

$$Y^i_{\ell,jm} = \sum_{m_s=-1}^{1} \langle(1\,m_s)\,(\ell\,m-m_s)|j,m\rangle\,Y_{\ell,m-m_s}(\theta,\phi)\,\chi^i_{1,m_s}\,,\qquad\text{(A.15)}$$

which have definite angular momentum,

$$\mathcal{L}^2 Y^i_{\ell,jm} = j(j+1)Y^i_{\ell,jm}\,,$$
$$\mathcal{L}_z Y^i_{\ell,jm} = mY^i_{\ell,jm}\,,\qquad\text{(A.16)}$$

and by construction satisfy

$$\mathcal{L}^2\left(e^{-i\omega t}G(r)Y^i_{\ell,jm}\right) = j(j+1)e^{-i\omega t}G(r)Y^i_{\ell,jm}\,,$$
$$\mathcal{L}_z\left(e^{-i\omega t}G(r)Y^i_{\ell,jm}\right) = me^{-i\omega t}G(r)Y^i_{\ell,jm}\,.\qquad\text{(A.17)}$$

The Clebsch-Gordan coefficients are only non-vanishing for $j \geq 0$, $|m| \leq j$, and $j+1 \geq \ell \geq |j-1|$. Any smooth spatial vector field can be decomposed into these harmonics,

$$V^i(t,r,\theta,\phi) = \sum_{j=0}^{\infty}\sum_{\ell=|j-1|}^{j+1}\sum_{m=-j}^{j} V_{\ell,jm}(t,r)\,Y^i_{\ell,jm}(\theta,\phi)\,.\qquad\text{(A.18)}$$

---

[29]If we can find basis vectors that are covariantly constant, then it is possible to unambiguously disentangle spin and orbital angular momentum, so that ℓ can be a good quantum number.

By construction, the harmonics (A.15) have definite parity, and acquire a factor of $(-1)^{\ell+1}$ under the transformation $(\theta, \phi) \to (\pi - \theta, \phi + \pi)$. A general odd-parity vector field E^i can thus be expanded as

$$E^i = \sum_{j,\ell,m} E_{\ell,jm}(t,r) Y^i_{\ell,jm}(\theta, \phi) \,, \tag{A.19}$$

where j runs over all positive integers, ℓ is even and takes values between $j \pm 1$, and m runs from $-j$ to j. Similarly, a general even-parity vector field B^i can be expanded as

$$B^i = \sum_{j,\ell,m} B_{\ell,jm}(t,r) \, Y^i_{\ell,jm}(\theta, \phi) \,, \tag{A.20}$$

where j runs over all non-negative integers, ℓ runs over all odd numbers between $j \pm 1$, and m runs from $-j$ to j. In both cases, if the field has definite azimuthal angular momentum m_z, the sum over m is restricted to m_z and hence can be dropped.

A major benefit of this basis of vector fields (A.14) is that it also acts simply on the scalar spherical harmonics. We may define the operators

$$\mathcal{D}_\pm Y_{\ell m_\ell} = \frac{e^{\pm i\phi}}{\sqrt{2}} \left(\pm \cos\theta \, \partial_\theta + i \csc\theta \, \partial_\phi \right) Y_{\ell m_\ell}(\theta, \phi) \tag{A.21}$$

$$= \sqrt{\frac{(\ell+1)^2(\ell \mp m_\ell)(\ell \mp m_\ell - 1)}{2(2\ell+1)(2\ell-1)}} Y_{\ell-1,m_\ell \pm 1} + \sqrt{\frac{\ell^2(\ell \pm m_\ell + 1)(\ell \pm m_\ell + 2)}{2(2\ell+3)(2\ell+1)}} Y_{\ell+1,m_\ell \pm 1} \,,$$

$$\mathcal{D}_0 Y_{\ell m_\ell} = \sin\theta \, \partial_\theta Y_{\ell m_\ell}(\theta, \phi) \tag{A.22}$$

$$= \sqrt{\frac{\ell^2(\ell + m_\ell + 1)(\ell - m_\ell + 1)}{(2\ell+1)(2\ell+3)}} Y_{\ell+1,m_\ell} - \sqrt{\frac{(\ell+1)^2(\ell + m_\ell)(\ell - m_\ell)}{(2\ell+1)(2\ell-1)}} Y_{\ell-1,m_\ell} \,,$$

so that the angular legs of each of (A.14) can be rewritten using these operators,

$$\begin{aligned}
\chi^i_{1,1} \, \partial_i &= \frac{1}{\sqrt{2}} e^{i\phi} \sin\theta F_r \, \partial_r + F_\theta \, \mathcal{D}_+ \,, \\
\chi^i_{1,0} \, \partial_i &= -F_r \cos\theta \, \partial_r + F_\theta \, \mathcal{D}_0 \,, \\
\chi^i_{1,-1} \, \partial_i &= -\frac{1}{\sqrt{2}} e^{-i\phi} F_r \sin\theta \, \partial_r + F_\theta \, \mathcal{D}_- \,.
\end{aligned} \tag{A.23}$$

While not strictly necessary, it will prove extremely convenient in our decomposition of the Proca equation to write all angular derivatives in terms of $\mathcal{L}^2$, $\mathcal{L}_z$, $\mathcal{D}_\pm$, and $\mathcal{D}_0$, as derivatives like $\partial_\theta Y_{\ell,m}$ are not easily expressible in terms of other spherical harmonics.

Finally, it will also be useful to construct a basis of one-form harmonics $\chi^{1,m_s}_i \, \mathrm{d}x^i$, which are dual to the vector fields (A.14), in the sense that

$$\bar{\chi}^{1,m_s}_i \chi^i_{1,m'_s} = \delta^{m_s}_{m'_s} \quad \text{and} \quad \bar{\chi}^{1m_s}_i \chi^j_{1,m_s} = \delta^j_i \,, \tag{A.24}$$

where the bar denotes complex conjugation. Explicitly, these form fields are

$$\chi_i^{1,1}\,\mathrm{d}x^i = \frac{1}{\sqrt{2}}e^{i\phi}\left(F_r^{-1}\,\sin\theta\,\mathrm{d}r + F_\theta^{-1}\left(\cos\theta\,\mathrm{d}\theta + i\sin\theta\,\mathrm{d}\phi\right)\right),$$

$$\chi_i^{1,0}\,\mathrm{d}x^i = -F_r^{-1}\cos\theta\,\mathrm{d}r + F_\theta^{-1}\cos\theta\,\mathrm{d}\theta\,, \qquad\qquad (\mathrm{A.25})$$

$$\chi_i^{1,-1}\,\mathrm{d}x^i = \frac{1}{\sqrt{2}}e^{-i\phi}\left(-F_r^{-1}\sin\theta\,\mathrm{d}r + F_\theta^{-1}\left(-\cos\theta\,\mathrm{d}\theta + i\sin\theta\,\mathrm{d}\phi\right)\right).$$

We can then write the set of *one-form spherical harmonics* as

$$Y_i^{\ell,jm} = \sum_{m_s=-1}^{1}\langle(1\,m_s)\,(\ell\,m-m_s)|j,m\rangle\,Y_{\ell,m-m_s}(\theta,\phi)\,\chi_i^{1,m_s}\,, \qquad (\mathrm{A.26})$$

which satisfy the orthonormality condition,

$$\int_{\mathrm{S}^2}\mathrm{d}\Omega\,\bar{Y}_i^{\ell,jm}(\theta,\phi)\,Y_{\ell',j'm'}^i(\theta,\phi) = \delta_{j'}^j\delta_{\ell'}^\ell\delta_{m'}^m\,, \qquad (\mathrm{A.27})$$

where $\int_{\mathrm{S}^2}\mathrm{d}\Omega = \int_0^{2\pi}\mathrm{d}\phi\int_0^\pi\sin\theta\,\mathrm{d}\theta$ denotes integration over the sphere.

B Details of the Analytical Treatment

In Section 3, we derived the quasi-bound state spectra for massive scalar and vector fields on the Kerr geometry, using the method of match asymptotic expansion. In this appendix, we provide some of the technical details that we left out in Section 3.

B.1 Separable Ansatz for Vectors

In the coordinates (2.3), the polarization tensor $B^{\mu\nu}$ in (2.20) reads

$$
B^{\mu\nu} = \frac{1}{\Sigma q_r}
\begin{pmatrix}
0 & iq_a\lambda^{-1}r & 0 & 0 \\
-iq_a\lambda^{-1}r & \Delta & 0 & -i\alpha\tilde{a}\lambda^{-1}r \\
0 & 0 & 0 & 0 \\
0 & i\alpha\tilde{a}\lambda^{-1}r & 0 & -\alpha^2\tilde{a}^2\Delta^{-1}
\end{pmatrix}
+ \frac{q_a}{\Delta q_r q_\theta}
\begin{pmatrix}
-1+\alpha^2\tilde{a}^2\lambda^{-2} & 0 & 0 & \alpha\tilde{a}\lambda^{-2} \\
0 & 0 & 0 & 0 \\
0 & 0 & 0 & 0 \\
\alpha\tilde{a}\lambda^{-2} & 0 & 0 & 0
\end{pmatrix}
$$

$$
+ \frac{1}{\Sigma q_\theta}
\begin{pmatrix}
-2\alpha^3\tilde{a}^2\Delta^{-1}r\sin^2\theta & 0 & i\alpha^2\tilde{a}^2\lambda^{-1}\cos\theta\sin\theta & -2\alpha^2\tilde{a}\Delta^{-1}r \\
0 & 0 & 0 & 0 \\
-i\alpha^2\tilde{a}^2\lambda^{-1}\cos\theta\sin\theta & 0 & 1 & -i\alpha\tilde{a}\lambda^{-1}\cot\theta \\
-2\alpha^2\tilde{a}\Delta^{-1}r & 0 & i\alpha\tilde{a}\lambda^{-1}\cot\theta & \csc^2\theta
\end{pmatrix} ,
$$

$$\tag{B.1}$$

where the following quantities have been introduced

$$
\begin{aligned}
q_r &\equiv 1 + \lambda^{-2}r^2 \,, \\
q_\theta &\equiv 1 - \alpha^2\tilde{a}^2\lambda^{-2}\cos^2\theta \,, \\
q_a &\equiv r^2 + \alpha^2\tilde{a}^2 \,.
\end{aligned}
\tag{B.2}
$$

Expanding $B^{\mu\nu}$ to leading order in α, which is equivalent to taking the flat-space limit, leads to the result (3.31).

In [28], the following special limit was taken[30]

$$
\lim_{\alpha\to 0}\left(\alpha\tilde{a}\lambda^{-1}\right) = \chi \,,
\tag{B.3}
$$

with $\chi = m \pm 1$, and the separation constant λ formally vanishes. It was then found that the ansatz (2.20) in this limit captures a subset of the magnetic-type modes of the vector field. We will now investigate these special solutions in more detail. The vector field in this case becomes

$$
A^{\mu}_{(0)} = \frac{1}{r^2\left(1 - \chi^2\cos^2\theta\right)}
\begin{pmatrix}
0 & 0 & 0 & 0 \\
0 & 0 & 0 & 0 \\
0 & 0 & 1 & -i\chi\cot\theta \\
0 & 0 & i\chi\cot\theta & \csc^2\theta
\end{pmatrix}
\begin{pmatrix}
\partial_t \\
\partial_r \\
\partial_\theta \\
\partial_\phi
\end{pmatrix}
Z_0 \,,
\tag{B.4}
$$

where only the angular gradient terms are non-vanishing. The leading-order angular equation

---

[30]To accommodate scenarios with non-vanishing black hole spin, we take $\alpha \to 0$, instead of $\tilde{a} \to 0$ as in [28].

then is

$$\frac{\mathrm{d}^2 S_0}{\mathrm{d}\theta^2} + \left(\cot\theta + 2\tan\theta + \frac{\tan\theta}{\chi\cos\theta - 1} - \frac{\tan\theta}{\chi\cos\theta + 1}\right)\frac{\mathrm{d}S_0}{\mathrm{d}\theta}$$
$$+ \left(m\chi - \frac{m^2}{\sin^2\theta} + \frac{m\sec\theta}{\chi\cos\theta - 1} + \frac{m\sec\theta}{\chi\cos\theta + 1}\right)S_0 = 0\,. \tag{B.5}$$

Although (B.5) is not the general Legendre equation, the associated Legendre functions $P_{\pm(m\pm1),m}$ are solutions to this equation, with the upper (lower) sign denoting solutions with positive (negative) m. Substituting these solutions into (B.4), and taking the appropriate scale factors $\{1, r, r\sin\theta\}$ into account, we find that

$$A^i_{(0)} \propto Y^i_{j,jm}\,, \tag{B.6}$$

with $j = |m|$. The relation in (B.6) shows that the limit (B.3) recovers a special type of magnetic mode, subject to the restriction $j = |m|$. It remains an open problem to obtain separated equations for all magnetic modes in the Kerr background, and it would be nice to understand if the other magnetic modes can also be recovered from the ansatz (2.20) or to show conclusively that this is not possible.

B.2   Higher-Order Corrections

In §3.1.3, we showed that the equations of motion at higher orders in α can be solved iteratively by treating the lower-order solutions as source terms; cf. (3.23). In the following, we discuss in more detail how these inhomogeneous equations can be solved through the method of variation of parameters.

Imposing the relevant boundary conditions at the horizon and at infinity, the near and far-zone solutions of the scalar field are

$$R_i^{\mathrm{near}}(z) = \mathcal{C}_i^{\mathrm{near}} n_c(z) - n_c(z)\int_0^z \mathrm{d}t\,\frac{J_i^z(t)n_d(t)}{W_n(t)} + n_d(z)\int_0^z \mathrm{d}t\,\frac{J_i^z(t)n_c(t)}{W_n(t)}\,,$$
$$R_i^{\mathrm{far}}(x) = \mathcal{C}_i^{\mathrm{far}} f_c(x) + f_c(x)\int_x^\infty \mathrm{d}t\,\frac{J_i^x(t)f_d(t)}{W_f(t)} - f_d(x)\int_x^\infty \mathrm{d}t\,\frac{J_i^x(t)f_c(t)}{W_f(t)}\,, \tag{B.7}$$

where we defined the homogeneous solutions of the leading-order equations of motion as

$$n_c(z) \equiv \left(\frac{z}{z+1}\right)^{iP_+}{}_2F_1(-\ell, \ell+1, 1-2iP_+, 1+z)\,,$$
$$n_d(z) \equiv z^{iP_+}(z+1)^{iP_+}{}_2F_1\left(-\ell+2iP_+, \ell+1+2iP_+, 1+2iP_+, 1+z\right)\,,$$
$$f_c(x) \equiv e^{-x/2}x^\ell\,U(\ell+1-\nu_0, 2+2\ell, x)\,, \tag{B.8}$$
$$f_d(x) \equiv e^{-x/2}x^\ell\,{}_1F_1(\ell+1-\nu_0, 2+2\ell, x)\,,$$

and introduced the Wronskian $W_n \equiv W[n_c, n_d] = n_c n_d' - n_d n_c'$ (and similarly for W_f), with the prime denoting a derivative with respect to the argument of the function. In general, the integrals in (B.7) cannot be solved analytically. However, to perform the matched asymptotic expansions, we are only interested in the asymptotic expansions of these integrals. To avoid clutter, we will

work with the z and x-coordinates for the near and far-zone solutions, instead of converting them to the matching coordinate ξ. Recall that the limit $\alpha \to 0$ of the asymptotic expansions in terms of ξ is equivalent to taking the limits $z \to \infty$ and $x \to 0$.

We first consider the integrals for the far-zone solutions. It is convenient to rewrite these integrals in the following general form

$$\int_x^\infty dt\, \frac{J_i^x(t)f(t)}{W_f(t)} \equiv \int_x^\infty dt\, e^{-t} H_i^x(t)\,, \tag{B.9}$$

where the exponential factor regulates all divergences in the limit $t \to \infty$. To obtain the asymptotic series in the limit $x \to 0$, we Taylor expand $H_i^x(t)$ for $t \to 0$. The result can be organized in the following way [42]

$$\begin{aligned}
\int_x^\infty dt\, e^{-t} H_i^x(t) = &\int_x^\infty dt\, e^{-t} \sum_{k=N_{\min}}^{-1} \sum_{m=0}^{\infty} a_{k,m} t^k \log^m(t) \\
&+ \int_0^\infty dt\, e^{-t} \left[H_i^x(t) - \sum_{k=N_{\min}}^{-1} \sum_{m=0}^{\infty} a_{k,m} t^k \log^m(t) \right] \\
&- \int_0^x dt\, e^{-t} \sum_{k=0}^{\infty} \sum_{m=0}^{\infty} a_{k,m} t^k \log^m(t)\,,
\end{aligned} \tag{B.10}$$

where $a_{k,m}$ are constants, and $N_{\min}$ is the smallest power that appears in the series. The first line in (B.10) consists of terms that converge as $t \to \infty$, the second line is a constant, while the third line consists of terms that diverge as $t \to \infty$, but converge as $t \to 0$. This is why we have rewritten the integral limits $\int_x^\infty \to \int_0^\infty - \int_0^x$ in the last line. Written in this form, (B.10) can be integrated term by term to give the asymptotic series as $x \to 0$.

Similarly, in the near zone, we encounter integrals of the form

$$\int_0^z dt\, \frac{J_i^z(t)n(t)}{W_n(t)} \equiv \int_0^z dt\, e^{-1/t} H_i^z(t)\,, \tag{B.11}$$

where the exponential factor regulates potential divergences for $t \to 0$. To obtain the asymptotic expansion as $z \to \infty$, we Taylor expand $H_i^z(t)$ for $t \to \infty$. The integral then becomes

$$\begin{aligned}
\int_0^z dt\, e^{-1/t} H_i^z(t) = &\int_0^z dt\, e^{-1/t} \sum_{k=-1}^{N_{\max}} \sum_{m=0}^{\infty} a_{k,m} t^k \log^m(t) \\
&+ \int_0^\infty dt\, e^{-1/t} \left[H_z(t) - \sum_{k=-1}^{N_{\max}} \sum_{m=0}^{\infty} a_{k,m} t^k \log^m(t) \right] \\
&- \int_z^\infty dt\, e^{-1/t} \sum_{k=-\infty}^{-2} \sum_{m=0}^{\infty} a_{k,m} t^k \log^m(t)\,,
\end{aligned} \tag{B.12}$$

where $N_{\max}$ is the maximum power of the integrand (which varies depending on the form of J_i^z). The reasoning behind the organization of (B.12) is similar to that for (B.10): the first line

53

converges as $t \to 0$, the second line is a constant, and the third line is convergent as $t \to \infty$. To evaluate the integrals in (B.12), it is convenient to perform the coordinate transformation $s \equiv 1/t$, such that they become directly analogous to the integrals in (B.10).

B.3 Ordinary Perturbation Theory

In the main text, we have argued that the $\ell > 0$ modes can be treated by extrapolating the far-zone solutions towards the outer horizon, $x \to 0$, and solve the spectra using ordinary perturbation theory. Here, we will provide further details of that claim, We will also present results for the higher-order electric angular problem that were omitted in §3.2.1.

To compute the higher-order eigenvalues, we take the inner product of the general equations of motion (3.23) with the zeroth-order eigenstates

$$0 = \int w\, X_0^* \, \Box^{(0)} X_i = \int w\, X_0^* \, J_i^X \,, \tag{B.13}$$

where w is the Sturm-Louiville weight factor and the integral is performed with respect to the relevant coordinate. The left-hand side vanishes after using the hermiticity of $\Box^{(0)}$ and the leading-order equations of motion. The eigenvalues, which are contained in J_i^X, are then computed at every order by performing this integral. At each order in α, we may back-substitute the eigenvalues and equations of motion of the previous order to simplify J_i^X.

The angular equations for the scalar field are trivially solved, since $J_i^\theta = 0$ up to the order of interest, cf. (3.24). For the vector field, on the other hand, the higher-order angular equations contain additional θ-dependent terms on the right-hand side of (2.22), which induce new cross couplings in the angular eigenstates, cf. (3.47). The coefficients in (3.47) are

$$b_{j-2} = -\left[\frac{(j^2 - m^2)[(j-1)^2 - m^2]}{(2j-3)(2j-1)^2(2j+1)} \right]^{1/2} \frac{(j+1-\lambda_0)}{\lambda_0^2(2j-1)} \,,$$

$$b_{j+2} = -\left[\frac{[(j+1)^2 - m^2][(j+2)^2 - m^2]}{(2j+1)(2j+3)^2(2j+5)} \right]^{1/2} \frac{(j+\lambda_0)}{\lambda_0^2(2j+3)} \,, \tag{B.14}$$

and $c_{j\pm2} = 2m\lambda_0^{-5} b_{j\pm2}$. These expressions are valid for both $\lambda_0 = \lambda_0^\pm$. Up to order α^3, the angular eigenvalues for the $j = \ell \pm 1$ modes are

$$\lambda = \lambda_0 - \frac{\alpha \tilde{a} m}{\lambda_0} - \left(\frac{\lambda_0}{2n^2(2\lambda_0 - 1)} - \frac{\tilde{a}^2(\lambda_0 + 1)(\lambda_0^2 - m^2)}{\lambda_0^3(2\lambda_0 + 1)} \right) \alpha^2$$

$$+ \left(\frac{1}{n^2(2\lambda_0 - 1)} + \frac{\tilde{a}^2(2 + \lambda_0)(\lambda_0^2 - m^2)}{\lambda_0^5(2\lambda_0 + 1)} \right) \tilde{a} m \alpha^3 \,. \tag{B.15}$$

These results are substituted into the radial equations to solve for the energy eigenvalues at higher orders.

For the radial equations, we restrict ourselves to the far-zone radial equations and impose regular boundary conditions at $x = 0$. The latter assumption allows us to remove derivative terms in J_i^x through integrations by parts. For a scalar field, the leading-order far-zone solution

54

can be written as

$$R_0^{\text{far}}(x) = \sqrt{\frac{(n-\ell-1)!}{2n(n+\ell)!}}\, e^{-x/2} x^\ell L_{n-\ell-1}^{(2\ell+1)}(x)\,, \qquad \text{(B.16)}$$

where $L_k^{(\rho)}$ is the associated Laguerre polynomial. The overall coefficient has been fixed by requiring the integral of the square of the mode function to be unity. Each term in the inner product (B.13) then has the following generic form

$$\langle x^{-s} \rangle \equiv \frac{(n-\ell-1)!}{2n(n+\ell)!} \int_0^\infty \mathrm{d}x\, e^{-x} x^{2\ell+2-s} \left(L_{n-\ell-1}^{(2\ell+1)}\right)^2 \,, \qquad \text{(B.17)}$$

where $J_i^x \supset x^{-s}$, with positive integer s. We may then compute the energy eigenvalues through the following identities

$$\left\langle \frac{1}{x} \right\rangle = \frac{1}{2n}\,, \qquad\qquad \left\langle \frac{1}{x^2} \right\rangle = \frac{1}{2n(2\ell+1)}\,,$$

$$\left\langle \frac{1}{x^3} \right\rangle = \frac{1}{2\ell(2\ell+1)(2\ell+2)}\,, \qquad \left\langle \frac{1}{x^4} \right\rangle = \frac{3n^2-\ell^2-\ell}{n(2\ell-1)(2\ell)(2\ell+1)(2\ell+2)(2\ell+3)}\,, \qquad \text{(B.18)}$$

which are valid for all ℓ. The fact that $\langle x^{-3} \rangle$ and $\langle x^{-4} \rangle$ diverge for $\ell = 0$ reflects the sensitivity of these modes to the near region of the black hole. In general, the presence of these terms indicates a breakdown of ordinary perturbation theory, and calculating the eigenvalues requires the more rigorous matched asymptotic expansion. However, in the case of a scalar field, these terms have coefficients that are proportional to m, which vanish for $\ell = 0$, so that the naively divergent terms do not contribute to the spectrum. Ordinary perturbation theory, with the assumption of a regular boundary condition at the horizon, is therefore sufficient for the scalar spectrum.

Although the far-zone radial equations of the scalar and vector fields are different, the inner product (B.17) is also valid for the vector case. This is because the additional power of x that appears in the radial solution for a vector field cancels, as the Sturm-Liouville weight factor is now 1, instead of x^2 for the scalar case. The identities (B.18) are therefore also valid for the vector field. Unlike in the scalar case, however, the coefficients of the $\langle x^{-3} \rangle$ and $\langle x^{-4} \rangle$ terms do not vanish for the vector $\ell = 0$ modes, so ordinary perturbation theory is expected to yield divergent results. Indeed, these divergences can be written as divergent boundary terms in the integral (B.17). Remarkably, however, if these boundary terms are discarded, we obtain results that agree with those obtained through the more rigorous matched asymptotic expansion. Since an implicit assumption in deriving the rules (B.18) is precisely that any boundary terms are negligible, substituting them into the divergent operators can still provide finite results. Indeed, we find that the coefficients of the $\langle x^{-3} \rangle$ and $\langle x^{-4} \rangle$ terms are precisely such that the divergences for $\ell = 0$ cancel in the sum. As a consequence of this cancellation, ordinary perturbation theory gives the correct results even for the fine and hyperfine splittings of vector spectrum. Interestingly, two wrongs *can* make a right.

C   Details of the Numerical Treatment

A large part of the analysis presented in Section 4 was focused on achieving accurate numeric results for the quasi-bound state spectrum without a separable ansatz. In §4.2.2, we presented a schematic outline for how one translates the unseparated Proca equation and Lorenz constraint into a nonlinear eigenvalue problem that can be readily solved on a computer. In the interest of pedagogy, we kept technical details there to a minimum, and will instead provide them in this appendix.

We first detail the decomposition of the Proca equation into its temporal, radial, and angular components using the vector spherical harmonics defined in §A.2, and describe how to choose these harmonics such that the quasi-bound state boundary conditions are satisfied. We then detail the construction of the finite-dimensional matrix, whose nonlinear eigenvalues determine the bound state spectrum. Finally, in §C.4, we provide a brief introduction to Chebyshev interpolation with an emphasis on its convergence properties and numeric implementation.

C.1   Decomposition of the Proca Equation

Our numerical analysis relies on a $1+1+2$ decomposition of the Proca equation into its temporal, radial and angular components. While such a decomposition is straightforward for a scalar field, the vector index complicates things. It will therefore be useful to first rewrite the Proca equation as a set of coupled scalar equations, reminiscent of the decomposed Klein-Gordon equation (4.25), with operators that act simply on the scalar spherical harmonics.

To this end, we introduce a basis of vector fields $e_a{}^\mu \partial_\mu$ and dual form fields $f^a{}_\mu \, dx^\mu$, where $a = 0, 1, 2, 3$. These bases are dual to one another in the sense that

$$
\begin{aligned}
\bar{e}_a{}^\mu f^b{}_\mu &= \delta_b^a \,, \\
\bar{e}_a{}^\mu f^a{}_\nu &= \delta_\nu^\mu \,,
\end{aligned}
\tag{C.1}
$$

where the bar denotes complex conjugation. Taking the vector fields to have definite angular momentum, we may write

$$
e_0{}^\mu \partial_\mu = F_t(r)\,\partial_t \,, \quad e_1{}^\mu \partial_\mu = \chi_{1,1}^i \,\partial_i \,, \qquad e_2{}^\mu \partial_\mu = \chi_{1,0}^i \,\partial_i \,, \qquad e_3{}^\mu \partial_\mu = \chi_{1,-1}^i \,\partial_i \,, \tag{C.2}
$$

$$
f^0{}_\mu\, dx^\mu = F_t^{-1}\, dt \,, \quad f^1{}_\mu\, dx^\mu = \chi_i^{1,1}\, dx^i \,, \quad f^2{}_\mu\, dx^\mu = \chi_i^{1,0}\, dx^i \,, \quad f^3{}_\mu\, dx^\mu = \chi_i^{1,-1}\, dx^i \,. \tag{C.3}
$$

where we have used the forms and vectors defined in the previous section. By design, these forms are well-behaved under the Kerr isometries,

$$
\pounds_t f^a{}_\mu = 0 \,, \quad \pounds_z f^0{}_\mu = 0 \,, \quad \text{and} \quad \pounds_z f^i{}_\mu = (2 - i) f^i{}_\mu \,, \quad \text{where} \quad i = 1, 2, 3 \,, \tag{C.4}
$$

and are eigenstates of the angular momentum operator, $\pounds^2 f^0{}_\mu = 0$ and $\pounds^2 f^i{}_\mu = 2 f^i{}_\mu$. Similar relations hold for the basis of vectors, $e_a{}^\mu$. Finally, it is useful to note that

$$
\begin{aligned}
\partial_\mu &= \bar{f}^a{}_\mu e_a{}^\nu \partial_\nu \\
&= i \bar{f}^0{}_\mu F_t \pounds_t + \delta_\mu^r \partial_r + \bar{f}^1{}_\mu F_\theta \mathcal{D}_+ + \bar{f}^2{}_\mu F_\theta \mathcal{D}_0 + \bar{f}^3{}_\mu F_\theta \mathcal{D}_- \,.
\end{aligned}
\tag{C.5}
$$

Our goal is to rewrite the Proca equation,[31] $\nabla^2 A_\mu = A_\mu$, and the Lorenz condition, $\nabla^\mu A_\mu = 0$, into a form that is (roughly) a system of coupled scalar differential equations. We assume that A_μ is in a state of definite frequency and azimuthal angular momentum,

$$\begin{aligned}
\pounds_t A_\mu &= -\omega A_\mu\,, \\
\pounds_z A_\mu &= +m A_\mu\,,
\end{aligned} \tag{C.6}$$

and write $A_\mu = A_a f^a{}_\mu$.

We begin by noting that, for any scalar Φ, the purely radial derivative operator $\partial_r(\Delta\partial_r)$ can be rewritten using the Laplacian ∇^2 and isometry generators $\pounds^2$, $\pounds_t$ and $\pounds_z$:

$$\partial_r\left(\Delta\partial_r\Phi\right) = \left[\Sigma\nabla^2 + \pounds^2 - \left(\Sigma + \frac{2\alpha r(r^2 + \alpha^2\tilde{a}^2)}{\Delta}\right)\pounds_t^2 - \frac{\alpha^2\tilde{a}^2}{\Delta}\pounds_z^2 - \frac{4\alpha^2\tilde{a}r}{\Delta}\pounds_t\pounds_z\right]\Phi\,. \tag{C.7}$$

For the Klein-Gordon equation, this almost immediately yields the decomposition into temporal, radial, and angular degrees of freedom we are after. The Proca equation requires a bit more work, but eventually can be written as

$$\begin{aligned}
0 ={}& \bar{e}_b{}^\mu \Delta^{-1}\Sigma\left(\nabla^2 - 1\right)\left(A_a f^a{}_\mu\right) \\
={}& \left[\frac{1}{\Delta}\partial_r(\Delta\partial_r) - \frac{1}{\Delta}\left(\pounds^2 + \alpha^2\tilde{a}^2\left(1 - \omega^2\right)\cos^2\theta\right)\right. \\
&\left. - (1-\omega^2) + \frac{P_+^2}{(r-r_+)^2} + \frac{P_-^2}{(r-r_-)^2} - \frac{A_+}{(r-r_+)(r_+-r_-)} + \frac{A_-}{(r-r_-)(r_+-r_-)}\right]A_b \\
&+ \mathcal{S}_b{}^a A_a + \mathcal{Q}_b{}^a \pounds_z A_a + \mathcal{R}_b{}^a \partial_r A_a + \mathcal{P}_b{}^a \mathcal{D}_+ A_a + \mathcal{Z}_b{}^a \mathcal{D}_0 A_a + \mathcal{M}_b{}^a \mathcal{D}_- A_a\,, \tag{C.8}
\end{aligned}$$

where we have introduced the following 'mixing matrices':

$$\begin{aligned}
\mathcal{S}_b{}^a &= \frac{1}{\Delta}\bar{e}_b{}^\mu\left[\Sigma\nabla^2 f^a{}_\mu - \frac{\alpha^2\tilde{a}^2}{\Delta}\pounds_z^2 f^a{}_\mu + \frac{4\alpha^2\tilde{a}\omega r}{\Delta}\pounds_z f^a{}_\mu - 2i\omega F_t\Sigma\,\bar{f}^0{}_\rho\nabla^\rho f^a{}_\mu\right]\,, \\
\mathcal{Q}_b{}^a &= -\frac{2\alpha^2\tilde{a}^2}{\Delta^2}\bar{e}_b{}^\mu \pounds_z f^a{}_\mu\,, \qquad \mathcal{R}_b{}^a = 2\Sigma\Delta^{-1}\bar{e}_b{}^\mu\nabla^\rho f^a{}_\mu \delta^r_\rho\,, \\
\mathcal{P}_b{}^a &= 2\Sigma\Delta^{-1}\bar{e}_b{}^\mu\nabla^\rho f^a{}_\mu \bar{f}^1{}_\rho F_\theta\,, \quad \mathcal{Z}_b{}^a = 2\Sigma\Delta^{-1}\bar{e}_b{}^\mu\nabla^\rho f^a{}_\mu \bar{f}^2{}_\rho F_\theta\,, \\
\mathcal{M}_b{}^a &= 2\Sigma\Delta^{-1}\bar{e}_b{}^\mu\nabla^\rho f^a{}_\mu \bar{f}^3{}_\rho F_\theta\,. \tag{C.9}
\end{aligned}$$

Similarly, the Lorenz condition can be written as

$$0 = \mathcal{T}^0 A_0 + \mathcal{S}^i A_i + \mathcal{R}^i \partial_r A_i + \mathcal{P}^i \mathcal{D}_+ A_i + \mathcal{Z}^i \mathcal{D}_0 A_i + \mathcal{M}^i \mathcal{D}_- A_i\,, \tag{C.10}$$

---

[31] At a technical level, the Proca equation with a lowered index is much simpler than with the upper index and so we focus exclusively on this form.

where we have defined the 'mixing vectors':

$$\mathcal{S}^i = \nabla^\mu f^i{}_\mu - i\omega F_t f^i{}_\mu g^{\mu\lambda} \bar{f}^0{}_\lambda \,, \qquad \mathcal{R}^i = f^i{}_\mu g^{\mu r} \,, \qquad \mathcal{P}^i = f^i{}_\mu g^{\mu\lambda} \bar{f}^1{}_\lambda F_\theta \,,$$
$$\mathcal{Z}^i = f^i{}_\mu g^{\mu\lambda} \bar{f}^1{}_\lambda F_\theta \,, \qquad \mathcal{M}^i = f^i{}_\mu g^{\mu\lambda} \bar{f}^1{}_\lambda F_\theta \,, \qquad \mathcal{T}^0 = iF_t^{-1}\big(mg^{t\phi} - \omega g^{tt}\big). \tag{C.11}$$

These mixing matrices and vectors encode how the temporal and spatial components couple to one another and how the Kerr geometry distinguishes scalar and vector fields.

C.2 Boundary Conditions

So far, the radial functions F_r, F_θ, F_t have not been specified. We are free to choose these functions in such a way that all of the components A_a scale in the same way as $r \to r_+$ and $r \to \infty$. This will make it easy to impose the ingoing boundary conditions at the outer horizon and the decaying boundary conditions at spatial infinity.

Let us first concentrate on the behavior at the event horizon, which will be easiest to analyze using the standard form of the Proca equation $\nabla^2 A_\mu = A_\mu$ instead of the decomposition (C.8). We demand that A_μ is an eigenstate of both frequency $\pounds_t A_\mu = -\omega A_\mu$ and angular momentum, $\pounds_z A_\mu = m A_\mu$, and so the coefficients A_μ can all be written as $A_\mu = A_\mu(r,\theta)\, e^{-i\omega t + im\phi}$. We can then solve the Lorenz condition for $A_0(r,\theta)$ and eliminate it from the Proca equation to attain equations of motion that only involve the A_i. While the system of equations is quite complicated, for what follows, we only need to consider the asymptotic behavior of these equations as $r \to r_+$. We will thus use (...) to denote functions that are constant in r (though they generally depend on θ, $r_\pm$, m and ω) and whose precise form are irrelevant to the discussion.

With the benefit of hindsight, we take

$$A_r = \left(\frac{r - r_-}{r - r_+}\right) \tilde{A}_r \,, \quad A_\theta = (r - r_-)\tilde{A}_\theta \,, \quad A_\phi = (r - r_-)\tilde{A}_\phi \,. \tag{C.12}$$

With these factors peeled off, the near-horizon behavior for the r, θ, ϕ components of the Proca equation are

$$0 = \partial_r^2 \tilde{A}_r + \frac{1}{r - r_+}\partial_r \tilde{A}_r + \frac{P_+^2}{(r - r_+)^2}\tilde{A}_r + \frac{(\dots)}{r - r_+}\partial_\theta \tilde{A}_\theta + \frac{(\dots)}{r - r_+}\partial_\theta^2 \tilde{A}_r + (\dots)\partial_r \tilde{A}_\theta$$
$$+ \frac{(\dots)}{r - r_+}\partial_\theta \tilde{A}_r + \frac{(\dots)}{r - r_+}\tilde{A}_\phi + \frac{(\dots)}{r - r_+}\tilde{A}_\theta + \cdots \,, \tag{C.13}$$

$$0 = \partial_r^2 \tilde{A}_\theta + \frac{1}{r - r_+}\partial_r \tilde{A}_\theta + \frac{P_+^2}{(r - r_+)^2}\tilde{A}_\theta + \frac{(\dots)}{r - r_+}\partial_\theta \tilde{A}_r + \frac{(\dots)}{r - r_+}\partial_\theta \tilde{A}_\theta$$
$$+ \frac{(\dots)}{r - r_+}\partial_\theta^2 \tilde{A}_\theta + \frac{(\dots)}{r - r_+}\tilde{A}_\phi + (\dots)\partial_r \tilde{A}_r + (\dots)\tilde{A}_r + \cdots \,, \tag{C.14}$$

$$0 = \partial_r^2 \tilde{A}_\phi + \frac{1}{r - r_+}\partial_r \tilde{A}_\phi + \frac{P_+^2}{(r - r_+)^2}\tilde{A}_\phi + (\dots)\left(\partial_r^2 \tilde{A}_r + \frac{1}{r - r_+}\partial_r \tilde{A}_r + \frac{P_+^2}{(r - r_+)^2}\tilde{A}_r\right)$$
$$+ \frac{(\dots)}{r - r_+}\tilde{A}_\theta + (\dots)\partial_r \tilde{A}_\theta + (\dots)\partial_r\partial_\theta \tilde{A}_\theta + (\dots)\partial_\theta \tilde{A}_r + \frac{(\dots)}{r - r_+}\partial_\theta \tilde{A}_\theta$$
$$+ \frac{(\dots)}{r - r_+}\partial_\theta \tilde{A}_\phi + (\dots)\partial_\theta^2 \tilde{A}_\theta + \frac{(\dots)}{(r - r_+)}\partial_\theta^2 \tilde{A}_\phi + \cdots \,. \tag{C.15}$$

58

We see that most singular terms imply that $\tilde{A}_r$, $\tilde{A}_\theta$, $\tilde{A}_\phi$ all go as $(r - r_+)^{\pm i P_+}$ as $r \to r_+$. In a similar way, we can also examine the Lorenz condition as $r \to r_+$,

$$A_0 = (\ldots)(r - r_+)\tilde{A}_r + (r - r_+)\partial_r\tilde{A}_r + (\ldots)(r - r_+)\partial_\theta\tilde{A}_\theta + (\ldots)(r - r_+)\tilde{A}_\theta + (\ldots)\tilde{A}_\phi \,, \quad \text{(C.16)}$$

and we see that A_0 also approaches $(r - r_+)^{\pm i P_+}$ as $r \to r_+$. With these scalings in mind, we take the radial functions to be

$$F_t = 1 \,, \quad F_r = \frac{r - r_+}{r - r_-} \,, \quad F_\theta = \frac{1}{r - r_-} \,, \quad \text{(C.17)}$$

so that $A_a \sim (r - r_+)^{\pm i P_+}\left(1 + \mathcal{O}(r - r_+)\right)$ as $r \to r_+$ for each a.

To analyze how the coefficients A_a behave as $r \to \infty$, we turn to the decomposed Proca equation (C.8), where the mixing matrices are computed with the radial functions (C.17). Ignoring the mixing matrices, for a moment, (C.8) predicts that the A_a scale in the same way as the scalar solution (3.6):

$$A_a \sim r^{-1-\nu+2\alpha^2/\nu}e^{-\sqrt{1-\omega^2}(r-r_+)}\left(1 + \mathcal{O}(r^{-1})\right). \quad \text{(C.18)}$$

This conclusion will not be affected by including the mixing matrices, as long as they decay faster at spatial infinity than r^{-1} and, by explicit computation, we confirm that $\mathcal{S}_0{}^0 = 0$, $\{\mathcal{S}_0{}^i, \mathcal{S}_i{}^0, \mathcal{R}_0{}^0, \mathcal{R}_i{}^j\}$ scale as r^{-2}, $\{\mathcal{S}_i{}^j, \mathcal{R}_0{}^i, \mathcal{R}_i{}^0, \mathcal{P}_0{}^0, \mathcal{P}_i{}^j, \mathcal{Z}_0{}^j, \mathcal{Z}_i{}^j, \mathcal{M}_0{}^0, \mathcal{M}_i{}^j\}$ scale as r^{-3}, while the rest decay as r^{-4}.

We have chosen the radial functions (C.17), so that the components A_a all have the same asymptotic behavior as $r \to r_+$ and $r \to \infty$. We then peel off this asymptotic behavior by writing

$$A_a(r) = \left(\frac{r - r_+}{r - r_-}\right)^{i P_+}(r - r_-)^{-1+\nu-2\alpha^2/\nu}\, e^{-\alpha(r-r_+)/\nu}B_a(r) \,, \quad \text{(C.19)}$$

and work with the functions B_a, which, for the modes of interest, approach constants as $r \to r_+$ and $r \to \infty$. In the numerics, this allows us to impose the boundary conditions for the quasi-bound states by simply expanding B_a in a set of functions that approach constant values at the boundaries.

C.3 Constructing the Matrix Equation

To convert (C.8) into a finite-dimensional matrix equation, we first write (C.19) as

$$A_a(r) = \left(\frac{r - r_+}{r - r_-}\right)^{i P_+}(r - r_-)^{-1+\nu-2\alpha^2/\nu}e^{-\alpha(r-r_+)/\nu}B_a(\zeta(r)) \equiv F(r)B_a(\zeta(r)) \,, \quad \text{(C.20)}$$

which is similar to the scalar case (4.9), with $\zeta(r)$ a map from $[r_+, \infty)$ to $[-1, 1]$. The spatial components $i = 1, 2, 3$ of the Proca equation (C.8) can then be written as

$$\mathcal{D}_i{}^k[B_k] + \mathcal{D}_i{}^0[B_0] = 0 \,, \quad \text{(C.21)}$$

where

$$\mathcal{D}_i{}^k[B_k] = \left(\partial_\zeta^2 + \frac{1}{\zeta'(r)}\left(\frac{1}{r-r_+} + \frac{1}{r-r_-} + \frac{2F'(r)}{F(r)} + \frac{\zeta''(r)}{\zeta'(r)}\right)\partial_\zeta\right)B_i$$

$$- \frac{1}{\zeta'(r)^2\Delta}\left(\pounds^2 + \alpha^2\tilde{a}^2\left(1-\omega^2\right)\cos^2\theta\right)B_i + \frac{1}{\zeta'(r)^2}\left(\frac{F'/F}{r-r_+} + \frac{F'/F}{r-r_-} + \frac{F''}{F}\right.$$

$$\left. - (1-\omega^2) + \frac{P_+^2}{(r-r_+)^2} + \frac{P_-^2}{(r-r_-)^2} - \frac{A_+}{(r-r_+)(r_+-r_-)} + \frac{A_-}{(r-r_-)(r_+-r_-)}\right)B_i$$

$$+ \tilde{\mathcal{S}}_i{}^k B_k + \tilde{\mathcal{Q}}_i{}^k \pounds_z B_k + \tilde{\mathcal{R}}_i{}^k \partial_\zeta B_k + \tilde{\mathcal{P}}_i{}^k \mathcal{D}_+ B_k + \tilde{\mathcal{Z}}_i{}^k \mathcal{D}_0 B_k + \tilde{\mathcal{M}}_i{}^k \mathcal{D}_- B_k \,, \quad \text{(C.22)}$$

$$\mathcal{D}_i{}^0[B_0] = \tilde{\mathcal{S}}_i{}^0 B_0 + \tilde{\mathcal{Q}}_i{}^0 \pounds_z B_0 + \tilde{\mathcal{R}}_i{}^0 \partial_\zeta B_i + \tilde{\mathcal{P}}_i{}^0 \mathcal{D}_+ B_0 + \tilde{\mathcal{Z}}_i{}^0 \mathcal{D}_0 B_0 + \tilde{\mathcal{M}}_i{}^0 \mathcal{D}_- B_0 \,. \quad \text{(C.23)}$$

In the above, we have defined the transformed mixing matrices

$$\tilde{\mathcal{S}}_b{}^a = \frac{1}{\zeta'^2}\mathcal{S}_b{}^a + \frac{F'}{\zeta'^2 F}\mathcal{R}_b{}^a\,, \quad \tilde{\mathcal{R}}_b{}^a = \mathcal{R}_b{}^a/\zeta'\,, \quad \tilde{\mathcal{Q}}_b{}^a = \mathcal{Q}_b{}^a/\zeta'^2\,,$$

$$\tilde{\mathcal{P}}_b{}^a = \mathcal{P}_b{}^a/\zeta'^2\,, \quad \tilde{\mathcal{Z}}_b{}^a = \mathcal{Z}_b{}^a/\zeta'^2\,, \quad \tilde{\mathcal{M}}_b{}^a = \mathcal{M}_b{}^a/\zeta'^2\,, \quad \text{(C.24)}$$

where $\zeta' = \partial_r\zeta$. Similarly, the Lorenz condition can be written as

$$\mathcal{D}_0{}^0[B_0] + \mathcal{D}_0{}^i[B_i] = 0\,, \quad \text{(C.25)}$$

where

$$\mathcal{D}_0{}^0[B_0] = \mathcal{T}^0 B_0\,, \quad \text{(C.26)}$$

$$\mathcal{D}_0{}^i[B_i] = \tilde{\mathcal{S}}^i B_i + \tilde{\mathcal{R}}^i \partial_\zeta B_i + \mathcal{P}^i \mathcal{D}_+ B_i + \mathcal{Z}^i \mathcal{D}_0 B_i + \mathcal{M}^i \mathcal{D}_- B_i\,, \quad \text{(C.27)}$$

with $\tilde{\mathcal{S}}^i = \mathcal{S}^i + F'\mathcal{R}^i/F$ and $\tilde{\mathcal{R}}^i = \zeta'\mathcal{R}^i$.

We then expand the temporal component of the field into scalar harmonics and the spatial components into one-form harmonics,

$$B_0 = \sum_{j'} B_{j'm} Y_{j'm}\,, \quad \text{(C.28)}$$

$$B_i = \sum_{\ell',j'} B_{\ell',j'm} Y_i^{\ell',j'm}\,. \quad \text{(C.29)}$$

As discussed in §A.2, the summation ranges of j' and ℓ' depend on the parity of the mode we are solving for. We then project the Proca equation (C.21) onto the vector harmonics and the

Lorenz constraint (C.25) onto the scalar harmonics, to obtain

$$\sum_{\ell',j'}\mathcal{D}^{\text{ss}}_{\ell j\,|\,\ell' j'}[B_{\ell',j'm}(\zeta)] + \sum_{j'}\mathcal{D}^{\text{st}}_{\ell j\,|\,j'}[B_{j'm}(\zeta)] = 0\,, \tag{C.30}$$

$$\sum_{\ell',j'}\mathcal{D}^{\text{ts}}_{j\,|\,\ell' j'}[B_{\ell',j'm}(\zeta)] + \sum_{j'}\mathcal{D}^{\text{tt}}_{j\,|\,j'}[B_{j'm}(\zeta)] = 0\,. \tag{C.31}$$

Explicitly, we find

$$
\begin{aligned}
\mathcal{D}^{\text{ss}}_{\ell j\,|\,\ell' j'}[B_{\ell',j'm}(\zeta)] &= \int_{\text{S}^2}\mathrm{d}\Omega\;\bar{Y}^i_{\ell,jm}\,\mathcal{D}_i{}^k\big[B_{\ell',j'm}(\zeta)Y^{\ell',j'm}_k\big]\,,\\
\mathcal{D}^{\text{st}}_{\ell j\,|\,j'}[B_{j'm}(\zeta)] &= \int_{\text{S}^2}\mathrm{d}\Omega\;\bar{Y}^i_{\ell,jm}\,\mathcal{D}_i{}^0\big[B_{j'm}(\zeta)Y_{j'm}\big]\,,\\
\mathcal{D}^{\text{ts}}_{j\,|\,\ell' j'}[B_{\ell',j'm}(\zeta)] &= \int_{\text{S}^2}\mathrm{d}\Omega\;\bar{Y}_{jm}\,\mathcal{D}_0{}^k\big[B_{\ell',j'm}(\zeta)Y^{\ell',j'm}_k\big]\,,\\
\mathcal{D}^{\text{tt}}_{j\,|\,j'}[B_{j'm}(\zeta)] &= \int_{\text{S}^2}\mathrm{d}\Omega\;\bar{Y}_{jm}\,\mathcal{D}_0{}^0\big[B_{j'm}(\zeta)Y_{j'm}\big]\,.
\end{aligned}
\tag{C.32}
$$

Because we defined the $f^a{}_\mu$ to have definite angular momentum, the harmonics (A.15) and A.26) take simple forms in this tetrad basis. For instance, the components of the one-form harmonics are

$$Y^{\ell,jm}_i = \langle (1\,m_i)\,(\ell\;m - m_i)|j\,m\rangle\,Y_{\ell,m-m_i}(\theta,\phi)\,, \tag{C.33}$$

where $m_i = 2 - i$. In practice, the overlaps (C.32) can be computed efficiently, as each term in the rewritten Proca equation (C.8) operates very simply on these harmonics.

A vector field is a solution of the Proca equation and the Lorenz constraint if and only if (C.30) and (C.31) are satisfied for all j and ℓ. Following the scalar case in §4.2.2, we may approximate the radial functions as

$$B_{\ell',j'm}(\zeta) = \sum_{k=0}^{N} B_{\ell',j'm}(\zeta_k)\,p_k(\zeta) \qquad\text{and}\qquad B_{j'm} = \sum_{k=0}^{N} B_{j'm}(\zeta_k)\,p_k(\zeta)\,, \tag{C.34}$$

where $p_k(\zeta)$ are the cardinal polynomials associated to the points $\{\zeta_k\}$. By substituting these approximations into (C.30) and (C.31), sampling each equation at the $\{\zeta_n\}$, and truncating the angular expansion, we convert this system of equations into a finite-dimensional matrix equation. This matrix, whose structure is depicted in Fig. 15, can then be passed to a nonlinear eigenvalue solver to determine the bound state spectrum.

C.4   Chebyshev Interpolation

Our numerical techniques rely on approximating the scalar and vector field configurations using finite and discrete sets of data. This discretization is a necessary step towards approximating the Klein-Gordon and Proca equations—i.e. partial *differential* equations—as finite-dimensional matrix equations. How we discretize matters immensely, and a careless choice can cause the numerics to fail outright. This section explains both what Chebyshev interpolation is and why

we choose it, and provides various technical details needed for the numerics outlined in §4.1.3. For an excellent introduction to the subject, see [55].

Any smooth function $f(\zeta)$ on the interval $\zeta \in [-1,1]$ has a unique representation in terms of Chebyshev polynomials,

$$f(\zeta) = \sum_{k=0}^{\infty} a_k T_k(\zeta) \,, \tag{C.35}$$

where the Chebyshev polynomials of degree k are $T_k(\cos\theta) = \cos k\theta$. The Chebyshev coefficients are then given by

$$a_k = \frac{2}{\pi} \int_{-1}^{1} d\zeta \, \frac{T_k(\zeta) \, f(\zeta)}{\sqrt{1 - \zeta^2}} \,, \tag{C.36}$$

for $k \geq 1$, while the right-hand side is multiplied by a factor of $1/2$ when $k = 0$. If we define an expanded function on the unit circle, $F(z) = F(1/z) = f(\zeta)$, with $\zeta = (z + z^{-1})/2$, then the Chebyshev expansion (C.35) is nothing more than the unique Laurent series for $F(z)$ and (C.36) is simply a translation of the Cauchy integral formula.

With this expansion in hand, we may define a degree N polynomial approximation to $f(\zeta)$ by truncating the sum,

$$\tilde{f}_N(\zeta) = \sum_{k=0}^{N} a_k T_k(\zeta) \,. \tag{C.37}$$

While this approximation is guaranteed to become exact as $N \to \infty$, its accuracy at finite N depends on how quickly the Chebyshev coefficients decay. This, in turn, depends on the analytic structure of $f(\zeta)$ and thus $F(z)$. Since $f(\zeta)$ is analytic on the interval $\zeta \in [-1,1]$, the expanded function $F(z)$ is necessarily analytic within an annulus about the unit circle, the largest of which we denote $\rho^{-1} \leq |z| \leq \rho$. The Laurent series for $F(z)$ diverges outside of this annulus, and so its size determines the asymptotic behavior of the Chebyshev coefficients, i.e. $a_k < \mathcal{C}\rho^{-k}$ as $k \to \infty$ for some constant $\mathcal{C}$. Since $|T_k(\zeta)| \leq 1$ on the interval, the truncation error scales as

$$|f(\zeta) - \tilde{f}_N(\zeta)| \leq \sum_{k=N+1}^{\infty} |a_k T_k(\zeta)| \leq \frac{\mathcal{C}\rho^{-N}}{\rho - 1} \,, \quad \text{as} \quad N \to \infty \,. \tag{C.38}$$

The Chebyshev approximation (C.37) thus converges to $f(\zeta)$ exponentially quickly, at a rate set by the singularity closest to the unit circle $|z| = 1$. If $F(z)$ is entire, the approximation converges even faster.

Of course, we are mainly interested in the analytic structure of $f(\zeta)$, and not its expanded counterpart $F(z)$. However, we can relate the two by noting that $\zeta = (z + z^{-1})/2$ maps a circle of radius ρ into an ellipse with foci at $\zeta = \pm 1$ defined by

$$\zeta(\theta) = \frac{1}{2} \left(\rho + \frac{1}{\rho} \right) \cos\theta + \frac{i}{2} \left(\rho - \frac{1}{\rho} \right) \sin\theta \,. \tag{C.39}$$

This is called the Bernstein ellipse of radius ρ, depicted in Fig. 16. From the above logic, the size of the largest such ellipse inside which $f(\zeta)$ is analytic then determines how quickly the Chebyshev expansion (C.35) converges, and thus the number of terms needed to approximate
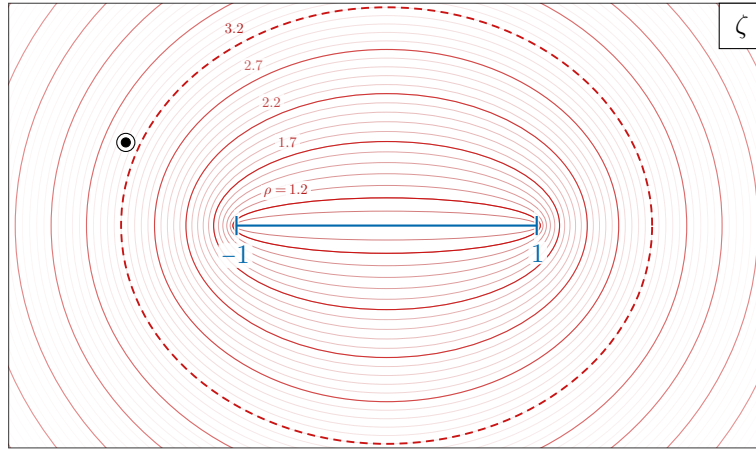
Figure 16: The interval $\zeta \in [-1, 1]$ and Bernstein ellipses of various sizes. The distance between the closest singularity of the function $f(\zeta)$ (pictured as ⊙) and the finite interval determines how quickly the Chebyshev expansion and interpolation converge. As illustrated here, truncation errors roughly decay as $(3.2)^{-N}$.

$f(\zeta)$ to a desired accuracy.

In practice, we will use a different degree N polynomial approximation, called the *interpolant*

$$f_N(\zeta) = \sum_{k=0}^{N} c_k T_k(\zeta) \,, \tag{C.40}$$

that will inherit the convergence properties of the projection (C.37), yet is more convenient and numerically robust. The $N + 1$ coefficients c_k are defined by requiring that $f_N(\zeta_n) = f(\zeta_n)$ at a set of $N + 1$ interpolation points $\{\zeta_n\}$. We may rewrite this interpolant in terms of the degree N *Lagrange polynomials*

$$f_N(\zeta) = \sum_{k=0}^{N} f(\zeta_k) \, p_k(\zeta) \,, \tag{C.41}$$

which are defined with respect to the interpolation points as

$$p_k(\zeta_n) = \delta_{nk} \,. \tag{C.42}$$

Explicitly, the Lagrange polynomials are given by

$$p_n(\zeta) = \frac{\prod_{k \neq n}(\zeta - \zeta_k)}{\prod_{k \neq n}(\zeta_n - \zeta_k)} = \frac{p(\zeta) \, w_n}{(\zeta - \zeta_n)} \,, \tag{C.43}$$

where we have defined both the degree $N + 1$ *node polynomial*

$$p(\zeta) = \prod_{k=0}^{N} (\zeta - \zeta_n) \tag{C.44}$$

and the *weights* $w_n^{-1} = p'(\zeta_n)$.

Whether or not this interpolant accurately approximates $f(\zeta)$ away from the points $\{\zeta_n\}$ depends crucially on how the interpolation points are distributed on the interval. One can show that the difference between the exact function and its approximation is given by [55, 56]

$$f(\zeta) - f_N(\zeta) = \frac{f^{(N+1)}(\zeta)\, p(\zeta)}{(N+1)!} . \tag{C.45}$$

If the interpolation points are such that the maximum value of $|p(\zeta)|$ on the interval does not grow with its degree, then, for large enough N, this difference is guaranteed to be small everywhere on the interval. Given that the Chebyshev polynomial $T_{N+1}(\zeta)$ is both extremely simple in its trigonometric form and is bounded on the interval by ± 1 for all N, we will take $p(\zeta) = T_{N+1}(\zeta)/2^N$ and sample it at its zeros

$$\zeta_k = \cos\left(\frac{\pi(2k+1)}{2(N+1)}\right), \qquad k = 0, \ldots, N , \tag{C.46}$$

with corresponding weights

$$w_k = \sin\left(\frac{2\pi k(N+2) + \pi}{2(N+1)}\right), \qquad k = 0, \ldots, N . \tag{C.47}$$

The interpolant inherits the convergence properties (C.38) of the truncation if we interpolate with the *Chebyshev nodes* (C.46),[32] and so (C.41) converges to $f(\zeta)$ at rate set by the largest Bernstein ellipse.

In practice, evaluating the interpolant (C.41) away from the interpolation points using (C.43) is a numerical disaster [55, 57, 58]. Fortunately, the *second barycentric form*,

$$p_n(\zeta) = \frac{\lambda_n}{\zeta - \zeta_n} \Bigg/ \sum_{k=0}^{N} \frac{\lambda_k}{\zeta - \zeta_k} , \tag{C.48}$$

is numerically robust [57, 59] and computationally efficient. This formula can be used to compute the derivative matrices $p'_k(\zeta_n)$ and $p''_k(\zeta_n)$ that appear throughout the text in a stable way.

---

[32]In fact, any set of interpolation points that are distributed according to the equilibrium distribution, $\rho(\zeta) = (\pi\sqrt{1-\zeta^2})^{-1}$, will share the convergence properties of the truncation (C.37). See [55] for more details.

Explicitly, we take

$$p_k'(\zeta_n) = \begin{cases} \dfrac{w_k/w_n}{\zeta_n - \zeta_k} & n \neq k \\ -\sum\limits_{k \neq n} p_k'(\zeta_n) & n = k \end{cases}, \tag{C.49}$$

$$p_k''(\zeta_n) = \begin{cases} 2p_k'(\zeta_n)p_n'(\zeta_n) - \dfrac{2p_k'(\zeta_n)}{\zeta_n - \zeta_k} & n \neq k \\ -\sum\limits_{k \neq n} p_k''(\zeta_n) & n = k \end{cases}. \tag{C.50}$$

Numerically, it is extremely important [60] to set the diagonal elements of these differentiation matrices such that the sum of all rows vanish identically. This forces the differentiation matrices to annihilate constant functions on the interval and can have an outsized effect on accuracy.

D Notation and Conventions

Symbol	Meaning	Reference
M	Mass of a black hole	(1.2)
a	Spin of a black hole	(1.2)
$\tilde{a}$	Dimensionless spin, $\tilde{a} \equiv a/M$	(2.3)
r_g	Gravitational radius, $r_g \equiv GM/c^2$	(1.1)
Ω_H	Angular velocity at the horizon, $\Omega_H \equiv a/(2Mr_+)$	(1.2)
μ	Mass of a bosonic field	(1.1)
λ_c	Compton wavelength of a bosonic field, $\lambda_c \equiv \hbar/(\mu c)$	(1.1)
α	Gravitational fine structure constant, $\alpha \equiv r_g/\lambda_c$	(1.1)
r_c	Typical Bohr radius, $r_c = (\mu\alpha)^{-1}$	(2.19)
$r_\pm$	Outer (inner) horizon, $r_\pm \equiv M \pm \sqrt{M^2 - a^2}$	(1.2)
$\tilde{r}_\pm$	Dimensionless horizon, $\tilde{r}_\pm \equiv r_\pm/M$	(1.2)
$\hat{r}_\pm$	Additional poles for the electric modes, $\hat{r}_\pm \equiv \pm i\lambda$	(2.24)
$\check{r}_\pm$	Approximate outer (inner) horizons of the magnetic modes	(2.26)
k	Killing vector field	§2.1
$\pounds$	Lie derivative	§2.1
Φ	Ultralight scalar field	(2.1)
A_μ	Ultralight vector field	(2.2)
$\pounds^2$	Total angular momentum operator, $\pounds^2 \equiv \pounds_x^2 + \pounds_y^2 + \pounds_z^2$	(2.7)
R	Radial function in separable ansatz	(2.9), (2.20)
S	Angular function in separable ansatz	(2.9), (2.20)
c^2	Spheroidicity parameter, $c^2 \equiv \alpha^2\tilde{a}^2(\omega^2 - \mu^2)$	(2.10)
$B^{\mu\nu}$	Polarization tensor for electric ansatz	(2.20)
x	Far-zone coordinate, $x \equiv 2\sqrt{\mu^2 - \omega^2}\,(r - r_+)$	(3.5)
y	Intermediate-zone coordinate, $y \equiv \mu(r - r_+)$	(3.28)
z	Near-zone coordinate, $z \equiv (r - r_+)/(r_+ - r_-)$	(3.2)
ξ	Matching coordinate	(3.15), (3.41)
J	Source terms of inhomogeneous equations	(3.23)
ω	Frequency eigenvalue	§2.1
E	Energy eigenvalue, $E \equiv \text{Re}\,\omega$	(2.27)
Γ	Instability rate, $\Gamma \equiv \text{Im}\,\omega$	(2.27)
ν	Rescaled energy eigenvalue, $\nu \equiv \mu\alpha/\sqrt{\mu^2 - \omega^2}$	(2.27), (3.1)
n	Principal quantum number, $n \geq \ell + 1$	§2.1
ℓ	Orbital angular momentum quantum number	§2.1
j	Total angular momentum quantum number	§2.1
m	Azimuthal angular momentum quantum number	§2.1

Symbol	Meaning	Reference
Λ	Angular eigenvalue	(2.10), (2.22)
λ	Electric angular eigenvalue	(2.21)
$\lambda_0^{\pm}$	Leading order electric angular eigenvalues for $j = \ell \pm 1$	(3.30), (3.37)
$\mathcal{M}_{nk}$	Nonlinear eigenvalue matrix of the radial sector	(4.8)
$\mathcal{A}_{nk}$	Nonlinear eigenvalue matrix of the angular sector	(4.21)
ζ	Rescaled coordinate, from $r = (r_+, \infty)$ to $\zeta = (-1, 1)$	(4.18), (4.19)
ζ_n	Chebyshev nodes	(4.13)
p_k	Cardinal polynomials, $p_k(\zeta_n) = \delta_{nk}$	(C.42)
ρ	Size of the Bernstein ellipse	(C.39)
$e_a{}^{\mu}$	Tetrad vector field components	§C.1
$f^a{}_{\mu}$	Tetrad one-form field components	§C.1
A_a	A_{μ}'s components in the tetrad basis, $A_{\mu} = A_a f^a{}_{\mu}$	§C.1
P_{jm}	Associated Legendre polynomial	[53]
Y_{jm}	Scalar spherical harmonic	[53]
$Y^i_{\ell,jm}$	Pure-orbital vector spherical harmonic	[41]
${}_2F_1$	Hypergeometric function	[53]
${}_1F_1$	Confluent hypergeometric function of the first kind	[53]
U	Confluent hypergeometric function of the second kind	[53]
$L_k^{(\rho)}$	Associated Laguerre polynomial	[53]
Γ	Gamma function	[53]
ψ	Digamma function	[53]
γ_E	Euler-Mascheroni constant	[53]
T_n	Chebyshev polynomial	[53]

References

[1] C. Cowan, F. Reines, F. Harrison, H. Kruse, and A. McGuire, "Detection of the Free Neutrino: A Confirmation," *Science* **124** (1956) 103–104.

[2] Y. Fukuda (Super-Kamiokande Collaboration), "Evidence for Oscillation of Atmospheric Neutrinos," *Phys. Rev. Lett.* **81** (1998) 1562–1567, `arXiv:hep-ex/9807003 [hep-ex]`.

[3] Y. Zel'Dovich, "Generation of Waves by a Rotating Body," *JETP Letters* **14** (1971) 180.

[4] Y. Zel'Dovich, "Amplification of Cylindrical Electromagnetic Waves Reflected from a Rotating Body," *Sov. Phys. JETP* **35** (1972) 1085.

[5] A. Arvanitaki, S. Dimopoulos, S. Dubovsky, N. Kaloper, and J. March-Russell, "String Axiverse," *Phys. Rev. D* **81** (2010) 123530, `arXiv:0905.4720 [hep-th]`.

[6] A. Arvanitaki and S. Dubovsky, "Exploring the String Axiverse with Precision Black Hole Physics," *Phys. Rev. D* **83** (2011) 044026, `arXiv:1004.3558 [hep-th]`.

[7] S. Detweiler, "Klein-Gordon Equation and Rotating Black Holes," *Phys. Rev.* **D22** (1980) 2323–2326.

[8] S. Dolan, "Instability of the Massive Klein-Gordon Field on the Kerr Spacetime," *Phys. Rev.* **D76** (2007) 084001, `arXiv:0705.2880 [gr-qc]`.

[9] H. Yoshino and H. Kodama, "Bosenova Collapse of Axion Cloud around a Rotating Black Hole," *Prog. Theor. Phys.* **128** (2012) 153–190, `arXiv:1203.5070 [gr-qc]`.

[10] S. Dolan, "Superradiant Instabilities of Rotating Black Holes in the Time Domain," *Phys. Rev.* **D87** (2013) 124026, `arXiv:1212.1477 [gr-qc]`.

[11] H. Okawa, H. Witek, and V. Cardoso, "Black Holes and Fundamental Fields in Numerical Relativity: Initial Data Construction and Evolution of Bound States," *Phys. Rev.* **D89** (2014) 104032, `arXiv:1401.1548 [gr-qc]`.

[12] H. Yoshino and H. Kodama, "Gravitational Radiation from an Axion Cloud around a Black Hole: Superradiant Phase," *PTEP* **2014** (2014) 043E02, `arXiv:1312.2326 [gr-qc]`.

[13] D. Baumann, H. S. Chia, and R. A. Porto, "Probing Ultralight Bosons with Binary Black Holes," *Phys. Rev.* **D99** (2019) 044001, `arXiv:1804.03208 [gr-qc]`.

[14] R. Brito, V. Cardoso, and P. Pani, "Black Holes as Particle Detectors: Evolution of Superradiant Instabilities," *Class. Quant. Grav.* **32** (2015) 134001, `arXiv:1411.0686 [gr-qc]`.

[15] A. Arvanitaki, M. Baryakhtar, and X. Huang, "Discovering the QCD Axion with Black Holes and Gravitational Waves," *Phys. Rev. D* **91** (2015) 084011, `arXiv:1411.2263 [hep-ph]`.

[16] A. Arvanitaki, M. Baryakhtar, S. Dimopoulos, S. Dubovsky, and R. Lasenby, "Black Hole Mergers and the QCD Axion at Advanced LIGO," *Phys. Rev. D* **95** (2017) 043001, `arXiv:1604.03958 [hep-ph]`.

[17] R. Brito *et al.*, "Stochastic and Resolvable Gravitational Waves from Ultralight Bosons," *Phys. Rev. Lett.* **119** (2017) 131101, `arXiv:1706.05097 [gr-qc]`.

[18] R. Brito *et al.*, "Gravitational Wave Searches for Ultralight Bosons with LIGO and LISA," *Phys. Rev. D* **96** (2017) 064050, `arXiv:1706.06311 [gr-qc]`.

[19] H. Witek, V. Cardoso, A. Ishibashi, and U. Sperhake, "Superradiant Instabilities in Astrophysical Systems," *Phys. Rev.* **D87** (2013) 043513, `arXiv:1212.0551 [gr-qc]`.

[20] P. Pani, V. Cardoso, L. Gualtieri, E. Berti, and A. Ishibashi, "Black Hole Bombs and Photon Mass Bounds," *Phys. Rev. Lett.* **109** (2012) 131102, `arXiv:1209.0465 [gr-qc]`.

[21] P. Pani, V. Cardoso, L. Gualtieri, E. Berti, and A. Ishibashi, "Perturbations of Slowly Rotating Black Holes: Massive Vector Fields in the Kerr Metric," *Phys. Rev.* **D86** (2012) 104017, `arXiv:1209.0773 [gr-qc]`.

[22] S. Endlich and R. Penco, "A Modern Approach to Superradiance," *JHEP* **05** (2017) 052, `arXiv:1609.06723 [hep-th]`.

[23] M. Baryakhtar, R. Lasenby, and M. Teo, "Black Hole Superradiance Signatures of Ultralight Vectors," *Phys. Rev.* **D96** (2017) 035019, `arXiv:1704.05081 [hep-ph]`.

[24] W. East and F. Pretorius, "Superradiant Instability and Backreaction of Massive Vector Fields around Kerr Black Holes," *Phys. Rev. Lett.* **119** (2017) 041101, `arXiv:1704.04791 [gr-qc]`.

[25] W. East, "Superradiant Instability of Massive Vector Fields around Spinning Black Holes in the Relativistic Regime," *Phys. Rev.* **D96** (2017) 024004, `arXiv:1705.01544 [gr-qc]`.

[26] W. East, "Massive Boson Superradiant Instability of Black Holes: Nonlinear Growth, Saturation, and Gravitational Radiation," *Phys. Rev. Lett.* **121** (2018) 131104, `arXiv:1807.00043 [gr-qc]`.

[27] V. Cardoso, Ó. Dias, G. Hartnett, M. Middleton, P. Pani, and J. Santos, "Constraining the Mass of Dark Photons and Axion-Like Particles Through Black Hole Superradiance," *JCAP* **1803** (2018) 043, `arXiv:1801.01420 [gr-qc]`.

[28] S. Dolan, "Instability of the Proca Field on Kerr Spacetime," *Phys. Rev.* **D98** (2018) 104006, `arXiv:1806.01604 [gr-qc]`.

[29] D. Baumann, H. S. Chia, R. A. Porto, and J. Stout, *to appear.*

[30] O. Hannuksela, K. Wong, R. Brito, E. Berti, and T. Li, "Probing the Existence of Ultralight Bosons with a Single Gravitational-Wave Measurement," *Nat. Astron.* **3** (2019) 447–451, `arXiv:1804.09659 [astro-ph.HE]`.

[31] J. Zhang and H. Yang, "Gravitational Floating Orbits around Hairy Black Holes," *Phys. Rev.* **D99** (2019) 064018, `arXiv:1808.02905 [gr-qc]`.

[32] E. Berti, R. Brito, C. Macedo, G. Raposo, and J. Rosa, "Ultralight Boson Cloud Depletion in Binary Systems," *Phys. Rev.* **D99** (2019) 104039, `arXiv:1904.03131 [gr-qc]`.

[33] J. Zhang and H. Yang, "Dynamic Signatures of Black Hole Binaries with Superradiant Clouds," `arXiv:1907.13582 [gr-qc]`.

[34] P. Krtous, V. Frolov, and D. Kubiznak, "Separation of Maxwell Equations in Kerr–NUT–(A)dS Spacetimes," *Nucl. Phys.* **B934** (2018) 7–38, `arXiv:1803.02485 [hep-th]`.

[35] V. Frolov, P. Krtous, D. Kubiznak, and J. Santos, "Massive Vector Fields in Rotating Black-Hole Spacetimes: Separability and Quasinormal Modes," *Phys. Rev. Lett.* **120** (2018) 231103, `arXiv:1804.00030 [hep-th]`.

[36] J. Rosa and S. Dolan, "Massive Vector Fields on the Schwarzschild Spacetime: Quasi-Normal Modes and Bound States," *Phys. Rev.* **D85** (2012) 044043, `arXiv:1110.4494 [hep-th]`.

[37] D. Brill, P. Chrzanowski, M. Pereira, E. Fackerell, and J. Ipser, "Solution of the Scalar Wave Equation in a Kerr Background by Separation of Variables," *Phys. Rev.* **D5** (1972) 1913–1915.

[38] B. Carter, "Hamilton-Jacobi and Schrödinger Separable Solutions of Einstein's Equations," *Commun. Math. Phys.* **10** (1968) 280.

[39] F. André Ronveaux *et al.*, *Heun's Differential Equations.* Oxford University Press, 1995.

[40] V. Frolov, P. Krtous, and D. Kubiznak, "Black Holes, Hidden Symmetries, and Complete Integrability," *Living Rev. Rel.* **20** (2017) 6, arXiv:1705.05482 [gr-qc].

[41] K. Thorne, "Multipole Expansions of Gravitational Radiation," *Rev. Mod. Phys.* **52** (1980) 299–339.

[42] C. Bender and S. Orszag, *Advanced Mathematical Methods for Scientists and Engineers I: Asymptotic Methods and Perturbation Theory.* Springer, 1999.

[43] M. Holmes, *Introduction to Perturbation Methods.* Texts in Applied Mathematics. Springer New York, 1998.

[44] A. Starobinsky, "Amplification of Waves Reflected from a Rotating "Black Hole"," *Sov. Phys. JETP* **37** (1973) 28. [Zh. Eksp. Teor. Fiz. **64** (1973) 48].

[45] S. Teukolsky, "Perturbations of a Rotating Black Hole. 1. Fundamental Equations for Gravitational, Electromagnetic and Neutrino Field Perturbations," *Astrophys. J.* **185** (1973) 635–647.

[46] Ó. Dias, J. Santos, and B. Way, "Numerical Methods for Finding Stationary Gravitational Solutions," *Class. Quant. Grav.* **33** (2016) 133001, arXiv:1510.02804 [hep-th].

[47] W. Gautschi, "Computational Aspects of Three-Term Recurrence Relations," *SIAM review* **9** (1967) 24–82.

[48] E. Leaver, "An Analytic Representation for the Quasi-Normal Modes of Kerr Black Holes," *Proc. Roy. Soc. Lond.* **A402** (1985) 285–298.

[49] S. Dolan and D. Dempsey, "Bound States of the Dirac Equation on Kerr Spacetime," *Class. Quant. Grav.* **32** (2015) 184001, arXiv:1504.03190 [gr-qc].

[50] W. Press, S. Teukolsky, W. Vetterling, and B. Flannery, *Numerical Recipes: The Art of Scientific Computing.* Cambridge University Press, 2007.

[51] V. Cardoso and S. Yoshida, "Superradiant Instabilities of Rotating Black Branes and Strings," *JHEP* **07** (2005) 009, arXiv:hep-th/0502206 [hep-th].

[52] S. Güttel and F. Tisseur, "The Nonlinear Eigenvalue Problem," *Acta Numerica* **26** (2017) 1–94.

[53] *NIST Digital Library of Mathematical Functions.* http://dlmf.nist.gov/.

[54] M. Abramowitz and I. A. Stegun, *Handbook of Mathematical Functions: with Formulas, Graphs, and Mathematical Tables*, vol. 55. Courier Corporation, 1965.

[55] L. Trefethen, *Approximation Theory and Approximation Practice*, vol. 128. Siam, 2013.

[56] J. Boyd, *Chebyshev and Fourier Spectral Methods.* Dover Books on Mathematics. Dover Publications, Mineola, NY, 2nd ed., 2001.

[57] J.-P. Berrut and L. Trefethen, "Barycentric Lagrange Interpolation," *SIAM review* **46** (2004) 501–517.

[58] L. Trefethen, "Six Myths of Polynomial Interpolation and Quadrature," 2011.

[59] N. Higham, "The Numerical Stability of Barycentric Lagrange Interpolation," *IMA Journal of Numerical Analysis* **24** (2004) 547–556.

[60] R. Baltensperger, "Improving the Accuracy of the Matrix Differentiation Method for Arbitrary Collocation Points," *Applied Numerical Mathematics* **33** (2000) 143–149.